

A. Manhard, U. Fantz, A. Stäbler, H. Greuner, B. Crowley

## **Spectroscopic Studies on Positive Ion Based Neutral Beam Injection Systems**

Spektroskopische Untersuchungen an Neutralteilcheninjektoren  
basierend auf positiven Ionen

**IPP 4/289**  
**July, 2008**



# **Spectroscopic Studies on Positive Ion Based Neutral Beam Injection Systems**

Spektroskopische Untersuchungen an  
Neutralteilcheninjektoren basierend auf positiven Ionen

A. Manhard, U. Fantz, A. Stäbler, H. Greuner, B. Crowley

This report is based on a diploma thesis of  
Armin Manhard  
Universität Augsburg  
Max-Planck-Institut für Plasmaphysik  
April 2008

Dieser Report basiert auf einer Diplomarbeit von  
Armin Manhard  
Universität Augsburg  
Max-Planck-Institut für Plasmaphysik  
April 2008



# Summary

Neutral beam injection systems based on positive hydrogen ions are used for plasma heating at most of the fusion experiments worldwide. The ion sources are low pressure plasmas that are either created by arc discharges or by inductive RF coupling. The ions are extracted by a multi-aperture grid and then neutralised in a gas target.

An important parameter for the heating power and profiles is the ion species composition in the extracted ion beam. Their correlation with the plasma parameters in the ion source is the subject of this thesis. This was investigated at two different RF driven ion sources at the Max-Planck-Institut fuer Plasmaphysik in Garching by varying the RF power and the gas pressure. In order to investigate isotope effects measurements were performed in hydrogen and deuterium, respectively. For comparison with arc generated plasmas measurements have been prepared at the neutral beam testbed of the European fusion experiment JET.

The extracted beam was analysed with the established method of  $H_\alpha$  Doppler spectroscopy. The extracted ion species  $H^+$ ,  $H_2^+$  and  $H_3^+$  interact with the neutraliser gas and fragment into fast excited neutral atoms with different velocities. The ion species distribution can then be derived from the intensity ratio of the respective Doppler shifted  $H_\alpha$  lines. The light emitted by hydrogen atoms and molecules in the ion source was analysed spectroscopically. For the analysis, absolute intensities of individual transitions were used as well as intensity ratios. From these measurements, the ratio of the atomic to the molecular density, the electron temperature and density as well as the gas temperature and the vibrational population of the hydrogen molecules were derived.

The investigations clearly show a dependence of the plasma parameters in the ion source with the source parameters, i.e. RF power and gas pressure. The same basic tendencies are obtained for both RF driven sources. The species distribution in the extracted beam also shows a clear correlation with the source plasma parameters. For example, an increase of the RF power increases the degree of dissociation in the hydrogen plasma and thus the amount of protons in the beam. A higher dissociation degree is observed in deuterium plasmas compared to hydrogen plasmas.



# Zusammenfassung

Neutralteilcheninjektoren auf der Grundlage von positiven Wasserstoffionen werden weltweit an zahlreichen Fusionsexperimenten zur Plasmaheizung eingesetzt. Bei den Ionenquellen handelt es sich um Niederdruckplasmen, die entweder in Bogenentladungen oder mittels induktiver HF-Einkopplung erzeugt werden. Durch ein System gitterförmiger Elektroden werden die Ionen extrahiert und anschließend beim Durchgang durch ein Gastarget neutralisiert.

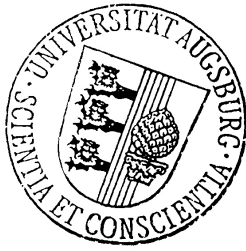
Ein wichtiger Parameter für die Heizleistung und die -rofile ist die Ionenzusammensetzung des extrahierten Ionenstrahls. Deren Zusammenhang mit den Parametern des Quellenplasmas ist Gegenstand der vorliegenden Arbeit. Dazu wurde an zwei HF-betriebenen Systemen unterschiedlicher Bauart am Max-Planck-Institut für Plasmaphysik in Garching die HF-Leistung und der Gasdruck variiert. Des Weiteren wurden Messungen mit Wasserstoff und Deuterium durchgeführt, um Isotopeneffekte herauszuarbeiten. Zum Vergleich mit Systemen mit bogenerzeugten Plasmen wurden zudem vorbereitende Maßnahmen für Messungen am Neutralteilchenteststand des europäischen Fusionsexperiments JET durchgeführt.

Der extrahierte Teilchenstrahl wurde mit der seit längerem bewährten Methode der  $H_\alpha$ -Dopplerspektroskopie analysiert. Bei der Wechselwirkung mit dem Neutralisatorgas fragmentieren die extrahierten Ionenspezies  $H^+$ ,  $H_2^+$  und  $H_3^+$  zu unterschiedlich schnellen angeregten H-Atomen. Das Intensitätsverhältnis der dopplerverschobenen  $H_\alpha$ -Linien erlaubt dabei Rückschlüsse auf die Ionenspeziesverteilung. Zudem wurde die Strahlung der Wasserstoffatome und -moleküle in der Ionenquelle spektroskopisch analysiert. Hierzu wurden sowohl absolute Intensitäten einzelner Übergänge als auch Intensitätsverhältnisse herangezogen. Daraus wurden das Verhältnis von Atom- zu Moleküldichte, die Elektronentemperatur und -dichte sowie die Gastemperatur und die Vibrationsbesetzung der Wasserstoffmoleküle abgeleitet.

Die Untersuchungen zeigen klare Abhängigkeiten der Plasmaparameter in der Ionenquelle von der HF-Leistung und dem Gasdruck. Für die beiden HF-Systeme, die sich in ihrer Geometrie unterscheiden, wurden die gleichen grundlegenden Tendenzen gemessen. Es zeigt sich ein deutlicher Zusammenhang der Speziesverteilung im extrahierten Strahl mit den Plasmaparametern in der Ionenquelle. So steigt zum Beispiel mit zunehmender HF-Leistung der Dissoziationsgrad des Wasserstoffplasmas und somit der Protonenanteil im extrahierten Ionenstrahl. In Deuteriumplasmen ist der Dissoziationsgrad höher als in Wasserstoffplasmen.







Lehrstuhl für Experimentelle Plasmaphysik  
Universität Augsburg

# **Spectroscopic Studies on Positive Ion Based Neutral Beam Injection Systems**

Diplomarbeit  
von  
Armin Manhard

vorgelegt  
am 14. April 2008



Lehrstuhl für Experimentelle Plasmaphysik  
Universität Augsburg

# **Spectroscopic Studies on Positive Ion Based Neutral Beam Injection Systems**

Diplomarbeit  
von  
Armin Manhard

vorgelegt  
am 14. April 2008

Erstprüfer: Priv.-Doz. Dr.-Ing. U. Fantz  
Zweitprüfer: apl. Prof. Dr. J. K. N. Lindner



# Contents

<b>1</b>	<b>Introduction</b>	<b>5</b>
<b>2</b>	<b>Neutral Beam Injection</b>	<b>7</b>
2.1	Thermonuclear Fusion with Magnetic Confinement . . . . .	7
2.2	Principles of Neutral Beam Injection . . . . .	9
2.3	The Ion Source . . . . .	10
2.4	The extraction system . . . . .	12
2.5	The Neutraliser . . . . .	16
2.6	Investigated Types of Neutral Beam Injection Systems . . . . .	17
2.6.1	The Arc PINI at JET . . . . .	17
2.6.2	The RF PINI at ASDEX Upgrade . . . . .	19
2.6.3	The RF Ion Source at GLADIS . . . . .	21
2.6.4	Comparison of the Investigated Ion Sources . . . . .	23
<b>3</b>	<b>Optical Emission Spectroscopy</b>	<b>25</b>
3.1	Spectroscopic systems . . . . .	25
3.2	Calibration of the spectrometers . . . . .	30
3.2.1	Wavelength Calibration . . . . .	30
3.2.2	Intensity calibration . . . . .	31
3.3	The emission spectrum of a plasma . . . . .	38
3.3.1	Rate coefficients . . . . .	38
3.3.2	Plasma Models . . . . .	40
3.4	Evaluation of the Atomic Spectrum with a Collisional Radiative Model . . . . .	42
3.5	Emission Spectrum of the Hydrogen Molecule . . . . .	45
3.5.1	Nomenclature for Molecular States . . . . .	45
3.5.2	The Emission Spectrum of Diatomic Molecules . . . . .	46
3.5.3	Evaluation of the Fulcher Transition . . . . .	52
3.6	Spectroscopic Measurement of the Atom to Molecule Ratio . . . . .	55

3.7	Measurement of the Species Distribution by $H_{\alpha}$ Doppler Spectroscopy . . . . .	58
<b>4</b>	<b>Preparation Work at JET</b>	<b>63</b>
4.1	The JET Neutral Beam Test Bed . . . . .	63
4.2	Testing of the Spectroscopic Equipment . . . . .	64
4.3	Maintenance and Refurbishment Work . . . . .	66
4.3.1	Spectral Radiance Standard . . . . .	66
4.3.2	Spectrometer Entry Optics . . . . .	67
4.3.3	CCD Camera . . . . .	67
4.4	Spectrometer Calibration . . . . .	69
4.5	Data File Conversion Program . . . . .	69
4.6	Measurements . . . . .	69
<b>5</b>	<b>Experiments at IPP Garching</b>	<b>71</b>
5.1	The Neutral Beam Injection at ASDEX Upgrade . . . . .	71
5.1.1	Lines of Sight . . . . .	72
5.1.2	Measurements . . . . .	73
5.1.3	Results . . . . .	75
5.2	The GLADIS High Heat Flux Test Bed . . . . .	80
5.2.1	Lines of Sight . . . . .	81
5.2.2	Measurements . . . . .	82
5.2.3	Results . . . . .	83
5.3	Comparison of the RF sources . . . . .	96
5.4	Synopsis . . . . .	99
<b>6</b>	<b>Summary</b>	<b>101</b>
<b>A</b>	<b>Appendix</b>	<b>107</b>
A.1	Sample spectra . . . . .	107
A.2	Molecular Data . . . . .	109
A.3	JET Neutral Beam Test Bed . . . . .	116
A.3.1	Wavelength Calibration Results . . . . .	116
A.3.2	Absolute Intensity Calibration . . . . .	117
A.3.3	Fibre Holder Construction Drawings . . . . .	118

# 1 Introduction

The heating of magnetically confined fusion plasmas with high energy neutral hydrogen beams was developed in the 1970s. Since then, it has become one of the most powerful and effective heating mechanisms in fusion experiments. The idea of neutral beam heating is that only neutral particles can penetrate the magnetic field and convey energy into the fusion plasma. These fast neutrals are created by extracting positive or negative hydrogen ions from a low temperature plasma. The ions are then accelerated electrostatically to energies of several 10 to 100 keV. Finally, the fast ions are converted into fast neutrals by interaction with a neutral gas target.

For many contemporary fusion experiments, positive ion based neutral beam injection systems are used. But despite their widespread use, there are still open questions regarding the plasma inside the ion source. Much higher injection energies (in the order of 1 MeV) will be needed for large scale fusion experiments of the next generation. In this energy range, only negative hydrogen ions have a sufficient neutralisation probability. While negative ions are in principle also favourable for current experiments, their efficient generation and extraction is much more difficult. Because of that, only few fusion experiments have adopted this technology yet. Furthermore, many concepts for negative hydrogen ion sources are based on their positive ion counterparts. This makes a thorough investigation of positive hydrogen ion sources still interesting.

For a comprehensive understanding of positive hydrogen ion sources, the plasma inside the ion source and the extracted particle beam are spectroscopically analysed. Optical emission spectroscopy is an advantageous measuring method for both the source plasma and the beam. First of all, it is non-invasive. It is also relatively easy to gain optical access to the ion source and the beam, and the use of glass fibres for transmitting the emitted light to the spectrometer inherently provides electrical insulation from the high voltage for the extraction.

In the ion source, the radiation of atomic and molecular hydrogen is measured relatively as well as in absolute units in order to determine the atom to molecule ratio, the electron density and temperature, the gas temperature and the vibra-

tional population of the hydrogen molecule. The Doppler shifted light emitted from fast excited hydrogen atoms in the beam is used to derive the ion species distribution. This allows a correlation of the ion beam and the parameters of the source plasma. The species distribution in the ion beam can be also be used as a measure for the ion species distribution inside the ion source. Measuring the positive ion species distribution by Doppler spectroscopy of the beam is not possible for negative hydrogen ion sources as only negative ions (and electrons) are extracted. In these ion sources, atomic and molecular positive hydrogen ions contribute to the formation of negative hydrogen ions in a surface process with caesium. An extrapolation of the results from positive hydrogen ion sources that is based on the plasma parameters in the ion source is therefore especially interesting.

To understand how the input power for the plasma generation and the gas pressure in the ion source influence the source plasma parameters and accordingly the extracted beam, sweeps of both these control parameters are performed. The investigation of different types of ion sources yields information about the influence of the ion source geometry and also the method of plasma generation. Furthermore, operating the ion sources with hydrogen and deuterium allows to study isotope effects.



## 2 Neutral Beam Injection

This chapter introduces the underlying concepts and technology of neutral beam injection (NBI) systems, and describes the fusion experiments where NBI systems are used. It explains the methods of plasma generation in the ion source of the injectors, the extraction and the neutralisation of the ion beam. Based on this, the investigated systems are presented.

### 2.1 Thermonuclear Fusion with Magnetic Confinement

One possibility to confine the hot plasmas necessary for thermonuclear fusion are magnetic fields in a toroidal geometry. On top of the toroidal confinement fields, particle drifts in the plasma make a poloidal field component necessary. There are two approaches to achieve the poloidal component: the *tokamak* and the *stellarator*.

In present day tokamak experiments, the plasma current is mainly created inductively by a transformer discharge, which inherently limits these machines to pulsed operation. Because of this, methods to drive a plasma current non-inductively are currently being investigated, for example by tangential injection of neutral beams and by high frequency electromagnetic waves. Another problem of tokamaks is an instability causing the sudden termination of the plasma current (a so-called *disruption*). This subsequently causes a near-immediate breakdown of the confinement. Developing methods for disruption mitigation is therefore also important. Large tokamak fusion experiments currently include JET (*Joint European Torus*, UK), ASDEX Upgrade (*Axially Symmetric Divertor EXperiment*, Germany), JT-60U (Japan) and DIII-D (USA). The international large scale experiment ITER (lat.: “the way”) that is currently being built in France will also have a tokamak configuration.

In stellarator experiments, the poloidal magnetic field component is created by

coil currents alone. Therefore, no transformer-driven plasma current is needed. This makes the stellarator a promising candidate for continuous operation, and also cancels the problem of the disruption instability. The design and construction of a stellarator are quite difficult because it needs very complexly shaped magnetic field coils. Also, in contrast to the tokamak, the plasma does not possess cylindrical symmetry anymore, which makes three dimensional computer codes for plasma simulation necessary. The more complex experimental set-up compared to tokamaks, including coil geometry and the necessity for non-ohmic heating, has led to stellarators presently being less developed by about one machine generation. Contemporary stellarator experiments are for example WENDELSTEIN 7-AS (recently decommissioned), its successor WENDELSTEIN 7-X (currently under construction, both in Germany), and LHD (*Large Helical Device*, Japan). The two different geometries for fusion experiments with magnetic confinement can be seen in Fig. 2.1.

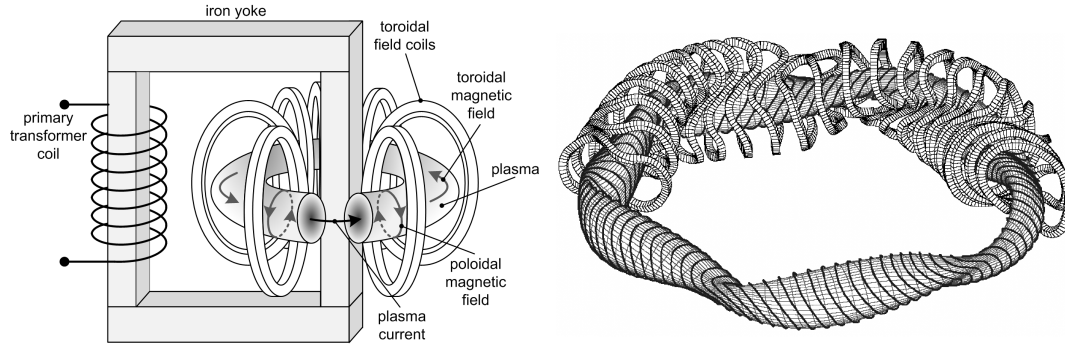


**Figure 2.1:** Magnetic field configuration of a tokamak (left) and a stellarator (right).

Existing and future fusion experiments require external energy sources in order to create and sustain a plasma at conditions comparable those required for fusion. Both tokamak and stellarator experiments are presently heated by electromagnetic wave heating at different frequencies. Tokamaks also have inherent ohmic heating by the plasma current. Probably the most important external heating method for both fusion experiment set-ups nowadays is the injection of high energy neutral particles.

## 2.2 Principles of Neutral Beam Injection

The injection of high energy particle beams is a very effective heating method for fusion experiments with magnetic confinement. However, only neutral particles are able to penetrate the confinement field and heat the fusion plasma. On the other hand, only charged particles can be accelerated to high energies by electric fields. The solution to this problem is to extract ions from a low temperature plasma source, accelerate them electrostatically and finally neutralize them through collisions with a cold neutral gas target (*“neutraliser”*). After this, the remaining ions in the beam have to be filtered out by magnets and directed onto cooled ion dumps in order to prevent uncontrolled deflection at the confinement field. Fig. 2.2 schematically shows a neutral beam injection (NBI) set-up.

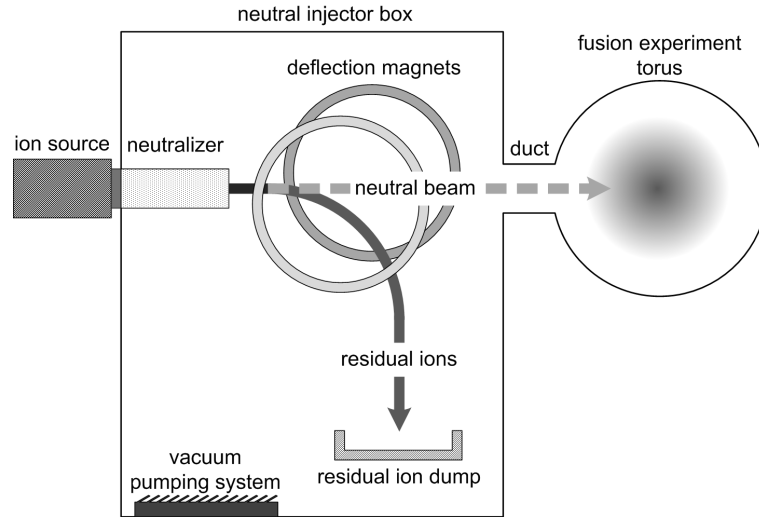


**Figure 2.2:** Neutral beam injector (schematic)

When the fast neutral particles interact with the fusion plasma, they are ionised by charge exchange with low energy ions. Subsequently, the fast ions are confined by the magnetic field, whereas the slow neutrals can leave the plasma. The confined fast ions can then distribute their energy to the plasma by collisions. Additionally, it is possible to drive a fraction of the plasma current necessary for tokamaks by tangential injection of neutral beams. Finally, NBI also serves as a method of refuelling the fusion plasma.

Recently, sources for negative hydrogen (respectively deuterium) ions are being developed because of their far better neutralisation efficiency at high energies around 500 keV per nucleon. This is needed for large scale experiments like ITER because at a given plasma density, the penetration depth of neutral particles into a

fusion plasma is in reasonable approximation proportional to their kinetic energy per nucleon [DAF<sup>+</sup>87]. However, most present day NBI systems still use positive ions since the neutralization efficiency is still acceptable at energies around 60 keV per nucleon, which is usually sufficient, and higher ion current densities can be extracted. Also, the systems needed for the extraction of negative ions are more complex, e.g. due to co-extracted electrons.

Spectroscopic measurements were taken in the ion source plasma as well as in the neutraliser region of the extracted beam. This was done in order to correlate the plasma conditions in the source, especially the atom to molecule ratio, with the ion species distribution in the extracted beam. The ion species distribution is important for the optimised operation of positive ion based systems as well as for modelling the plasma of sources for negative hydrogen ions with a comparable set-up. The evaluation methods will be described in more detail in chapter 3.

## 2.3 The Ion Source

There are two different approaches to the generation of the ion source plasma. The “classical” one is a *DC arc discharge*: a potential difference of approximately 100 V is applied between heated tungsten filaments and the metallic walls of the ion source; the resulting arc current typically is in the order of 1000 A, which makes for an overall input power of around 100 kW [DAF<sup>+</sup>87]. In order to improve the insulation of the plasma from the walls, *confinement magnets* are used. This means that strong permanent magnets (e.g. CoSm) are arranged around the source body in a multipole pattern [EL73, DAF<sup>+</sup>87]. This way, a magnetic cusp field is created in the vicinity of the walls. Between the cusps, the electron density drops to zero in an approximately linear way over several centimetres. At the cusps, the plasma comes much closer to the walls. Overall, this leads to an effective magnetic surface that is detached from the walls, and subsequently improves the ion source efficiency [CBC83]. Outside the effective range of the cusp field, plasma shows a good homogeneity in a plane parallel to the extraction surface (typically around  $\pm 5\%$ ) [DAF<sup>+</sup>87]. This type of ion source is also called (*magnetic*) *bucket source*.

In some cases, an additional long range magnetic filter field is used. This “super-cusp” configuration is shown in Fig. 2.3. The filter field is supposed to keep primary arc electrons with high energies of  $\approx 100$  eV away from the extraction region near the plasma grid in order to suppress the production of  $\text{H}_2^+$  ions. Since

the magnetic filter field also causes a decreased electron temperature near the plasma grid, dissociative recombination of molecular ions is assumed to be enhanced, thus increasing the degree of dissociation and accordingly the  $H^+$  yield of the ion source [DAF<sup>+</sup>87]. On the downside, the filter field also causes a general plasma inhomogeneity that makes beam steering more difficult and causes power losses along the beam line [GCF00].

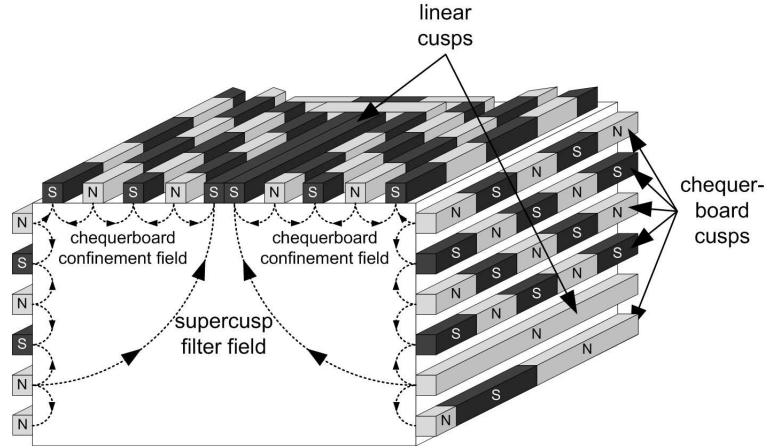


**Figure 2.3:** Confinement magnet pattern with an additional “supercusp” magnetic filter [DAF<sup>+</sup>87].

A different approach to the source plasma generation is an inductively coupled radio frequency (RF) discharge. A typical design features an RF coil that is wound around a body made from a dielectric material, e.g. quartz or alumina. The back plate of the source body is metallic and in some designs shielded by a magnetic cusp field similar to the one used in arc sources. The side walls do not have magnetic shielding. In order to protect them from erosion by the plasma, a slotted metal screen is introduced between plasma and wall. It provides electrostatic confinement of the plasma, but also increases the source impedance and prevents capacitive coupling of the RF to the plasma. This causes two problems: it reduces the impedance of the source, which makes the impedance matching of the plasma more difficult. The electrostatic shielding by the Faraday screen also decreases the efficiency of the RF heating and makes a starter filament necessary [KSF<sup>+</sup>98]. However, erosion of material from the dielectric body cannot be tolerated since decreases the voltage holding capability of the extraction system [FKS<sup>+</sup>95].

The RF can penetrate into the plasma only on the scale of the skin depth. This means that in an RF discharge, the actual heating zone is restricted to the vicinity the walls around which the RF coil is wound. The plasma of large area

RF-driven ion sources is therefore more inhomogeneous than that of comparable bucket sources [FKS<sup>+</sup>95]. This can be alleviated by adding magnets near the extraction system [SCF<sup>+</sup>99].

A major advantage of RF ion sources is that they require very little maintenance. Arc sources, on the other hand, suffer from evaporation of the filaments. The filaments therefore have to be replaced regularly. Additionally, in sources for negative hydrogen ions, the negative ions are created by a surface process on a surface with a small electron work function. The deposition of filament material would compromise these surfaces. Apart from that, the RF generators can be galvanically de-coupled from the ion source by an isolation transformer. This is advantageous since the source body is set at high potential and the extracted ions accelerated towards ground potential (see section 2.4). For an arc source, this is not possible, so the whole power supply for the filaments and the arc have to be set at high potential, too [SCF<sup>+</sup>99]. Another advantage of RF sources is that their power output can be regulated faster than in arc sources, which makes real-time current feedback regulation possible [FOS<sup>+</sup>98]. The simpler design of RF sources (only one RF coil as opposed to multiple filaments and power supplies for filament heating and the arc) also makes them more cost effective in production [SCF<sup>+</sup>99].

## 2.4 The extraction system

Typical NBI systems have a gross power before neutralisation in the range of megawatts. Because a divergent beam would cause an intolerable power loading of beamline components, the beams must have a very good quality (divergences in the order of 1°). After the neutralisation of the particle beam, it cannot be controlled and refocussed by electric and magnetic fields any more, so this quality has to be achieved right in the extraction and acceleration system.

For a large area beam with typical cross sections of several 100 cm<sup>2</sup> up to over 1000 cm<sup>2</sup>, many small scale extraction apertures are preferred over a single large extraction aperture. Typical are over 100 apertures with a diameter in the order of 1 cm. This allows for better optimisation of the ion optical properties [Spe89]. For the investigated types of ion sources, a system of three or four grid electrodes with circular apertures is used to extract the ions [Spe89]. The grid in contact with the plasma (*plasma grid*) is set at a strong positive potential  $U_{ex}$  of up to more

than 100 kV along with the source body. The next grid (*electron suppression* or “*deceleration*” *grid*) is set at a slightly negative potential of several kV, while the final grid (*earth grid*) is set at ground potential. The negative potential electrode is needed to keep electrons that are created in the neutraliser from streaming back into the accelerator since this would strain the power supplies as well as the grid system (and even the backplate of the ion source). An additional grid electrode is sometimes introduced between the plasma grid and the electron suppression grid for even more control over the ion optics [SCCG02]. A section of an extraction grid system can be seen in Figs 2.4 and 2.5.

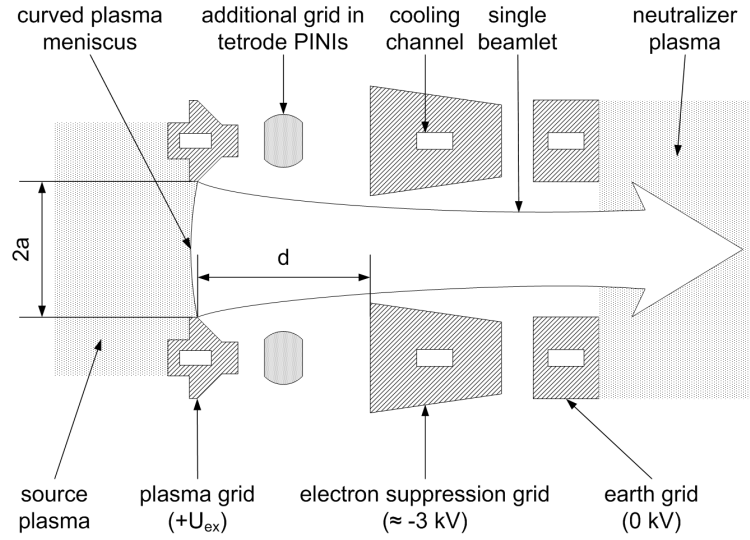


**Figure 2.4:** Extraction grid system of a neutral beam injector. The additional grid between plasma grid and suppressor grid is only present in tetrode designs.

The beams extracted from the ion source of a NBI system are usually focussed, with a focal length of several metres (depending on the distance between torus and ion source). There are several possibilities to achieve this focussing. A straightforward method is to either use a curved the grid surface, or to divide the grid into multiple subsections that are tilted against each other. Another way to achieve beam steering is to offset the aperture positions in the suppression grid with respect to the plasma grid. For a convergent beam, the aperture spacing has to be closer packed in the plasma grid. This is because the decelerating potential between the suppression grid and the earth grid creates a negative lens effect. Therefore, the suppression grid’s apertures have to be displaced outward from the beam axis [DAF<sup>+</sup>87, Spe89].

Apart from the focussing described above, the total beam optics are determined



**Figure 2.5:** Detail view of the triode grid system of the GLADIS ion source. The topmost grid is the plasma grid. Behind that, the electron suppression grid and the earth grid can also be seen.

by the optics of each sub-beam (usually called *beamlet*). The beamlets' ion optics, primarily their divergence, are determined by space charge effects. According to the Child-Langmuir law the maximum space charge limited current  $I$  that can be driven by a voltage  $U$  is given by

$$I = \Pi_{max} U^{\frac{3}{2}}. \quad (2.1)$$

The value  $\Pi_{max}$  is called the (*maximum*) *perveance*. For a solely space charge limited current,  $\Pi_{max}$  is a purely geometric factor and is given by

$$\Pi_{max} = \frac{4\pi\epsilon_0}{9} \sqrt{\frac{2e}{m}} \left(\frac{a}{d}\right)^2. \quad (2.2)$$

Here  $a$  is the radius of the anode aperture,  $d$  is the distance between the anode and the cathode as shown in Fig. 2.4.  $m$  is the ion mass.

In analogy to (2.1), a perveance can also be defined as a general property of a charged particle beam with extraction voltage  $U_{ex}$  and extracted current  $I$ :



$$\Pi = \frac{I}{U_{ex}^{\frac{3}{2}}}. \quad (2.3)$$

For a certain perveance  $\Pi_{opt} < \Pi_{max}$  that depends on the exact implementation of the extraction system, the divergence of the extracted beam becomes minimal.  $\Pi_{opt}$  is therefore called the *optimum* perveance [Spe89]. The divergence does not completely vanish at  $\Pi_{opt}$ . One reason for this is a finite ion temperature in the plasma that causes the ion velocity perpendicular to the beam to be non-zero [FKV<sup>+</sup>99]. Apart from that, there are higher order ion optical aberrations and space charge forces. Also, it has to be kept in mind that the “anode” for the extraction of ions from a plasma is not a solid planar surface but a curved surface (*meniscus*) that is determined by space charge effects of the extracted ion flow (and therefore the extraction voltage) and the plasma [Spe89].

For the extraction grid system of an ion source, the spacing between plasma grid and deceleration grid therefore has to be set in order to accommodate the specified extraction voltage and extracted current at optimum perveance. Due to higher order aberrations of the beamlet optics at the edge of the aperture the actual optimum perveance may be lower than a theoretically derived optimum value [Cox03, Spe89]. For all different settings of extraction voltages, the current has to be regulated to achieve perveance matching. This is usually done by regulating the plasma source input power (arc or RF) and thus the extractable ion density.

There are not only  $H^+$  ( $D^+$ ) ions in the source plasma of a neutral beam injector, but also  $H_2^+$  and  $H_3^+$  molecular ions. These are extracted as well by the extraction voltage  $U_{ex}$  and reach an energy of  $E_0 = e \cdot U_{ex}$ . In the neutraliser (see section 2.5), however, they dissociate into neutral atoms with  $1/2 E_0$  or  $1/3 E_0$ . There is also a minor fraction of fast neutral  $H_2$  molecules with full or  $2/3$  energy [FVS98]. The fraction of the total beam power carried by these reduced energy neutrals is not transported as far into the plasma core as the fraction carried by full energy neutrals: in a rough approximation, the mean free path for ionisation  $\lambda_i$  (and therefore the penetration depth into the plasma) is proportional to the kinetic energy per nucleon of the neutral particles [DAF<sup>+</sup>87]. Larger molecular ion fractions therefore cause a broader power deposition profile in the fusion plasma. The ion species distribution also influences the efficiency of the NBI system, i.e. the

ratio of the power injected into the fusion plasma to the gross extracted beam power. This is because the neutralisation cross section is higher for the molecular ions.

This means that the ion species distribution is an important parameter for optimising a NBI system for a given task, i.e. high heating efficiency for the fusion plasma, or a high, peaked power deposition profile. This can be achieved through constructive measures like the use of magnetic filters or certain wall materials. Apart from that, the ion species distribution is an important parameter for plasma modelling. The species distribution is also interesting for optimising negative hydrogen ion sources because the positive hydrogen ions  $H^+$ ,  $H_2^+$  and  $H_3^+$  also contribute significantly to the formation of negative hydrogen ions in the surface process.

One aim of this work is to investigate the relations between ion source control parameters like pressure and input power and the ion species distribution by analysis of the ion beam. Additionally, the source plasma is analysed in order to correlate the ion species distribution directly to the source plasma conditions.

## 2.5 The Neutraliser

In a typical NBI system, a neutraliser gas target is provided by a cold hydrogen gas flow through an approximately 2 m long<sup>1</sup> drift tube directly after the accelerator. The gas flow in the neutraliser is provided by neutral gas streaming from the ion source as well as from valves in the neutraliser tube itself. The main property of the neutraliser is its linear target thickness  $\langle nL \rangle$  [FVS98]:

$$\langle nL \rangle = \int_0^L n \, dl \quad (2.4)$$

with  $n$  as the neutral gas density and  $L$  as the geometrical length of the neutraliser. When the ion beam passes through the neutraliser gas, fast ions are neutralized by charge exchange with slow neutral molecules (or atoms). The fast neutrals created by this process can also be re-ionised. This leads to a neutral beam fraction  $F_0$  after the neutraliser that increases with target thickness and saturates for thick targets ( $\langle nL \rangle \geq 5 \cdot 10^{19} \text{ m}^{-2}$ ) [FVS98]:

---

<sup>1</sup>At ASDEX Upgrade [FVS98].

$$F_0 = F_0^\infty \left(1 - e^{-\langle nL \rangle (\sigma_{+10} + \sigma_{0+1})}\right), \quad (2.5)$$

where  $F_0^\infty$  is the limit of  $F_0$  for an infinitely thick target, and  $\sigma_{+10}$  and  $\sigma_{0+1}$  are the cross sections for neutralisation respectively re-ionisation of beam particles. Usually, neutralisers are designed to have target thicknesses that lie in the saturation region for  $F_0$ . However, due to heating of the neutral gas and even plasma formation due to the ion beam hitting the neutraliser gas target, the target thickness can be reduced [SCC<sup>+</sup>02, SC03].

## 2.6 Investigated Types of Neutral Beam Injection Systems

Investigations were focussed on three different NBI systems. The first one has an arc-driven ion source and is located at the neutral beam test bed (NBTB) of the fusion experiment JET (Culham, UK) [DAF<sup>+</sup>87]. The second one is an RF source at the fusion experiment ASDEX Upgrade (Garching, Germany) [FKS<sup>+</sup>95]. Both these systems are variants of the PINI (*Plug-In Neutral Injector*) design. This is a modular design that uses a quasi-standardised extraction system and neutraliser. The ion sources have a very similar geometry on the outside and are designed to illuminate identical extraction areas.

The third system is an RF-driven system that was modified for use in the materials testing facility GLADIS (*Garching Large DIvertor Sample test facility*) at Garching [GBB<sup>+</sup>05]. Originally the NBI system of the now decommissioned stellarator WENDELSTEIN 7-AS [KFH<sup>+</sup>01], it is now used for subjecting plasma facing components for fusion experiments to reactor typical heat fluxes (up to 10 - 20 MW/m<sup>2</sup>). The GLADIS system does not have a residual ion filter, so the full beam (i.e. ions and neutrals) is directed onto the sample.

### 2.6.1 The Arc PINI at JET

The arc source at JET is the classical PINI system. It is designed for arc currents up to 1500 A at an arc voltage of 100 V at gas pressures around 2.5 Pa. It has a

rectangular geometry with a cross section of  $61 \times 32 \text{ cm}^2$  and a depth of 19 cm. The extraction area has a cross section of  $18 \times 45 \text{ cm}^2$  and is divided into two halves containing 131 circular holes each (diameter: 12 mm) [Cox03]. The grid halves are inclined by  $\pm 0.47^\circ$  to the vertical plane to for vertical focussing of the beam. Offset steering is also used for additional focussing. The whole source body and extraction system are actively water cooled. A schematic of the arc source is shown in Fig. 2.6. Fig. 2.7 shows a photograph the complete PINI system at assembly.

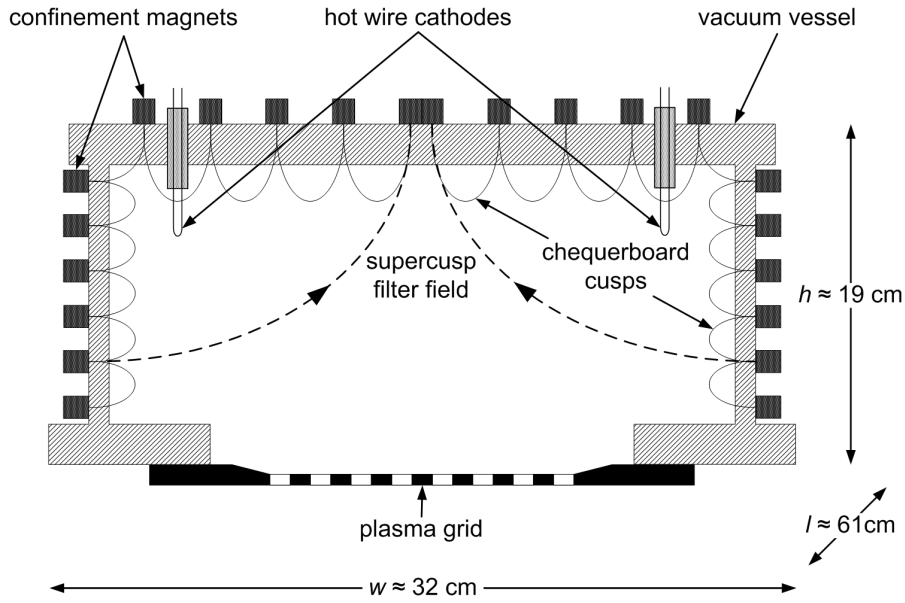


**Figure 2.6:** Schematic of an arc-driven PINI ion source.

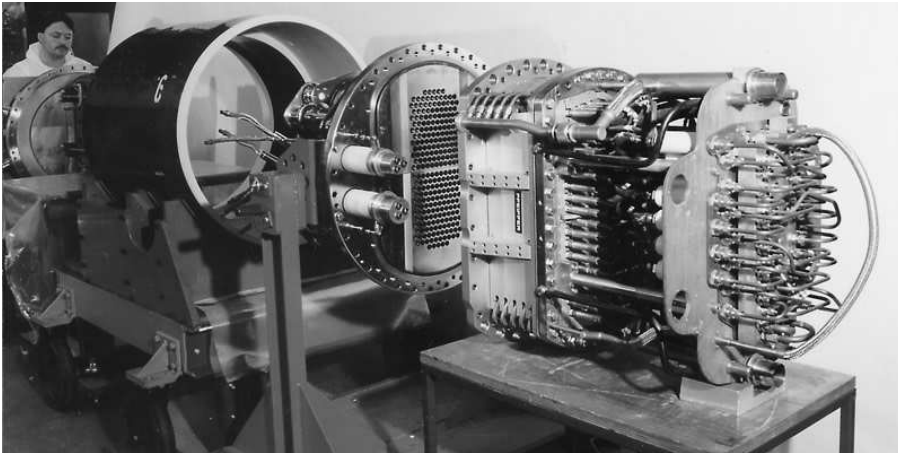


**Figure 2.7:** An arc-driven PINI of JET being assembled [EJ07].

This source was designed to achieve very high proton / deuteron fractions of more than 80%. For this purpose, the supercusp configuration for the confinement magnets was invented [DAF<sup>+</sup>87]. Because of the large plasma volume of JET (minor radius: 1.25 m) [EJ07], its neutral beam injectors are designed for high particle energies. The initial design featured extraction voltages of up to 80 kV in hydrogen or 160 kV in deuterium at extracted currents of up to 60 A for hydrogen or 42 A for deuterium. It has a tetrode extraction system [DAF<sup>+</sup>87]. Since the first use of the NBI system at JET, it has been continuously modified and improved. For the newest generation of PINIs, the extraction voltage has been reduced to 125 kV (deuterium), while the extracted current in deuterium was increased to 65 A. It has a triode extraction system. This ion source design also uses a pure chequerboard pattern for the confinement magnets. This leads to higher neutralisation efficiency and eliminates the plasma inhomogeneity caused by the supercusp filter field. Accordingly, the power losses through residual ions and beam line losses are reduced, and the heating power injected into the JET torus is increased [C<sup>+</sup>06].

Two injector boxes with eight PINIs each are installed at JET [EJ07]. Several different generations of arc PINIs are used. The NBI system is currently upgraded to a full set of 16 of the new 125 kV / 65 A PINIs. The projected total power is  $> 34$  MW (deuterium) injected into the torus at pulse durations of up to 20 seconds at full power and up to 40 seconds at half power (with the two injector boxes firing successively) [C<sup>+</sup>06]. Measurements were planned to be taken at the NBTB because the ion sources at the JET torus are not accessible for spectroscopic diagnostics. Also, the NBTB can operate independently from the main experiment. However, due to a long maintenance shut-down of JET and the NBTB only preparations for these measurements could be made. The NBTB facility and the conducted preparation work are described in chapter 4.

### 2.6.2 The RF PINI at ASDEX Upgrade

The newer RF-driven variant of the PINI at ASDEX Upgrade has a very similar outline compared to the JET PINIs. Its RF coil is placed inside a  $61 \times 32 \times 19$  cm<sup>3</sup> vacuum vessel and wound around a rectangular quartz body [FKS<sup>+</sup>95]. The vacuum is necessary because the quartz vessel cannot withstand atmospheric pressure. Additionally, it provides protection against breakthroughs between the coil windings at the high RF input powers of up to 87 kW at a frequency of approximately 1 MHz. A schematic of this ion source type can be seen in Fig.

2.8. The photograph in Fig. 2.9 shows the Faraday screen, the quartz vessel and the RF coil.

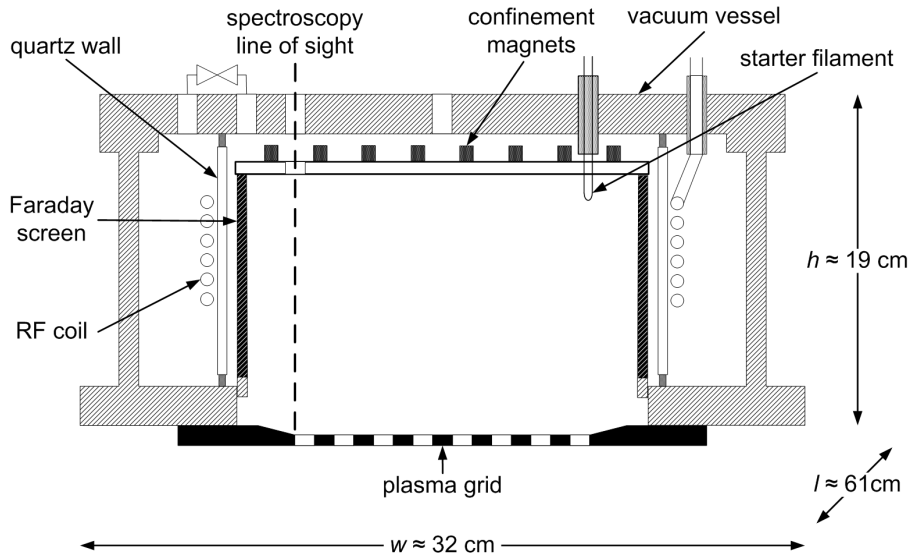


**Figure 2.8:** Schematic of the RF variant of the PINI ion source.

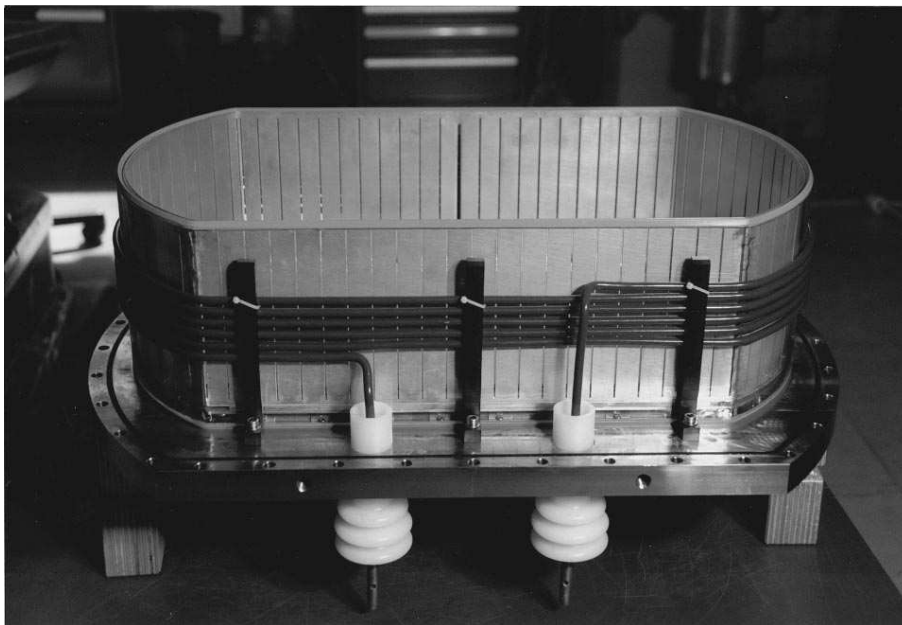


**Figure 2.9:** Faraday screen, quartz vessel and RF coil of an RF PINI source.

Like for the arc PINI, typical gas pressures are around  $2.5 \text{ Pa}^2$ . The extraction system is a triode system that can deliver currents of up to 64 A at an extraction

---

<sup>2</sup>It has to be noted that it is technically possible to vary the gas pressure for this system. For operational reasons this could not be done here, however.

voltage of 72 kV in hydrogen, or up to 63 A at 93 kV in deuterium<sup>3</sup>. The grid halves have an inclination of  $\pm 0.9^\circ$  [FKV<sup>+</sup>99] because the beam's travel length from the source into the plasma is shorter than at JET. This source has been designed for a high injection efficiency rather than a high proton fraction. It only uses confinement magnets in a chequerboard pattern to shield the back plate of the ion source [FKS<sup>+</sup>95]. Like the JET PINI, it is actively watercooled.

At ASDEX Upgrade, two injector boxes with four ion sources each are used [IPP08]. Beam line 1 (designated also “south-east”) uses arc PINIs with chequerboard confinement magnets and a maximum extraction voltage of 60 kV. These are not accessible for source plasma diagnostics, however. Beam line 2 (“north-west”) uses four of the RF PINIs described above. The maximum net heating power injected into the torus is 10 MW (deuterium) per beam line for up to 8 seconds [FKV<sup>+</sup>99]. The results presented here were obtained from source 4 of the north-west beam line. The beam line set-up along with the spectroscopy lines of sight is described in chapter 5.

### 2.6.3 The RF Ion Source at GLADIS

The system used at GLADIS is smaller than the PINIs and has a circular cross section with a diameter of 24.5 cm. The source depth is approximately 18 cm [KFH<sup>+</sup>01]. It operates at lower RF input powers than the PINI, only up to 35 kW (but at the same frequency of approximately 1 MHz) [GGB<sup>+</sup>05]. However, the maximum power density is about the same due to the smaller source volume. The gas pressure can be varied in five steps between 0.82 and 1.92 Pa (see section 5.2.3). For this source, the RF coil is wound around an alumina cylinder that directly serves as the vacuum wall, so the coil is located in air and only has a conventional insulation. The back plate is made out of copper [KFH<sup>+</sup>01]. The ion source is shown in Fig. 2.10. The extraction system is a focused triode system. It has a circular extraction area with a diameter of 17.4 cm that contains 187 circular holes (diameter: 7.85 mm). It is not divided into sub-grids like the PINI extraction system. Fig. 2.11 shows a photograph of the grid system with the alumina cylinder. It is designed to deliver up to 22 A at 55 kV in hydrogen [FKS82]. Since the GLADIS test bed does not have neutron shielding, it cannot be operated with deuterium.

The original design used only inertial cooling. For repetitive heat load testing of

---

<sup>3</sup>These values were obtained from electrical measurements.

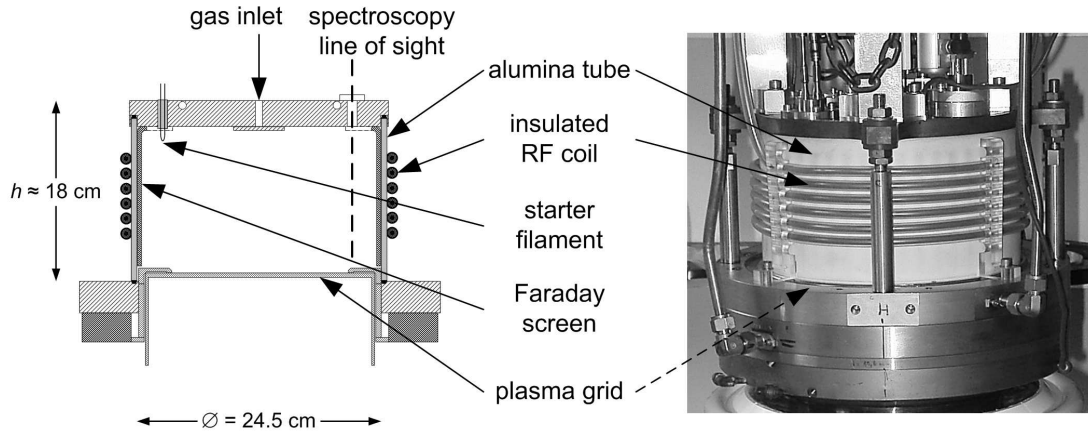


**Figure 2.10:** Modified WENDELSTEIN 7-AS RF ion source used at the GLADIS test bed.

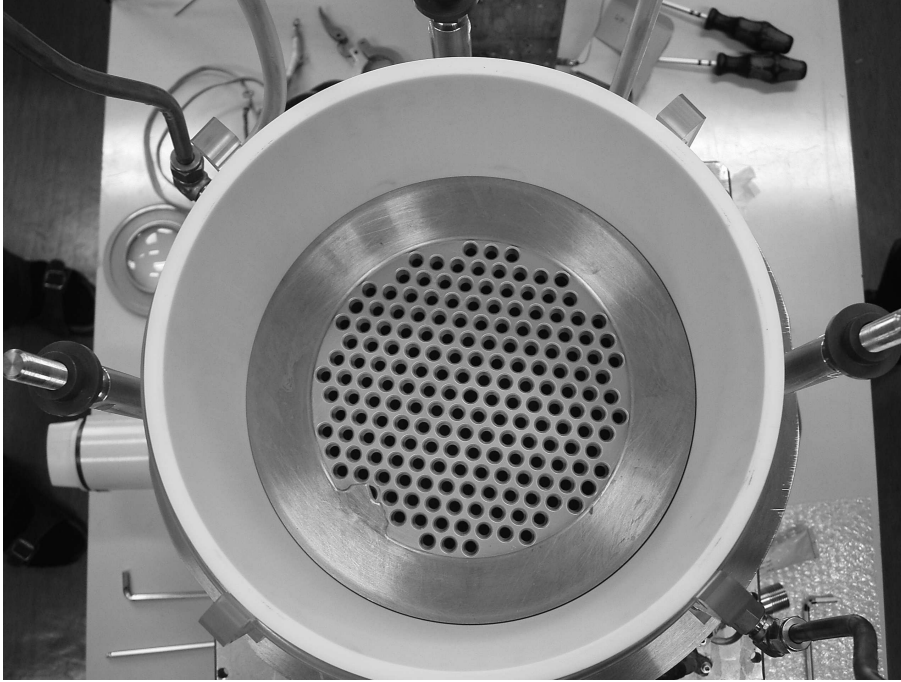


**Figure 2.11:** View from above into the open GLADIS ion source with extraction system and alumina cylinder. The protrusion on the lower left side of the rim surrounding the plasma grid protects the starter filament from backstreaming electrons.

fusion experiment components, pulse durations of up to 45 seconds at repetition rates of 60 - 100 pulses per hour are necessary. Because of that, the original extraction system has been replaced by the water cooled extraction system from the NBI of the decommissioned ASDEX tokamak<sup>4</sup> [GBBM07]. This system is fully compatible to the WENDELSTEIN 7-AS sources because of a common design

<sup>4</sup>The predecessor experiment of ASDEX Upgrade. It only used arc-driven ion sources but was designed for longer pulses than the NBI system of WENDELSTEIN 7-AS



basis [FKS82]. A water cooled Faraday screen has also been added, as well as water cooling for the back plate [GBBM07].

The GLADIS facility consists of two of the ion sources described above (only one of which is used presently) and cylindrical test chamber (length 3.2 m, diameter 1.5 m) for plasma facing components of fusion experiments. The test bed uses a mixed neutral and ion beam to deliver the heat flux to the samples. Therefore, almost all of the extracted beam power of up to 1.2 MW (apart from small losses along the beam line) is utilised. Extrapolations show that at full power, peak heat loads of up to 55 MW / m<sup>2</sup> can be achieved in the centre of the beam cross section [GBBM07]. The set-up of the GLADIS test bed along with the spectroscopy lines of sight can be found in chapter 5.

#### 2.6.4 Comparison of the Investigated Ion Sources

Investigating these three different types of NBI ion sources offers the possibility to compare the ion species distribution and the source plasma parameters for different methods of source plasma generation as well as for a wide range of gas pressures  $p_{source}$  and source input powers  $P_{input}$ . Additionally, measurements could be done both in hydrogen and deuterium. The different injector types also cover a wide range of extraction voltages  $U_{ex}$  and extracted currents  $I_{ex}$  and accordingly, of gross output powers  $P_{beam}$ . For comparison, all these parameters are compiled in Tab 2.1.

**Table 2.1:** Comparison of parameters for the discussed positive ion sources. The columns  $P_{input}$ ,  $U_{ex}$  and  $I_{ex}$  list maximum values. The column  $P_{beam}$  lists the maximum extractable beam power before the separation of residual ions.

Source Type	Gas	$P_{input}$ [kW]	$p_{source}$ [Pa]	$U_{ex}$ [kV]	$I_{ex}$ [A]	$P_{beam}$ [MW]	Plasma gen.
GLADIS source	H <sub>2</sub>	35	0.82 – 1.92	55	22	1.2	RF
RF PINI	H <sub>2</sub>	85	$\approx 2.5$	72	64	4.6	RF
RF PINI	D <sub>2</sub>	87	$\approx 2.5$	93	63	5.8	RF
JET PINI (supercusp)	D <sub>2</sub>	150	$\approx 2.5$	130	56	7.3	arc
JET PINI (chequerboard)	D <sub>2</sub>	150	$\approx 2.5$	125	65	8.1	arc

## 3 Optical Emission Spectroscopy

Optical emission spectroscopy (OES) is a non-invasive diagnostic method utilising the light emitted by plasmas. The observed wavelength region typically is the visible spectrum and can be extended to the near ultraviolet and near infrared regions, from about 200 nm to 1000 nm. Wavelength resolved analysis of the emitted light is nowadays usually performed by spectrographs with a diffractive grating, although optical prisms are possible, but less common. Some spectrometers also use a combination of both principles.

This chapter first describes the spectroscopic systems used for observing the ion source and neutraliser plasmas of the investigated ion sources and the process of calibrating the intensity axis of these systems. After that, the spectra of atoms and molecules in low pressure, low temperature hydrogen plasmas are explained. The methods for their interpretation are also described in detail. In the source plasma of the investigated NBI sources, atomic and molecular radiation was analysed in order to derive various plasma parameters such as the electron temperature and density, the atom to molecule ratio, the gas temperature and the vibrational population of hydrogen molecules. The extracted ion beam was analysed with  $H_\alpha$  Doppler spectroscopy in order to derive the ion species distribution.

### 3.1 Spectroscopic systems

The standard design for visible range spectroscopy is the Czerny-Turner set-up that can be seen in Fig. 3.1. The light can be coupled either directly into the entrance slit, or by optical fibres. It can be detected with either single channel (e.g. photomultiplier tubes) or multi channel devices, e.g. photo diode arrays (PDAs) or CCDs. Two-dimensional detector arrays even allow for spatially resolved measurements. The exposure time of the detector is usually defined by an electromechanical shutter. A detailed overview of different types of spectroscopic systems can be found e.g. in [Beh00].

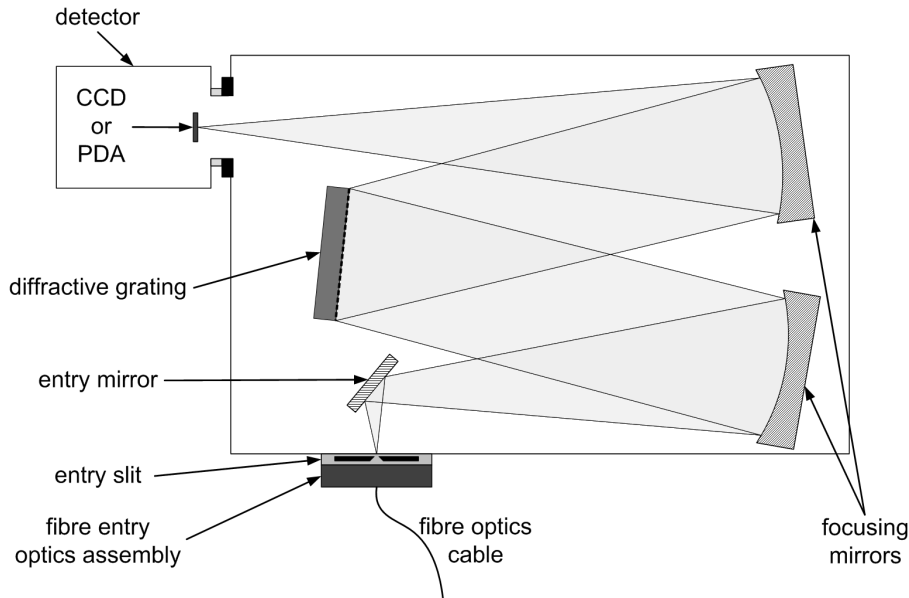


**Figure 3.1:** Czerny-Turner spectrograph (schematic).

A number of different spectroscopic systems were used here. The main reason for this is that spectrometers are usually very delicate and are not designed for mobility. Additionally, the use of different systems made it possible to analyse the emission spectra in different resolutions, and to cross-check the results. All spectroscopic systems were intensity calibrated either relatively or absolutely with the method described in section 3.2.

The spectrograph at the JET neutral beam test bed is a  $f = 500$  mm Czerny-Turner spectrograph of type SPEX 500M. Its diffractive grating has 1800 lines/mm. Information about the grating's blaze could not be obtained. Its wavelength drive was controlled by a SPEX Minidrive 2 controller. The detector is a 410 x 600 pixel Wright Instruments CCD camera with a 16 bit dynamic range. It has thermoelectric/air cooling and a PC interface. When the spectrometer was initially set up, the positions of entrance slit and camera were exchanged due to the available space. The spectrometer is located in the NBTB control room and coupled to the experiment inside the radiation shielded "Hot Cell" with 24 optical fibres (approximate length: 50 m). These are connected to a switchboard with SMA couplings on the spectrometer side which provide an interface for the spectrometer entry optics assembly. The initial assembly with 24 channels and a camera objective was later replaced with a 12 channel assembly for the sake of more sensitivity (see section 4.3.2). On the experiment side, the fibres are connected to two focussed optical fibre arrays spatially mapping the Test Bed's neutral particle beam. Such an array is sketched in Fig. 3.2. The original entry

optics assembly had a similar design.

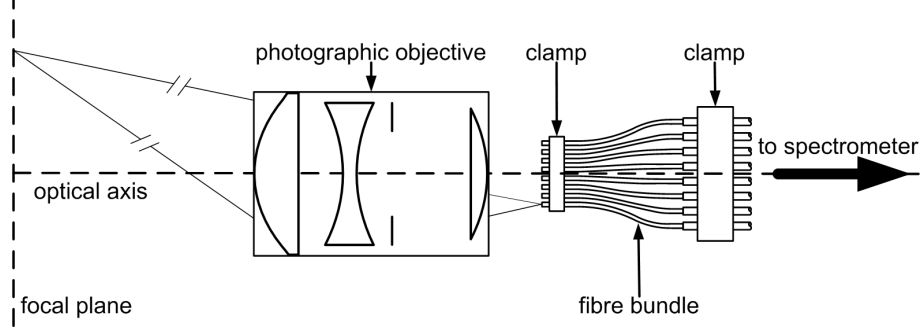


**Figure 3.2:** Multi-fibre optical arrangement at the JET NBTB.

There are 15 lines of sight across the vertical cross section of the beam, looking inside the NIB at a point near the neutraliser exit from a side mounted viewport at an angle of  $46.2^\circ$  upstream. 8 more lines of sight mapping the horizontal cross section use a viewport on the top of the NIB and are also looking at the neutraliser exit at an angle of  $47^\circ$  upstream. Two more fibres collect light from the neutraliser plasma perpendicular to the beam. These fibres do not have collimating or focussing optics. A viewport for the ion source is also planned.

Both the source plasma and the neutraliser at the ASDEX Upgrade RF source were observed with a Czerny-Turner spectrograph of the type Acton SP750i. Its focal length is 750 mm, and it has a diffraction grating with 1800 lines/mm (500 nm blaze). Its detector is a Roper Scientific CCD camera with thermo-electric/air cooling and 1024 x 1024 pixels. The dynamic range of the camera is 16 bit. The entrance slit is set to  $35\ \mu\text{m}$ . Although this spectrometer is set up for multichannel recording for high spatial resolution Doppler spectroscopy (20 channels) for the negative hydrogen ion source experiment MANITU [Lor05], only one channel (#5) was used here. The optical access to the ion source was provided by the viewport for an optical interlock that shuts down the RF generator if the plasma does not ignite or is unexpectedly extinguished. A Y-Splitter was inserted between the optical fibre and the photo diode for this interlock to couple light to the spectrometer.

At the GLADIS test bed, two independent spectrometers with different characteristics were available, one for spectroscopy of the source plasma and one for  $H_\alpha$  Doppler spectroscopy of the extracted beam. The spectroscopic measurements of

the source plasmas were done with an ANDOR Shamrock SR303i ( $f = 0.3$  m) Czerny-Turner spectrograph. This spectrograph is equipped with three interchangeable gratings mounted on an on-axis turret (see Fig. 3.3).

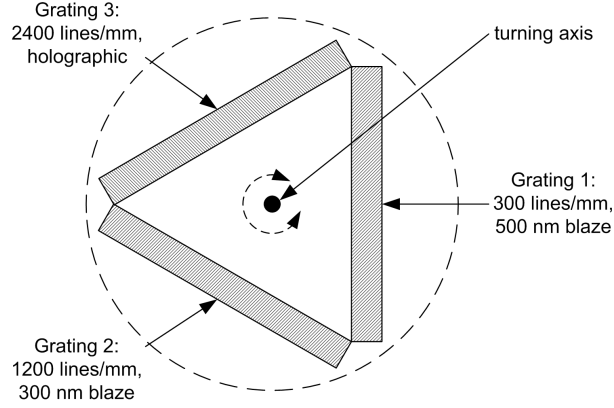


**Figure 3.3:** Triple grating turret with on-axis mounting as it is used in the ANDOR SR303i.

The detector of this spectrometer is a thermoelectric/air cooled CCD camera with 1024 x 256 pixels (model: ANDOR iDus DV420OE) and a 16 bit dynamic range. The spectrometer is fitted with an entry optics mounting for 5 optical fibres. Here, only Channel 3 (centre) was used since it produces the best resolved spectra<sup>1</sup> and only one line of sight was available at the ion source.

Normally, the exposure time is defined by an electromechanical shutter, and the CCD chip is read out in 5 sections of about 40 rows that correspond to the individual fibres. Unfortunately, while setting up the spectrometer for the measurements at GLADIS, a malfunction of the shutter occurred. Because the measurement date was too close for a repair and could not be postponed due to the tight schedule for materials testing at the facility, it was decided to use the so-called “Full Vertical Binning” (FVB) mode of the camera: Here, all 256 rows of the camera are binned, and no shutter is used. Although this invoked a number of other problems such as stray light from the four unused channels interfering with the actual signal and a less clear definition of the exposure time, this was considered preferable to the risk of another shutter malfunction. The stray light problem was eliminated by taking several more exposures after the end of the plasma pulse and subtracting the spectra with and without plasma. The problem of additional exposure of the CCD during readout was considered bearable since the readout time was considerably smaller than the exposure time ( $\approx 10$  ms compared to 200 ms for grating 1 respectively 1500 ms for gratings 2 and 3).

<sup>1</sup>The other channels suffer some optical aberrations.

For the line of sight in the GLADIS ion source, a special optical arrangement was necessary. This set-up can be seen in Fig. 3.1. Normally, this viewport is used for an optical interlock similar to the one at the RF PINI. The spectrometer is coupled to the optical fibre for this interlock with an Y-splitter. At the high cycling rates used for materials testing at GLADIS, the window of this viewport suffers considerable stress from power loading by electrons streaming back from the extraction system. Therefore, it has to be shielded during nominal operation. This shielding is provided by an M6 pinhole in front of the diagnostics port that can be closed with a screw. In that case, only stray light through an elbow channel can be coupled to the fibre, which is sufficient for the interlock. For the spectroscopic measurements, the screw is removed and the indirect lighting is blocked by a metal cylinder inserted into the porthole. This shielding is provided by an M6 pinhole in front of the diagnostics port that can be closed with a screw. In that case, only stray light through an elbow channel can be coupled to the fibre, which is sufficient for the interlock. For the spectroscopic measurements, the screw is removed and the indirect lighting is blocked by a metal cylinder inserted into the porthole.

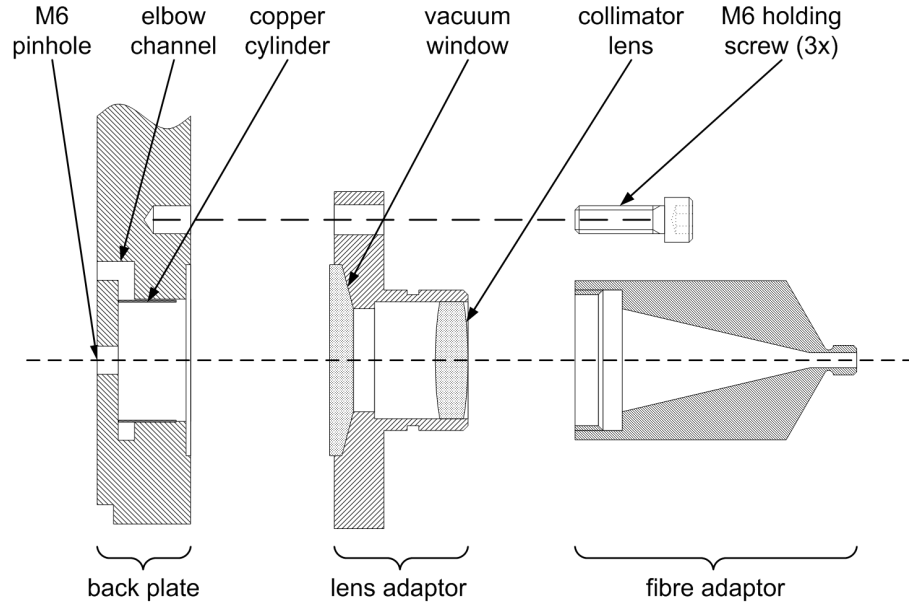


**Figure 3.4:** Optics assembly for the spectroscopy of the source plasma at GLADIS.

The Doppler spectroscopy of the ion beam was carried out with a system consisting of a SPEX 1870 ( $f = 0.5$  m) Czerny-Turner spectrograph with a 2400 lines/mm holographic grating and a row camera with a 1024 Si diode array (Princeton Instruments, type ST-120). The viewing angle of the Doppler spectroscopy line of sight relative to the observed ion beam is  $\approx 45^\circ$  downstream. The light is collected by a collimating lens head and transmitted to the spectrometer via fibre optics.

## 3.2 Calibration of the spectrometers

### 3.2.1 Wavelength Calibration

For the spectrometer at the NBTB, a wavelength calibration was performed with selected lines of a neon spectral lamp in the range between 350 nm and 810 nm. The spectrometer positions for the calibration were chosen in such a way that at least two spectral lines were visible in the observed wavelength range each time. The slope of a linear regression of the lines' peak pixel numbers versus their nominal wavelength returned the wavelength increment per pixel for a given central wavelength. The wavelength corresponding to the first pixel column of the CCD was derived by extrapolating the linear regression to  $x = 0$ .

To increase the accuracy of the calibration especially around the Balmer lines and to fill gaps in the above wavelength range that were not sufficiently covered by the neon spectrum (e.g. between 400 nm and 450 nm), a hydrogen lamp was also used. The first 5 spectral lines of the Balmer series were observed, and for each line the central wavelength was set to three different values, placing the line to the far left, exactly centred and to the far right of the CCD. The slope of a linear regression of the peak pixel number versus the nominal wavelength of the spectral line again returned the wavelength increment per pixel. The wavelength corresponding to the first pixel column was calculated by identifying the peak pixel number for the centred line with the nominal wavelength and extrapolating to zero using the slope obtained by shifting the line. The resulting values were assigned to the spectrometer position centring the line on the CCD. This resulted in two curves:

- Pixel 0 wavelength versus spectrometer position.
- Wavelength increment per pixel versus spectrometer position.

The pixel 0 wavelength was then fitted with a linear function, the increment with a quadratic function in order to interpolate the calibration curves to arbitrary central wavelengths. The calibration curves can be seen in Fig. 3.5. The fit parameters for the wavelength calibration function are listed in Tab. A.10 in the appendix.

For the beam spectrometer at GLADIS, a wavelength calibration was performed for a central wavelength of 660.1 nm with the  $H_\alpha$  line of a hydrogen lamp. This was done in the same way as described for the JET NBTB spectrometer.



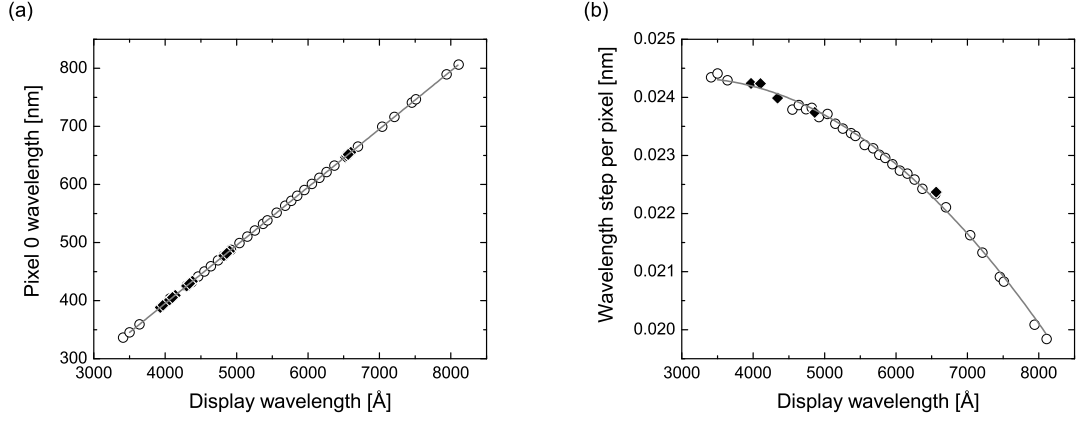


**Figure 3.5:** JET NBTB spectrometer wavelength calibration curves. (a) Pixel 0 wavelength, (b) Wavelength increment per pixel. Open circles represent calibration measurements with a Ne lamp, filled diamonds with a H<sub>2</sub> lamp. Gray lines represent fitted curves.

The Acton SP750i and the ANDOR SR303i both had a valid wavelength calibration already. Because the ANDOR SR303i had to be moved in order to be set up at GLADIS, its calibration was checked at random wavelengths with a low pressure mercury lamp. The small deviations that occurred were corrected by adjusting the counter offset of the wavelength drive.

### 3.2.2 Intensity calibration

All spectrometers also received an intensity calibration. Intensity calibrations are done by comparing the spectrometer's output signal with a standard continuum light source whose intensity spectrum is known. In the visible spectrum, this can be for example a tungsten ribbon lamp or an integration sphere illuminated by tungsten halogen lamps. In the (near) UV region, deuterium arc lamps are frequently used. For a relative calibration, the spectroscopic system's sensitivity is referenced to a certain wavelength. It makes the measurement of spectral line ratios possible. An absolute calibration requires a standard light source calibrated in absolute units, commonly measured either as spectral luminance  $L_\lambda$  [ $\text{lm m}^{-2} \text{nm}^{-1} \text{sr}^{-1}$ ] or spectral radiance  $\epsilon_\lambda$  [ $\text{W m}^{-2} \text{nm}^{-1} \text{sr}^{-1}$ ]. An overview over the possible realisations of radiation standards is given in [Beh00].

Absolute calibrations also have to be done with all optical components (i.e. lenses, fibres, windows etc.) in place. This optical set-up must not be changed in order for the calibration to remain valid.

All spectral radiance calibrations were performed with an integration sphere. Additionally, the spectral radiance  $\epsilon_\lambda$  was converted into the spectral photon count rate  $\dot{N}_\lambda$  [ $Photons\ m^{-2}\ nm^{-1}\ sr^{-1}\ sec^{-1}$ ] since this unit is more intuitive for calculating the particle densities of light emitting atoms or molecules. Assuming isotropic radiation, the radiation into the full solid angle  $4\pi$  is obtained simply by multiplication with  $4\pi$ . Typical error margins for the absolute intensity calibrations are assumed to be in the order of  $\pm 10\%$ .

### Acton SP750i at ASDEX Upgrade

The Acton SP750i spectrometer at ASDEX Upgrade was calibrated only relatively<sup>2</sup>. The resulting calibration factors can be seen in Fig. 3.6, the relative sensitivities of the centre pixel for each calibrated central wavelength  $\lambda_c$  are listed in Tab. 3.1.

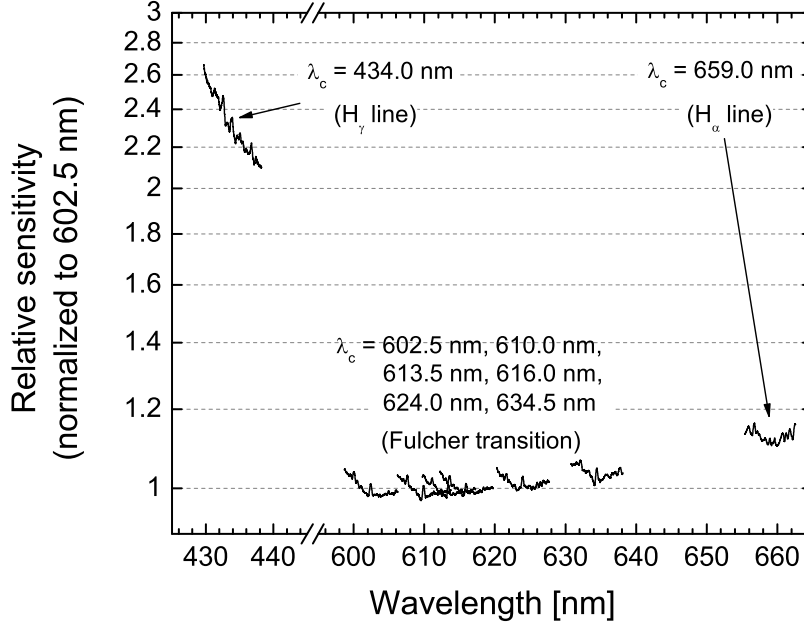


**Figure 3.6:** Relative intensity calibration curves for the Acton SP750i spectrometer at the ASDEX Upgrade NBI. Normalized to the value at 602.5 nm. The structure of the individual curves reflects the pixel sensitivity of the CCD camera.

<sup>2</sup>In this case, this means that the relative sensitivity of a single spectrometer channel was determined for different wavelength ranges.

**Table 3.1:** Relative sensitivity of centre pixels for the spectrometer at ASDEX Upgrade. Normalised to  $\lambda_c = 602.5$  nm.

$\lambda_c$ [nm]	centre pixel [relative]
434.0	2.33
602.5	1.00
610.0	1.00
613.5	1.00
616.0	1.00
624.0	1.01
634.5	1.04
659.0	1.12

An absolute calibration at ASDEX Upgrade was not possible because the vacuum window at the ion source could not be removed. A possible coating of this window with sputtered copper from the metallic components inside the ion source would have a strong effect on the absolute transmissivity. The relative transmission curve is only slightly affected by such a coating, however [Mai07]. The optics at the neutraliser were not accessible. The relative calibration was therefore estimated by the calibration for the optical system at the ion source.

Using the noise level of the spectra acquired for the calibration as a guideline, the uncertainty of the relative calibration can be estimated to be about  $\pm 5\%$  for each central wavelength.

### **SPEX 1870 at GLADIS**

A relative intensity calibration was sufficient for the beam line spectroscopy at GLADIS. It was performed in the same way as for the Acton SP750i at ASDEX Upgrade, but only for a central wavelength of 660.1 nm. This covers all possible Doppler shifts of the  $H_\alpha$  line (see section 3.7) as well as the unshifted line at GLADIS. The result is shown in Fig. 3.7.

The noise level of the calibration curve results in an estimated uncertainty of approximately  $\pm 3\%$ .

### **SPEX 500M at the JET NBTB**

The SPEX 500M at the JET NBTB was calibrated absolutely. All optical com-

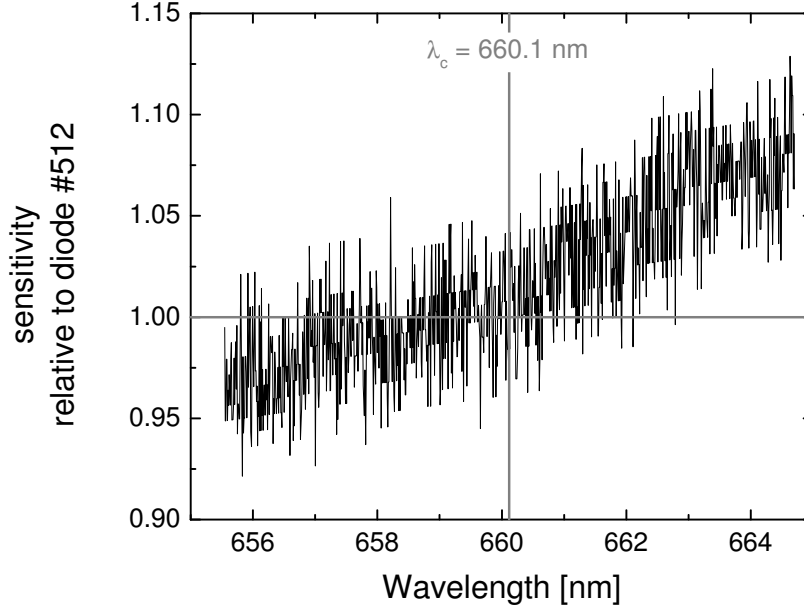


**Figure 3.7:** Relative sensitivity curve of the beam spectrometer at GLADIS for a central wavelength of 660.1 nm.

ponents including vacuum windows were arranged in a mock-up of the actual measurement set-up. This was especially difficult at the JET NBTB because the experiment-side optics had long focal lengths (2.84 m for the vertical and 5.22 m for the horizontal array). At GLADIS, the arrangement shown in Fig. 3.1 was recreated by placing a 6 mm aperture in front of the lens.

The intensity calibration at the JET NBTB was performed for 12 channels of the vertical array and for 6 channels of the horizontal one. A listing of the calibrated channels can be found in Tab. A.11 in the appendix. The calibration was performed for 9 different spectrometer positions covering the  $H_\alpha$  to  $H_\delta$  Balmer lines as well as the Q branches of the vibrational bands  $0 \rightarrow 0$  to  $3 \rightarrow 3$  of the Fulcher transition of the  $H_2$  (resp.  $D_2$ ) molecule as stated in Tab. 3.2.

The calibration curves of three different horizontal and vertical channels can be found in Figs. 3.8 and 3.9. The shape of the individual curves represents the CCD sensitivity. They were smoothed in order to reduce the noise level.

**Table 3.2:** Central wavelengths for the spectral radiance calibration at the JET NBTB. The wavelength controller displays the central wavelength in Å.

SPEX Position	Description
6530 Å	H $_{\alpha}$ / D $_{\alpha}$ lines and Doppler shifted lines
6350 Å	H $_2$ Fulcher band Q 3→3
6250 Å	H $_2$ Fulcher band Q 2→2; D $_2$ Fulcher band Q 3→3
6150 Å	H $_2$ Fulcher band Q 1→1; D $_2$ Fulcher band Q 2→2
6080 Å	D $_2$ Fulcher band Q 1→1
6030 Å	H $_2$ Fulcher band Q 0→0; D $_2$ Fulcher band Q 0→0
4860 Å	H $_{\beta}$ / D $_{\beta}$ lines
4340 Å	H $_{\gamma}$ / D $_{\gamma}$ lines
4100 Å	H $_{\delta}$ / D $_{\delta}$ lines

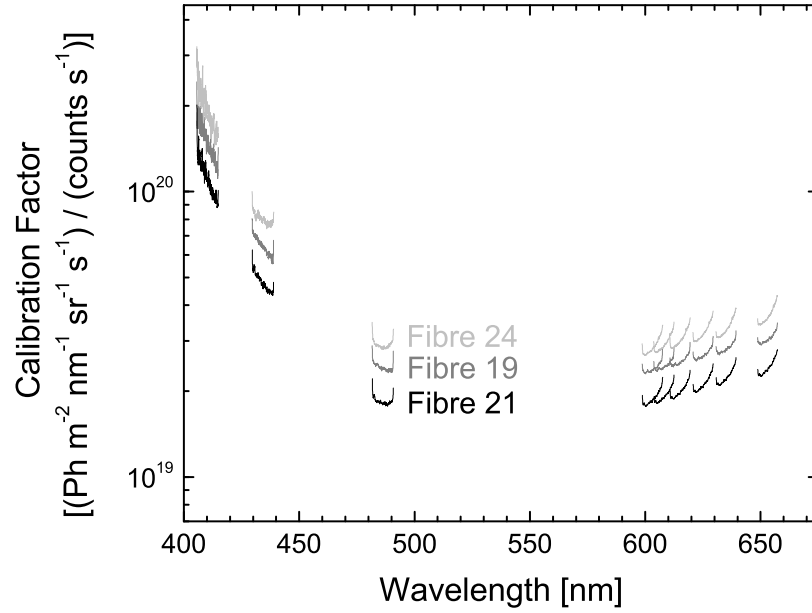


**Figure 3.8:** JET NBTB spectrometer absolute calibration curves: horizontal array. Exemplary for edge (fibres 19 and 24) and centre (fibre 21) fibres. All curves have been smoothed.

**ANDOR SR303i at GLADIS** For the ANDOR SR303i at GLADIS an absolute intensity calibration in FVB mode was performed with an integration sphere. For this calibration, the optical arrangement shown in Fig. 3.1 was recreated by placing a 6 mm aperture in front of the lens at the same distance as in the original set-up.

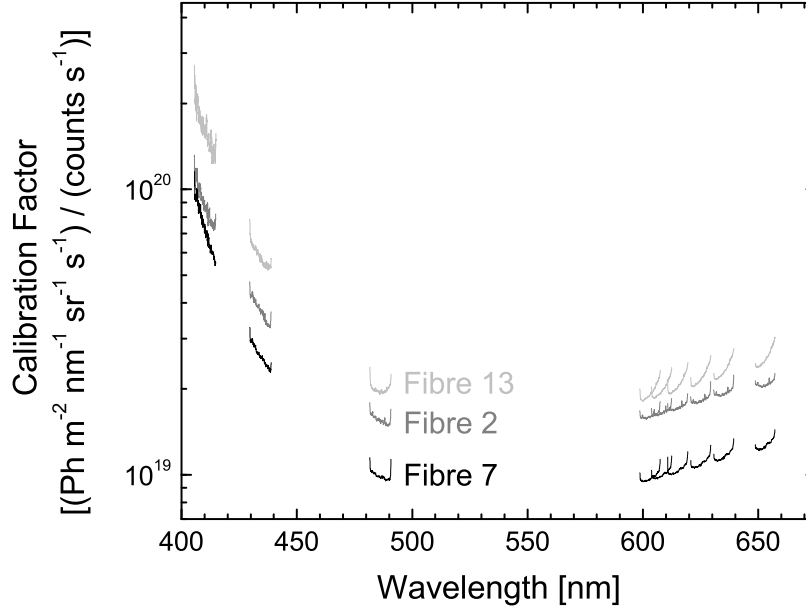


**Figure 3.9:** JET NBTB spectrometer absolute calibration curves: vertical array. Exemplary for edge (fibres 2 and 13) and centre (fibre 7) fibres. All curves have been smoothed.

While evaluating the calibration measurements, an inconsistency of the relative calibration between the three gratings became apparent. When applying the calibration to a plasma measurement, the same spectral line was measured with significantly different intensity values by each grating. The scaling factor was the same for each of the measurements taken at GLADIS, but varied for different central wavelengths. Furthermore, it turned out that a control measurement with one of the gratings showed a significant discrepancy when compared to its equivalent. Because of this, a recalibration was attempted, but failed since the spectrometer had already been prepared for transport in the meantime and the alignment of the entry optics had been disturbed in the process. However, measurements revealed significant drifting of the calibration lamp's signal as well as of the background signal over time. The background signal's drift could not fully explain the difference in calibration signal. Measurements with permanently closed shutter also showed a strong drifting of the CCD camera's dark current. Since at least the relative calibration factors measured with Grating 1 were considered reliable, as with this grating the whole observed wavelength range from approximately 300 nm to 640 nm was observed at once, the calibration factors for the other gratings were scaled in such a way that when applied to any one spectrum, all three gratings showed the same line radiance when integrating over the same

spectral line. The comparison of the atom to molecule ratio from absolute and relative spectroscopic measurements (see sections 3.4 and 3.6) finally fixed the absolute value. This value was also backed by the comparison of the  $\text{H}_2$  molecule density derived from gas pressure measurements and absolute spectroscopic measurements of the Fulcher band. Fig. 3.10 shows the original and the corrected calibration curves for all three gratings.

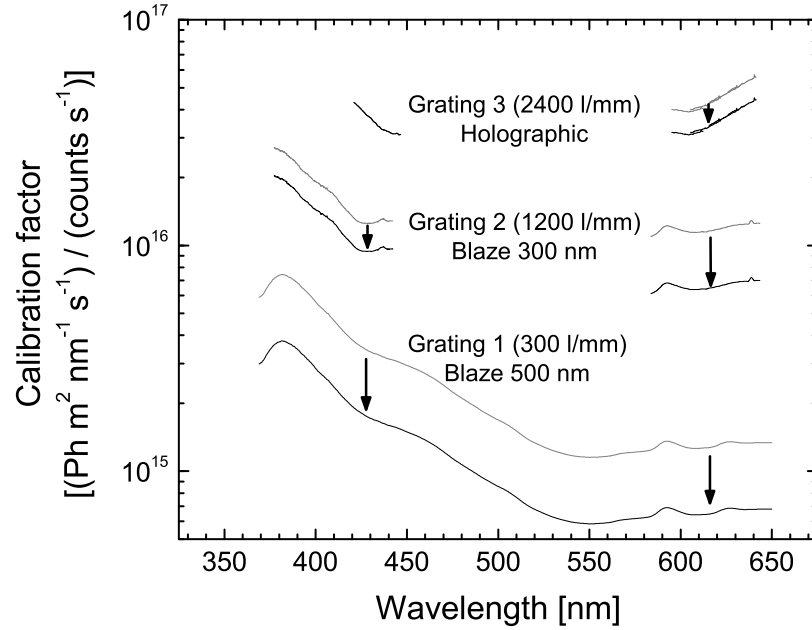


**Figure 3.10:** Intensity calibration curves for the ANDOR spectrometer at the GLADIS test bed. Black lines are the final corrected calibration factors, grey lines represent the initial, i.e. unscaled, factors.

Because of these problems, extensive laboratory tests were conducted in order to verify the reliability of the spectrometer. They revealed that the scaling factors between the three gratings indeed produced the correct sensitivity ratios, whereas the unscaled calibration did not. Furthermore, a light leak in the CCD camera was found. While this leak has negligible effects on strong measured signals, it poses a significant uncertainty when an absolute calibration is performed in the blue to UV wavelength regions where only small signals can be obtained from a tungsten halogen light source. For the spectra of the GLADIS source plasma, the effect of the light leak can be considered small since signals were intense and background spectra were taken immediately after each pulse, so that changing ambient light conditions can be neglected.

### 3.3 The emission spectrum of a plasma

This section gives a general introduction on how the emission spectrum of a plasma comes about and how it can be modelled. For this, the concepts of rate coefficients and optical thickness are explained. Two important plasma models are also briefly introduced: the corona model and collisional radiative models. A more detailed description this can be found in [Beh01].

A detailed description of the method that was used for the evaluation of the spectrum of atomic hydrogen can be found in section 3.4. Section 3.5 gives a detailed explanation of the distinctive features of molecular spectra. The focus is laid on the hydrogen Fulcher band and how it was interpreted. Section 3.7 explains how the ion species distribution was derived from spectroscopic measurements of the extracted beam.

#### 3.3.1 Rate coefficients

In the most general case, densities of particle species, photons and excited states can be calculated using *rate equations*: these are equations of continuity where the source and sink terms are determined by the densities of the participating particle species and a *rate coefficient*  $X$ :

$$\frac{dn}{dt} = \sum_{sources} \left[ \left( \prod_{\alpha} n_{\alpha} \right) \cdot X_{sources} \right] - \sum_{sinks} \left[ \left( \prod_{\beta} n_{\beta} \right) \cdot X_{sinks} \right]. \quad (3.1)$$

The products are to be read in the way that they include all densities  $n_{\alpha}$  respectively  $n_{\beta}$  participating in a particular source or sink process for the density of the species of interest,  $n$ .

A rate coefficient is a measure for how many reactions will take place per time interval for given densities. In the case of a binary collision, a rate coefficient  $X$  is obtained by a convolution of a (usually velocity dependent) cross section  $\sigma(v)$  and the relative velocity  $v$  over the complete velocity distribution  $f_T(v)$  (which is, in the easiest case, Maxwellian):



$$X(T) = \langle v \sigma(v) \rangle_T = \int d^3v f_T(v) v \sigma(v). \quad (3.2)$$

Since  $f_T(v)$  generally varies with temperature<sup>3</sup>, so does  $X$ .

A very important rate equation for spectroscopy is the *radiation transport equation*. It is a general formulation for the evolution of the spectral radiance  $L_\nu$  as the light travels through the plasma:

$$\frac{dL_\nu}{dl} = \epsilon_\nu - \alpha_{eff}(\nu)L_\nu. \quad (3.3)$$

Here,  $\epsilon_\nu$  is the spectral emissivity.  $\alpha_{eff}(\nu)$  is the effective spectral absorption coefficient, i.e. absorption reduced by stimulated emission.

Introducing the so-called *source function*  $S_\nu = \epsilon_\nu/\alpha_{eff}(\nu)$  and the *optical thickness*  $\tau(\nu)$  with the *optical depth*  $d\tau = \alpha_{eff}(\nu)dl$ , (3.3) can also be written as:

$$\frac{dL_\nu}{d\tau} = S_\nu - L_\nu. \quad (3.4)$$

Integrating (3.4) yields (for a plasma with length  $l$ ):

$$L_\nu = S_\nu \cdot (1 - e^{-\tau(\nu)}) \text{ with } \tau(\nu) = \alpha_{eff}(\nu) \cdot l. \quad (3.5)$$

From this, the limit cases of the optical thickness can now be easily seen: For  $\tau(\nu) \rightarrow \infty$  the exponential term vanishes, and (3.5) yields the equilibrium case, i.e. the Planck law. Such a spectral line is called *optically thick*. For  $\tau(\nu) \rightarrow 0$  the line is called *optically thin*. Here the exponential term can be approximated in first order by its argument  $-\tau(\nu)$ , and the spectral radiance  $L_\nu$  increases with the observed plasma length  $l$ . A method to consider a finite optical thickness  $\tau(\nu)$  are so-called *escape factors*  $\Theta$ . For the hydrogen atom, this is described in detail by [BF00]. In many low pressure plasmas, most lines are optically thin, although certain resonance lines (e.g. the Lyman series in a hydrogen plasma) which have a strong absorption coefficient may still be optically thick. These resonance lines can significantly influence the distribution of excited states [BF00].

---

<sup>3</sup>In the case of non-equilibrium plasmas, there may be different temperatures for each particle species.

In the general case, to fully describe a plasma, the rate equations for every single particle or state occurring in the plasma have to be solved simultaneously, which is often impossible since not all theoretical rate coefficients are available with sufficient precision. Therefore, to get a result nonetheless, plasma models for different equilibrium and non-equilibrium states have to be used.

### 3.3.2 Plasma Models

A relatively simple model is possible for plasmas with a low electron density (e.g. the solar corona with  $n_e \approx 10^{12} \text{ m}^{-3}$ ). Here, three body recombination and electron impact de-excitation become negligible compared to radiative recombination and spontaneous emission, respectively. Also, the vast majority of the particles are in the electronic ground state at a given time. Therefore, the simplest *corona equilibrium* can be defined by solely balancing electron impact ionisation with radiative recombination and electron impact excitation with spontaneous emission:

$$n_Z n_e X_{ion}^Z = n_{Z+1} n_e X_{rec}^{Z+1} \quad (3.6)$$

$$n_{Z,0} n_e X_{0 \rightarrow k}^Z = n_{Z,k} \sum_{l < k} A_{kl}. \quad (3.7)$$

Here,  $Z \geq 0$  is the particle species with charge  $Z$ . The indices  $0, k, l$  represent ground and excited states of  $Z$ . The rate coefficients for electron impact ionisation, radiative recombination and electron impact excitation are named  $X_{ion}^Z$ ,  $X_{rec}^{Z+1}$  and  $X_{0 \rightarrow k}^Z$ , respectively.  $A_{kl}$  is the Einstein coefficient for spontaneous emission leading to a transition  $k \rightarrow l$  with  $l < k$ . This leads to the Corona ionisation balance

$$\frac{n_{Z+1}}{n_Z} = \frac{X_{ion}^Z}{X_{rec}^{Z+1}}. \quad (3.8)$$

in which is independent from the electron density.

The density of an excited state  $k$  can be calculated as

$$n_{Z,k} = \frac{n_{Z,0} n_e X_{0 \rightarrow k}^Z}{\sum_{l < k} A_{kl}}. \quad (3.9)$$

From this, the line emission coefficient  $\epsilon_{km}$  can be calculated.  $\epsilon_{km}$  is the spectral emission coefficient  $\epsilon_\nu$  integrated over the whole spectral line corresponding to the transition  $k \rightarrow m$ . Since each transition event  $k \rightarrow m$  corresponds to one photon of energy  $h\nu$  emitted, and the rate of transitions is  $\dot{N}_{k \rightarrow m} = n_{Z,k} \cdot A_{km}$ , it is given by

$$\epsilon_{km} = \frac{h\nu}{4\pi} n_{Z,0} n_e X_{0 \rightarrow k}^Z \frac{A_{km}}{\sum_l A_{kl}} \quad (m, l < k). \quad (3.10)$$

(The factor  $1/4\pi$  is necessary because  $\epsilon_{km}$  is by definition measured per solid angle.)

The ratio  $A_{km}/\sum_{l < k} A_{kl}$  is also called the *branching ratio*  $b_{km}$ . It can be merged with the excitation rate coefficient  $X_{0 \rightarrow k}^Z$ ; this product is then called *emission rate coefficient*  $X_{k \rightarrow m}^Z$  and describes the whole process of spontaneous emission following electron impact excitation from the ground state for a specific spectral line [Fan01].

While the Corona model holds well for low electron densities, ever more processes become important when  $n_e$  rises. The consideration of all these effects ultimately leads to *collisional radiative models (CRMs)*. Here, a large number of rate equations has to be solved simultaneously to calculate the particle species densities in a plasma and the emitted radiation. This is done in computer models. In a first step, population coefficients  $R_s(k)$  are calculated, where  $s$  is the initial and  $p$  the final particle species or state. With given absolute source densities  $n_s$ , absolute final state densities  $n(k)$  can then be calculated:

$$n(k) = n_e \sum_{s=1}^N n_s \cdot R_s(k). \quad (3.11)$$

The population coefficients  $R_s(p)$  generally depend on  $T_e$ ,  $n_e$  and other plasma parameters.

From these densities  $n(k)$ , so-called *effective rate coefficients*  $X^{eff}$  can be calculated in analogy to the emission rate coefficients in (3.10):

$$X_{k \rightarrow m}^{eff} = \frac{n_k}{n_0 n_e} A_{km} = \frac{\sum_{s=1}^N n_s \cdot R_s(k)}{n_0} A_{km}. \quad (3.12)$$

The dependence of the population coefficients  $R_s(k)$  on the plasma parameter implicates the same dependences for  $X_{k \rightarrow m}^{eff}$ . The effective rate coefficients form

the basis of spectroscopic measurements of plasmas. Here, rate coefficients from the CRM described in [Wün04] were used to interpret the Balmer series radiation from the hydrogen atom.

### 3.4 Evaluation of the Atomic Spectrum with a Collisional Radiative Model

The available spectroscopic equipment was designed for visible range spectroscopy. For the hydrogen atom, the Balmer series is found in this wavelength range. This series of spectral lines was discovered in 1885 by Johann Jakob Balmer. It is the result of excited electrons in hydrogen atoms relaxing to the state with the main quantum number  $n = 2$ . The wavelengths  $\lambda$  of the Balmer lines are given by

$$\lambda_{m \rightarrow 2} = \left[ R_\alpha \cdot \left( \frac{1}{4} - \frac{1}{m^2} \right) \right]^{-1} ; (m \geq 3). \quad (3.13)$$

The lines are denoted with Greek indices for rising main quantum number  $m$  of the initial state, i.e.  $H_\alpha$ ,  $H_\beta$  and so on.  $R_\alpha$  is the Rydberg constant with the index  $\alpha$  denoting different nuclear isotopes, i.e. hydrogen, deuterium or also tritium. Because the mass of the nucleus is finite,  $R_\alpha$  depends on the nuclear mass according to

$$R_\alpha = \frac{\mu_\alpha e^4}{8\epsilon_0^2 c h^3}. \quad (3.14)$$

$\mu_\alpha = \frac{m_e + M_\alpha}{m_e \cdot M_\alpha}$  is the electron reduced mass;  $m_e$  is the free electron mass and  $M_\alpha$  is the mass of the nucleus. This means that for the heavier isotopes of hydrogen, the spectral lines are shifted slightly towards shorter wavelengths. For the Balmer  $H_\alpha$  and  $D_\alpha$  lines, this leads to a wavelength shift of 0.179 nm.

Analysing the Balmer series yields a multitude of information about the plasma. By measuring the absolute emissions of a line and knowing the appropriate effective rate coefficients, various plasma parameters can be derived. For example, the atom density  $n_H$  can be calculated by absolutely measuring the emitted photon count rate  $\dot{N}$  of a single Balmer line, e.g.  $H_\gamma$ , and dividing it by the effective emission rate coefficient  $X_{H \rightarrow H_\gamma}^{eff}(T_e, n_e)$  [Fan01]:

$$n_{\text{H}} = \frac{\dot{N}_{\text{H}_\gamma}}{n_e X_{\text{H} \rightarrow \text{H}_\gamma}^{\text{eff}}(T_e, n_e)}. \quad (3.15)$$

It should be noted that the  $\text{H}_\gamma$  radiation may also partly originate from other mechanisms, for example dissociative excitation. In that case, the measured radiation  $\dot{N}_{\text{H}_\gamma}$  has to be corrected by this contribution. The plasmas in NBI ion sources have atom to molecule ratios of more than 0.05. Considering that the rate coefficient for dissociative excitation is by more than two orders of magnitude smaller than for electron impact excitation [BF00], this means that the electron impact excitation dominates in this case.

There is also the possibility measuring line ratios, especially if only a relative calibration of the spectroscopic system is possible. In thermal equilibrium, this yields the electron temperature due to the Boltzmann law of excited state densities

$$\frac{n_k}{n_l} = \frac{g_k}{g_l} e^{\frac{\Delta E_{kl}}{k_B T_e}}, \quad (3.16)$$

where  $k$  and  $l$  designate the initial and final states and  $g_{k,l}$  the associated statistical weights.  $\Delta E_{kl}$  is the energy gap between the two states. The Boltzmann law can be applied to derive the temperature of any *thermal* population, e.g. also the rotational population of molecular states (see section 3.5.3). For electronic states in a non equilibrium plasma, line ratios have to be compared to the ratios of the appropriate effective rate coefficients.

Re-absorption of resonance lines, i.e. the Lyman series, leads to an increased population of excited states. Accordingly, if the Lyman series becomes optically thick, this also affects the absolute emissivities as well as the line ratios of the Balmer lines. Correction factors for this effect were derived in [BF00]. This correction is smaller for the  $\text{H}_\gamma$  line than for the  $\text{H}_\alpha$  and the  $\text{H}_\beta$  lines.

For the estimation of electron temperature and density, the absolute intensities of the Balmer lines  $\text{H}_\beta$ ,  $\text{H}_\gamma$  and  $\text{H}_\delta$  were compared to model calculations based on the collisional radiative model YACORA [Wün04].

The neutral particle densities  $n_{\text{H}_2}$  and  $n_{\text{H}}$  that are necessary for calculating absolute emissivities were derived by measuring the cold gas pressure  $p_{\text{source}}$  (i.e.

at room temperature and without plasma). Regarding the ion sources under investigation here, a constant gas flow is set by opening one from a set of valves, hence it is assumed that the initial density is given by  $n_0 = p_{\text{source}}/k_B T_{\text{room}}$ . For the particle densities in the plasma, this means

$$n_0 = \text{const.} = n_{\text{H}_2} + 2n_{\text{H}}. \quad (3.17)$$

This equation was taken as the boundary condition for the neutral particle densities. The electron temperature  $T_e$ , the electron density  $n_e$  and the atom to molecule ratio  $\Delta_a$  were then determined in an iterative procedure. First, “reasonable” starting values for  $T_e$  and  $n_e$  were assumed. An electron temperature of  $T_e \approx 6$  eV was chosen for two reasons: First, the electron temperature was expected to be relatively high. Second, the variation of the rate coefficients for the Balmer lines with  $T_e$  is only minor for 6 eV or higher. With this temperature, the starting value for  $n_e$  was derived from the intensity ratio  $\text{H}_\beta/\text{H}_\gamma$ . The measurement of the ion species distribution by  $\text{H}_\alpha$  Doppler spectroscopy of the extracted beam (see section 3.7) provided an independently measured fixed ratio of the  $\text{H}_2^+$  density and the electron density.

The atom to molecule ratio and the electron density were then varied until the differences between measurement and model were minimized for both absolute intensities and line ratios. The electron temperature was kept fixed for this.

A run with a lower electron temperature than 6 eV yielded a less good agreement between model and measurement. This confirmed the initial assumption that  $T_e$  was indeed in the range of 6 eV or more. On the other hand, the insensitivity of the rate coefficients to  $T_e$  in this temperature range means that it was not possible to observe variations of  $T_e$  with the spectroscopic measurements.

The sensitivity of this evaluation method with respect to  $n_e$  and  $\Delta_a$  is very high. Because of this, the uncertainty of the results is governed by the uncertainty of the absolute calibration. It is therefore estimated to be in the range of  $\pm 10\%$  for both values.

**To summarise, the electron temperature and the electron density were derived by comparing the measured absolute intensities of the Balmer lines with a modelled spectrum from the collisional radiative model YACORA. The boundary conditions for the modelling were taken from pressure measurements and the measurement of the ion species distribution from the extracted beam. This evaluation method also yields**

values for the atom to molecule ratio  $\Delta_a$ . However, the main diagnostic for this value is the comparison of atomic and molecular radiation. It is described in section 3.6.

## 3.5 Emission Spectrum of the Hydrogen Molecule

### 3.5.1 Nomenclature for Molecular States

The energy level spectrum of the hydrogen molecule is much more complex than that of the hydrogen atom. One major difference is that the electronic states of a hydrogen molecule are divided into a spin-singlet and a spin-triplet system because two electrons are present in the molecule. Transitions between the two spin multiplets are dipole forbidden. The other major change is the presence of two nuclei. This leads to rotational and vibrational states, and also to a distinguished spatial direction, namely the connection axis between the nuclei.

There are several nomenclatures for describing these features. In the one used here [Beh00], states in the spin multiplet of the ground state  $X$  (for hydrogen, the singlet system) are named with capital Roman letters. States from other multiplets (in hydrogen the triplet system) are labelled with lower case letters. The spin multiplicity is stated by a raised number right of this letter (in the case of hydrogen, “1” respectively “3” for singlet respectively triplet states), e.g.  $X^1$  or  $d^3$ . The next symbol states the projection  $\Lambda$  of the total angular momentum of the electrons  $L$  on the molecular axis. Values of 0, 1, 2,... are indicated by the capital Greek letters  $\Sigma$ ,  $\Pi$ ,  $\Delta$  and so on in analogy to  $s$ ,  $p$ ,  $d$ , ... for single electron orbital angular momentums. Finally, the subscripts “ $g$ ” and “ $u$ ” state the parity (i.e. “even” or “odd”), and the superscripts “+” and “-” the symmetry of the wave function regarding.

For example, the ground state of the hydrogen molecule is given by  $X^1\Sigma_g^+$ , i.e.: the state named “X” in the singlet system (i.e. with spin multiplicity 1),  $\Lambda = 0$ , parity “even” and symmetry “+”.

Fig. 3.11 shows several electronic states of the hydrogen molecule. The Fulcher transition  $d^3\Pi_u \rightarrow a^3\Sigma_g^+$  that was measured here is also marked.

When describing a transition between two molecular states, the quantum numbers in the energetically higher state are indicated by a prime (e.g.  $J'$ ); the lower state has a double prime (e.g.  $J''$ ).

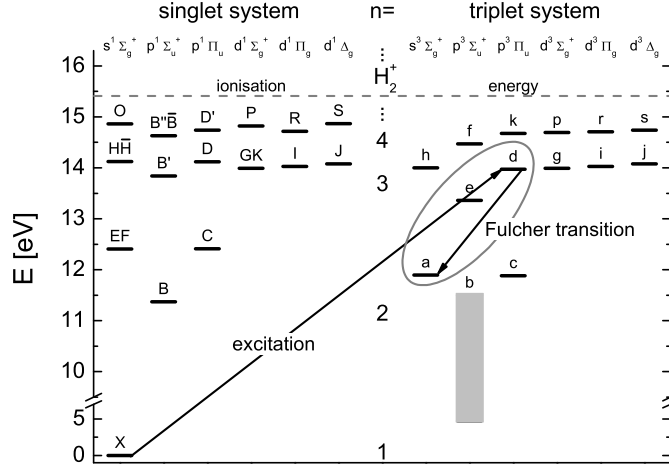


**Figure 3.11:** Selection of electronic energy levels in molecular hydrogen  $H_2$  [HH79]. The  $b^3\Sigma_u^+$  state is repulsive and expands up to infinity; its lower border corresponds to the potential energy for infinite nuclear distance. The symbols  $s, p, d$  in the second line from the top state the single electron angular momentums.

### 3.5.2 The Emission Spectrum of Diatomic Molecules

The total energy  $T$  of a specific molecular state can be written as the sum of the electronic term  $T_{el}(p)$ , the vibrational term  $G(v)$  and the rotational term  $F_v(J)$  [Hel89]:

$$T = T_{el}(p) + G(v) + F_v(J). \quad (3.18)$$

$p$  indicates an electronic state,  $v$  is the vibrational and  $J$  the rotational quantum number.  $T_{el}(p)$  is the minimum of the potential curve of a molecular electronic state  $p$ . These curves represent the potential energy of the molecule depending on the internuclear distance and the electronic state. For bound states, the potential curve has a minimum at the equilibrium distance. Several such potential curves of the hydrogen molecule are shown in Fig. 3.12.



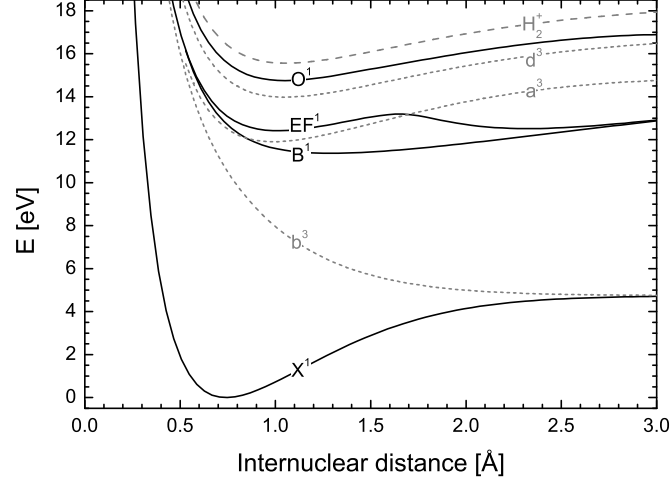


**Figure 3.12:** Several potential curves of molecular hydrogen  $H_2$  [FW06]. Note the different radial position of the minima of the potential curves.

The vibrational term  $G(v)$  in (3.18) can be calculated by assuming an anharmonic oscillator [Hel89]:

$$G(v) = \hbar \left[ \omega_e \left( v + \frac{1}{2} \right) - x_e \omega_e \left( v + \frac{1}{2} \right)^2 + y_e \omega_e \left( v + \frac{1}{2} \right)^3 - \dots \right]; \quad v = 0, 1, 2, \dots \quad (3.19)$$

$\omega_e$  is the eigenfrequency of the oscillator in the electronic state  $p$ ,  $x_e$  and  $y_e$  are the anharmonic constants and depend on the shape of the potential curve of the state  $p$ . The first term corresponds to the energy eigenvalues of a harmonic oscillator, but the anharmonic corrections cause a reduction in the energy gap between vibrational states with rising  $v$ . However, the number of vibrational states for a specific electronic state  $p$  is finite, unlike the number of electronic levels in an atom. Also, since the potential curves are asymmetric and flatten out for increasing internuclear distance, the mean distance increases with  $v$ . This can even lead to dissociation of the molecule and also influences the rotational spectrum. Fig. 3.13 shows a representation of the vibrational eigenfunctions for the  $H_2$  molecule. Their eigenvalues are represented by the limits towards zero respectively infinite internuclear distance and correspond to the  $G(v)$  term.

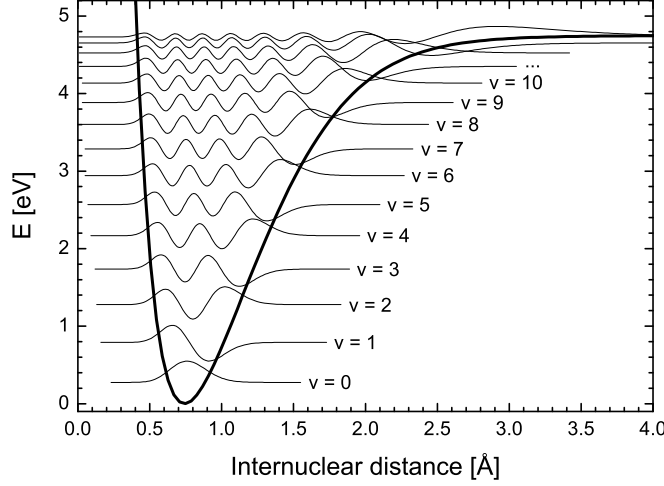


**Figure 3.13:** Vibrational eigenfunctions in the potential curve of the electronic ground state ( $X^1\Sigma_g^+$ ) of the  $H_2$  molecule [FW06]. Note that the vibrational eigenfunctions quantum number  $v$  is limited for a given electronic state, in this case to  $v_{max} = 14$ .

The rotational spectrum expressed by  $F_v(J)$  is the spectrum of a non-rigid, vibrating rotator. The energy levels of the non-rigid rotator (without the influence of vibration) can be expressed as [Hel89]

$$F(J) = hc [B_e J(J+1) - D_e J^2(J+1)^2 \pm \dots]; \quad J = 0, 1, 2, \dots \quad (3.20)$$

The rotational constant  $B_e$  and the centrifugal distortion constant  $D_e$  are molecule constants. They depend on the electronic state  $p$  because the equilibrium distance of the nuclei varies with  $p$ . On top of that comes the influence of the vibration. It can be expressed by modifying the rotational constants:

$$B_v = B_e - \alpha_e(v + \frac{1}{2}) + \dots \quad (3.21)$$

$$D_v = D_e + \beta_e(v + \frac{1}{2}) + \dots \quad (3.22)$$

and so on, whereas  $\alpha_e$  and  $\beta_e$  are molecular constants (also depending on  $p$ ) [Hel89].

The ro-vibronic transitions cannot occur without an electronic transition for an unpolar molecule such as  $H_2$ . This means that with the available equipment,

only the transitions between excited electronic states could be observed, and only in emission<sup>4</sup>. To understand the emission spectrum, it is first necessary to understand how the rotational and vibrational states of electronically excited states are populated.

The basic assumption for this is the *Born-Oppenheimer approximation*: the movement of the nuclei is considered slow on the time scale of electronic processes, e.g. excitation and photon emission. The internuclear distance is therefore considered fixed [Hel89]. As a consequence, the population density distribution  $n_{J''}$  from the ground state is conserved in the excited state. However, the rotational constants  $B_v$  are larger in the ground state with  $v = v'' = 0$  than for a given  $v = v'$  in the excited state. The reason for this is that the equilibrium distance of the nuclei is smallest in the ground state (see Fig. 3.12). It can be easily derived from (3.20) that the energy gap between two neighbouring rotational states is also larger in the ground state.

For a thermal distribution in the ground state, this means that in first order a rotational temperature in an excited state (e.g. the  $d^3\Pi_u$  state from which the Fulcher band originates) is scaled to the one in the ground state by the ratio of the rotational constants  $B_{v=0}(X^1\Sigma_g^+)$  and  $B_{v'}(d^3\Pi_u)$ :

$$T_{rot}^{v''=0}(X^1\Sigma_g^+) = \frac{B_{v''=0}(X^1\Sigma_g^+)}{B_{v'}(d^3\Pi_u)} T_{rot}^{v'}(d^3\Pi_u). \quad (3.23)$$

$T_{rot}^v$  is the rotational temperature corresponding to the vibrational state with quantum number  $v$  in the excited respectively ground state. Tab. A.9 in the appendix shows these scaling factors for the first four diagonal vibrational transitions in the Fulcher band for hydrogen and deuterium.

Basically, the rotational transitions can be classified into three branches by the change of the vibrational quantum number  $\Delta J = J' - J''$  according to the following selection rules [Hel89]:

- P branch:  $\Delta J = -1$
- Q branch:  $\Delta J = 0$
- R branch:  $\Delta J = +1$ .

---

<sup>4</sup>Absorption from the ground state is basically possible, but requires VUV radiation. A set-up for VUV absorption was not available, however.

Transitions with  $J' = J'' = 0$  are always forbidden.

Within a single given vibrational transition  $v' \rightarrow v''$ , the transition probability  $A_{J',J''}$  depends  $J'$  according to [Dra96]

$$A_{J',J''} \propto \frac{S'_J}{2J' + 1}. \quad (3.24)$$

$S'_J$  is the so-called *Hönl-London factor* or *theoretical line strength* for a transition in emission. It depends on the type of transition. For the P, Q and R branches of the Fulcher transition in hydrogen as well as in deuterium it is given by [Her53]

$$P \text{ branch : } S_{J'}^P = \frac{J'}{4}; \quad (3.25)$$

$$Q \text{ branch : } S_{J'}^Q = \frac{2J' + 1}{4}; \quad (3.26)$$

$$R \text{ branch : } S_{J'}^R = \frac{J' + 1}{4}. \quad (3.27)$$

As can be seen, the Q branch is more intense than the other two branches.

It should be mentioned that  $A_{J',J''}$  is also proportional to cubic of the frequency  $\nu$  of the transition  $J' \rightarrow J''$ . However, the frequency difference between the first five Q branch transitions within a vibrational band is very small compared to the absolute frequency  $\nu$ , so this dependence can be neglected here.

The statistical weight of a rotational state  $J$  is generally given by  $2J + 1$ . For molecular hydrogen however, there is an additional factor  $\gamma_{J'}$  that depends on the isotope, more precisely on the nuclear spins [Beh00]. The nuclei of the  $^1\text{H}$  isotope are fermions with spin  $1/2$ . Their total spin  $I$  can therefore be 0 or 1, with the  $I = 1$  variant called *ortho* and the  $I = 0$  variant called *para* hydrogen. The statistical weight of each species is given by  $2I + 1$ . Since the total molecular wave function has to be antisymmetric (i.e. fermionic), the rotational states with odd quantum number are occupied by ortho hydrogen, and the even ones by para hydrogen<sup>5</sup>. This results in alternating intensities resp.  $\gamma_{J'}$  for the rotational lines of  $\text{H}_2$  with a ratio of 3:1. The deuteron  $^2\text{D}$ , on the other hand, is a boson with spin 1. Possible combinations are  $I = 2, 1, 0$  with the statistical weights as before.

---

<sup>5</sup>This is only valid for the  $d^3\Pi_u^-$  state from which the Q branch originates. The P and R branch originate from  $d^3\Pi_u^+$ , where the occupation of states with odd and even  $J'$  by ortho and para hydrogen is reversed.

Hence the abundance of the para configuration is  $\frac{5+1}{3} = 2$  times the abundance of ortho, resulting in intensities in the  $D_2$  spectrum alternating like 1:2. The total statistical weight  $g_{J'}$  is thus given by  $\gamma_{J'} \cdot (2J' + 1)$ .

Considering all this, the emissivity  $\dot{N}$  of a rotational line is given by

$$\dot{N} = n_{J'} A_{J'J''} \propto n_{J'} \gamma_{J'} S_{J'}. \quad (3.28)$$

The Born-Oppenheimer approximation is also used for the population of vibrational states, i.e. the nuclei are again considered immobile during an electronic transition [Her53]. As can be seen in Fig. 3.14, the vibrational eigenfunctions are shifted together with the potential curves of different electronic states. Graphically, this means that an electronic transition is represented by a vertical line in Fig. 3.14.

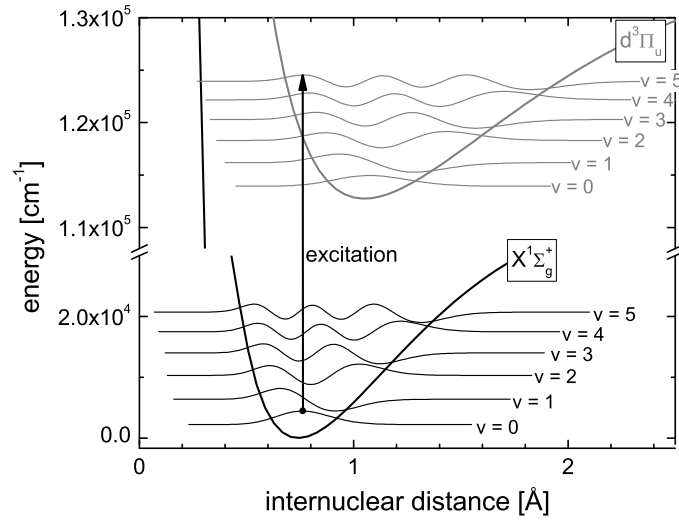


**Figure 3.14:** Some vibrational eigenfunctions in the ground state  $X^1\Sigma_g^+$  and the  $d^3\Pi_u$  state of  $H_2$  [FW06]. The vertical arrow symbolizes excitation by electron impact.

In a more formal approach, the overlap integrals between vibrational states have to be calculated over the internuclear distance  $r$  [Dra96]:

$$q_{v''v'}^{p''p'} = \left| \int \Psi_{v''}^{p''} \Psi_{v'}^{p'} dr \right|^2, \quad (3.29)$$

with  $\Psi_{v''}^{p''}$  and  $\Psi_{v'}^{p'}$  denominating the vibrational eigenfunctions of the initial and final states. The square absolutes  $q_{v''v'}^{p''p'}$  of the overlap integrals are called *Franck-*

*Condon factors* are a (normalised) measure for the transition probability. If the matrix  $\left(q_{v''v'}^{p''p'}\right)$  of the Franck-Condon factors is non-diagonal, this means that during an excitation, the vibrational population  $n(v'')$  is redistributed into  $n(v')$ . This is for example the case for the excitation from the  $X^1\Sigma_g^+$  to the upper state  $d^3\Pi_u$  of the Fulcher transition. For the Fulcher transition  $d^3\Pi_u \rightarrow a^3\Sigma_g^+$  itself, the Franck-Condon matrix is almost diagonal because the equilibrium distance is nearly equal for the upper and lower state. This has the consequence that the diagonal transitions are the strongest ones.

Similar to rotational lines, the total intensity  $\dot{N}_{p'p''}^{v'v''}$  of a vibrational band is given by

$$\dot{N}_{p'p''}^{v'v''} = n_{p'}(v') A_{p'p''}^{v'v''}, \quad (3.30)$$

with the transition probability  $A_{p'p''}^{v'v''}$ . The transition probability is the result of the convolution of the appropriate Franck-Condon with the electronic transition dipole moment and is an absolute quantity. A detailed derivation and listing of Franck-Condon factors and transition probabilities for the hydrogen molecule and its isotopomers can be found in [FW06].

### 3.5.3 Evaluation of the Fulcher Transition

The Fulcher transition of the hydrogen molecule was used to measure the atom to molecule ratio in the source plasmas of the investigated ion sources. This was done by comparing of its total radiation with the emissivity of an atomic emission line. A detailed description for this can be found in section 3.6. This section explains how the vibrational population and the gas temperature were derived by performing vibrationally respectively rotationally resolved measurements. Both are important parameters for plasma modelling. Measured spectra of the Fulcher band in hydrogen and deuterium can be seen in Figs. A.1 and A.2 in the appendix. The molecular data that the evaluation is based on is compiled in Appendix A.2.

#### Gas temperature

It was assumed that the rotational population in the ground state  $X^1\Sigma_g^+$ ,  $v'' = 0$  of the hydrogen molecule is a thermal distribution that corresponds to the gas

temperature. This assumption is reasonable because the energy gap between the rotational states is much smaller than between electronic states. As described by (3.23), this temperature is linked to the rotational temperature of the  $d^3\Pi_u$  state. The rotational temperature of this state was derived from the measurement of the Q1 to Q5 rotational lines for the vibrational states  $v' = 0, 1, 2, 3$ . For this, the rotational population  $n_{J'}$  of  $d^3\Pi_u$  was calculated according to (3.28).  $n_{J'}$  was then plotted logarithmically over the energy of the rotational states  $J'$  (a so-called *Boltzmann plot*). The slope of a linear fit through the obtained data points yields the rotational temperature according to the Boltzmann law (3.16). The error margin of this fit yields the error margin for the rotational temperature.

One would expect that the rotational temperature of all four measured vibrational bands yield the same gas temperature when scaled to the ground state with (3.23). However, this is not the case: the resulting gas temperature drops with increasing  $v'$ , as has been shown e.g. in [Fan01]. When a trace of nitrogen is added to the plasma, the gas temperature obtained from the  $C^3\Pi_u \rightarrow B^3\Pi_g, v' = 0 \rightarrow v'' = 2$  transition of the nitrogen molecule. The best agreement with the evaluation of the Fulcher transition for  $H_2$  results for the  $v' = v'' = 2$  vibrational band. For  $D_2$ , the  $v' = v'' = 1$  yields the closest results [Fan01]. Nitrogen could not be added to the investigated ion source plasmas, however. Therefore, the gas temperature was derived from the  $v' = v'' = 2$  ( $H_2$ ) respectively  $v' = v'' = 1$  ( $D_2$ ) vibrational bands of the Fulcher transition .

### Vibrational population

The method used to derive a ground state vibrational population from molecular radiation is described by [Heg02]. A thermal population with a vibrational temperature  $T_{vib}$  is assumed in the ground state  $X^1\Sigma_g^+$  because the energy gap between the vibrational states is still small compared to electronic states. It is projected into the excited state  $d^3\Pi_u$  with the appropriate Franck-Condon matrix. In order to compensate for the lack of vibrationally resolved excitation rate coefficients, the mean rate coefficient for the  $X^1\Sigma_g^+ \rightarrow d^3\Pi_u$  transition is scaled by correction factors that depend on  $v''$ . These correction factors take into account that the threshold energy for the transition into a given vibrational state  $v'$  is smaller for a higher  $v''$ . This is done only for  $v'' = 1 \dots 5$  because higher vibrational levels in  $X^1\Sigma_g^+$  are only weakly populated. The procedure for calculating these factors as well as their values can be found in [FH98].

Using (3.30), a vibrational population  $n(v')$  is derived from spectroscopic measurements. The calculated and measured populations are normalised (usually to

$n(v' = 0)$ ) and compared. The ground state  $T_{vib}$  is then varied until they agree. If no such  $T_{vib}$  can be found, this can have two reasons: either the ground state vibrational population cannot be described by a vibrational temperature, or the population in the excited state is disturbed. This can be caused e.g. by depopulating processes such as predissociation and auto-ionisation that are not included in this model.

Examples of calculated populations of  $d^3\Pi_u$  for typical ground state vibrational temperatures in hydrogen and deuterium are shown in Fig. 3.15.

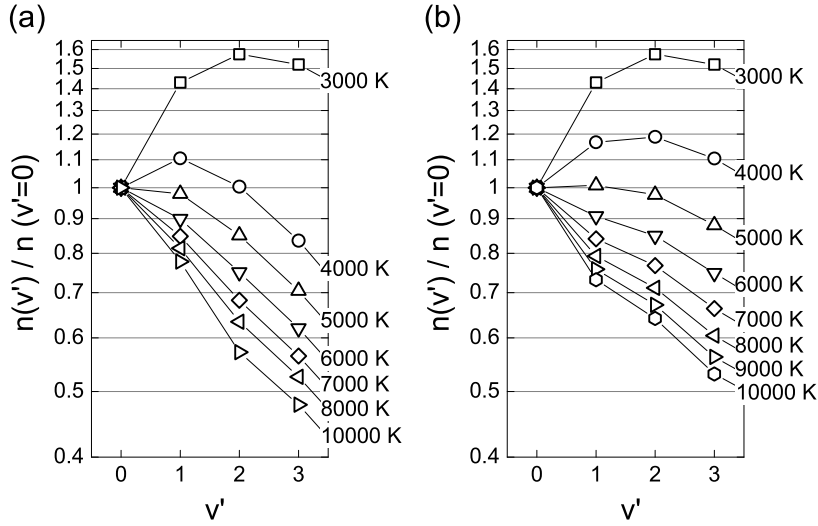


**Figure 3.15:** Calculated vibrational populations of  $d^3\Pi_u$  for hydrogen (a) and deuterium (b). The populations are normalised to  $n(v' = 0)$ .

The photon count rates  $\dot{N}_{v'v''}$ , and accordingly the populations  $n_{p'}(v')$ , are derived from scaling a single reference rotational line per vibrational band with a factor  $f_{v'}(T_{rot})$  depending on the rotational temperature  $T_{rot} = T_{rot}^{v'}(d^3\Pi_u)$  for this band. This factor is obtained by calculating the (relative) theoretical intensities of all rotational lines from the P, Q and R branches in this band for a given rotational temperature  $T_{rot}$  using equations (3.16) and (3.28). Their sum is then compared to the reference line. Here, for hydrogen the Q1 lines and for deuterium the Q2 lines were chosen as the reference lines, since these are among the most intense lines per band and also relatively undisturbed by other spectral lines of hydrogen. They were therefore considered to be the most accurately measurable ones.

In hydrogen, the resulting scaling factors  $f_{v'}(T_{rot})$  can be well approximated with a linear fit between 200 K and 1200 K, which is the relevant range for the measurements taken. In deuterium, a linear fit can be made between 200 K and 1200 K,



too. For low temperatures the curves for  $D_2$  diverge, however. The reason is the scaling to the Q2 line: for  $T_{rot} \rightarrow 0$ , the  $J' = 2$  rotational state is not populated anymore compared to  $J' = 1$ . Therefore, all lines originating from  $J' = 1$  are infinitely stronger than the Q2 line.

Plots of  $f_{v'}(T_{rot})$  against  $T_{rot}$  for  $v' = v'' = 0, 1, 2, 3$  can be found in the appendix (Figs. A.3 and A.4). The rate of photons emitted the vibrational band  $v' = v''$  is then obtained by multiplying the measured Q1 respectively Q2 intensity with the appropriate  $f_{v'}(T_{rot})$ , and the vibrational population according to (3.30).

To summarise this section, molecular spectra feature complex emission bands from combined electronic and ro-vibronic transitions. In the ground state, thermal rotational and vibrational populations can often be assumed because the separation between these energy levels is much smaller than between electronic levels. The populations in excited states are derived from the ground state population in Born-Oppenheimer approximation. For the rotational population, this results in a scaling of the rotational temperature with the ratio of the rotational constants  $B_v$ . The vibrational population in the excited state is redistributed according to a Franck-Condon matrix. For states with different equilibrium distance, this matrix is non-diagonal, and the resulting population is non-thermal.

The rotational temperature of the  $d^3\Pi_u$  state is derived from a Boltzmann plot of the Q1–Q5 lines of the Fulcher transition for  $v' = v'' = 0, 1, 2, 3$ . This temperature is then scaled to the ground state in order to obtain the gas temperature. The vibrational population in  $d^3\Pi_u$  is measured by scaling a single rotational line per vibrational band with a factor that depends on the rotational temperature. It is then compared to a calculated population based on a thermal population in the ground state to obtain the vibrational temperature.

## 3.6 Spectroscopic Measurement of the Atom to Molecule Ratio

The main diagnostic for the density ratio of hydrogen atoms and molecules in the ion source plasma was the comparison of characteristic radiation from each species. The Fulcher band was chosen for the molecule and the Balmer- $\gamma$  line

for the atom. Both transitions are reasonably undisturbed by spectral lines from other transitions. The brighter  $H_\alpha$  and  $H_\beta$  lines would basically be alternatives for the atomic emission. However, the  $H_\gamma$  line is less susceptible to contributions from dissociative excitation and opacity of the Lyman series (see section 3.4). Additionally, the ratio of the effective rate coefficients for the Fulcher band and the  $H_\gamma$  line varies only little with  $T_e$  and  $n_e$ . This means that the intensity ratio of these two transitions yields a good estimate of the atom to molecule ratio even without exact knowledge of the plasma parameters.

The total intensity emitted by the Fulcher transition was calculated from the intensities of the first four diagonal vibrational transitions. These were obtained as described in section 3.5.3. For obtaining the scaling factor  $f_{vib}$  from the measured bands to the whole transition, first a theoretical vibrational population of the  $d^3\Pi_u$  state was calculated. This was done with a vibrationally resolved corona model for a given  $T_e$  and ground state  $T_{vib}$ . Details about this model can be found in [Reg05]. However, some loss processes in the  $d^3\Pi_u$  state (e.g. predissociation) that were originally included in the model were neglected here. This was done for comparability with other works such as [Heg02]. Since no corona model was available for deuterium, the vibrational population of  $d^3\Pi_u$  was estimated with the simpler model described in section 3.5.3.

The matrix of transition probabilities ( $A_{p'p''}^{v'v''}$ ) for the Fulcher transition was taken from [FW06]. It was used to obtain the intensities of all possible vibrational transitions. Their sum was then compared to the sum of the first four diagonal transitions, i.e.  $v' = v'' = 0, 1, 2, 3$  in order to obtain  $f_{vib}$ . This factor varies only little with  $T_e$  and  $T_{vib}$  in the relevant parameter range. At average values of  $T_e = 6$  eV and  $T_{vib} = 5000$  K, the scaling factor is 1.95 for hydrogen and 2.63 for deuterium. It varies only little with  $T_e$  and  $T_{vib}$  within the relevant parameter range.

Multiplying the sum of the measured intensities with  $f_{vib}$  now yields the total radiation from the Fulcher band.

When the total radiation  $\dot{N}_{Fulcher}$  from the Fulcher transition is determined, the molecular density  $n_{H_2}$  can be calculated similar to (3.15):

$$n_{\text{H}_2} = \frac{\dot{N}_{\text{Fulcher}}}{n_e X_{\text{Fulcher}}^{\text{eff}}(T_e, n_e)}. \quad (3.31)$$

$X_{\text{Fulcher}}^{\text{eff}}(T_e, n_e)$  is the effective emission rate coefficient for the Fulcher transition calculated e.g. with a collisional radiative model. The explicit calculation of  $n_{\text{H}_2}$  is not necessary for calculating the atom to molecule ratio. However, equation (3.31) was used to cross-check the absolute intensity calibration of the ANDOR SR303i (see section 3.2.2).

With the intensities and effective emission rate coefficients of both the Fulcher band and the  $\text{H}_\gamma$  line, the atom to molecule ratio  $\Delta_a$  is calculated by dividing (3.15) by (3.31):

$$\frac{n_{\text{H}}}{n_{\text{H}_2}} = \frac{\dot{N}_{\text{H}_\gamma}}{\dot{N}_{\text{Fulcher}}} \cdot \frac{X_{\text{Fulcher}}^{\text{eff}}(T_e, n_e)}{X_{\text{H}_\gamma}^{\text{eff}}(T_e, n_e)}. \quad (3.32)$$

A mean value of  $X_{\text{Fulcher}}^{\text{eff}}/X_{\text{H}_\gamma}^{\text{eff}} = 1.85$  for hydrogen plasmas was assumed for the evaluation of the measurements in this thesis. This corresponds to  $T_e = 6$  eV and  $n_e = 2 \cdot 10^{17} \text{ m}^{-3}$ . A factor of 2 was used as an approximation for the deuterium plasmas because  $T_e$  and  $n_e$  could not be measured (see section 5.1). Also, the collisional radiative model used to calculate the ratio of rate coefficients is not yet adapted to consider isotopic effects in deuterium plasmas.

A weakness of measuring the atom to molecule ratio by the method described above is the extrapolation of the Fulcher band intensity from relatively few measured lines. Any error in the intensity of the critical lines (the Q1 lines for hydrogen and the Q2 lines for deuterium), for example by unresolved interference from other transitions, has a strong influence on the total result. The accuracy of the extrapolation also depends strongly on the accuracy of the rotational temperatures  $T_{\text{rot}}^v(d^3\Pi_u)$  ( $v = 0, 1, 2, 3$ ): they determine the scaling factors  $f_v(T_{\text{rot}})$  from the Q1 respectively Q2 lines to the according vibrational bands. The uncertainty of the  $f_v(T_{\text{rot}})$  factors is one of the main uncertainties for the determination of the total radiation of the Fulcher band. It amounts to approximately  $\pm 6 - \pm 10\%$ . The other uncertainty is the error margin for the intensity calibration, which is in the same order. Therefore, an overall error margin in the order of  $\pm 10 - \pm 15\%$  can be assumed for this diagnostic.

Also, most spectrometers able to satisfactorily resolve the individual lines of the Fulcher band cannot measure the Fulcher band and the  $H_\gamma$  line at the same time. Quite often, only a wavelength range of 6 - 10 nm width can be measured at once so that even the Fulcher band measurements have to be split into multiple separate exposures. Since the typical pulse lengths for the plasmas in positive ions sources are between 1 second and 10 seconds, this usually also means separate plasma discharges and makes good reproducibility of the measurements and plasma conditions crucial for the accurate determination of the atom to molecule ratio.

**To summarise, the main diagnostic for the atom to molecule ratio was to measure the intensity ratio of the  $H_\gamma$  line and the Fulcher transition. The total intensity of the Fulcher band was derived by first extrapolating one rotational line to the whole corresponding vibrational band. The resulting intensities of the vibrational bands  $v' = v'' = 0, 1, 2, 3$  were then further extrapolated to the whole  $d^3\Pi_u \rightarrow a^3\Sigma_g^+$  transition.**

### 3.7 Measurement of the Species Distribution by $H_\alpha$ Doppler Spectroscopy

As already mentioned in section 2.4, three different ion species are extracted from a positive hydrogen ion source:  $H^+$ ,  $H_2^+$  and  $H_3^+$ . All these ions are accelerated to the same energy  $e \cdot U_{ex}$  by the extraction voltage  $U_{ex}$ . The molecular ions have double and triple mass compared to the protons (resp. deuterons), however. This means the velocity of neutral atoms originating from the dissociation of molecular ions in the neutraliser is by a factor  $1/\sqrt{2}$  respectively  $1/\sqrt{3}$  smaller than the velocity of neutrals created by neutralisation of  $H^+$ . When the fast neutral atoms are created by charge exchange of fast ions with slow neutrals, they are electronically excited. Also, collisions of fast neutrals with the neutraliser gas can also lead to excited fast neutrals. The relaxation of the fast excited neutrals leads to the emission of photons, among others  $H_\alpha$  radiation. When measured by a stationary observer, the wavelength  $\lambda$  of the emitted light is Doppler shifted to  $\lambda'$  according to

$$\lambda' = \lambda_0 \frac{1 - \beta \cos \alpha}{\sqrt{1 - \beta^2}}, \quad (3.33)$$

where  $v$  is the relative velocity between particle and observer and  $\beta = \frac{v}{c}$  its ratio to the vacuum speed of light.  $\alpha$  measures the viewing angle towards the particle trajectory. For particles with energies per nucleon of  $eU_{ex}/A = 60$  keV (with  $A$  being the number of nucleons),  $\beta$  is about  $10^{-2}$ , which means that  $\sqrt{1 - \beta^2}$  is still very close to unity for typical extraction voltages  $U_{ex}$  in positive ion sources. The wavelength shift  $\Delta\lambda = \lambda' - \lambda_0$  can therefore be calculated in non-relativistic approximation [FVS98]:

$$\Delta\lambda = -\lambda_0 \cdot \beta \cos \alpha. \quad (3.34)$$

The  $H_\alpha$  Doppler spectroscopy uses the Doppler shift of the  $H_\alpha$  line to distinguish between the full, half and third energy neutrals. Because of their different velocities, they produce three Doppler shifted peaks besides the unshifted line that originates from the background gas. Their measurement yields the beam energy and divergence, and the extracted ion species distribution. It is assumed that the extraction probability is equal for all three positive ion species. The species distribution in the beam therefore mirrors the distribution inside the ion source. Fig. 3.16 schematically shows the geometry of a set-up for  $H_\alpha$  Doppler spectroscopy.

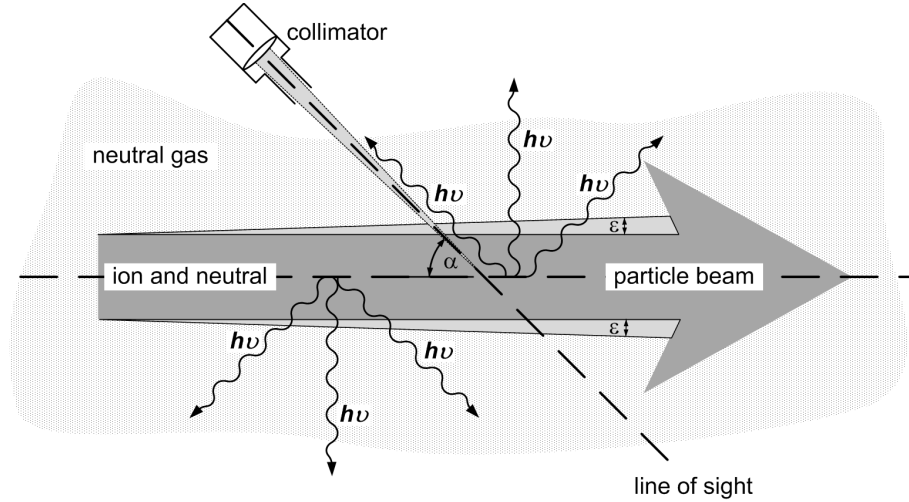


**Figure 3.16:** Geometry of a set-up for  $H_\alpha$  Doppler spectroscopy.  $\alpha$  is the viewing angle,  $\epsilon$  is the half divergence angle of the beam.

A sample spectrum from a hydrogen beam with  $U_{ex} = 42$  kV and a viewing angle of approximately  $47^\circ$  downstream is shown in Fig. 3.17.

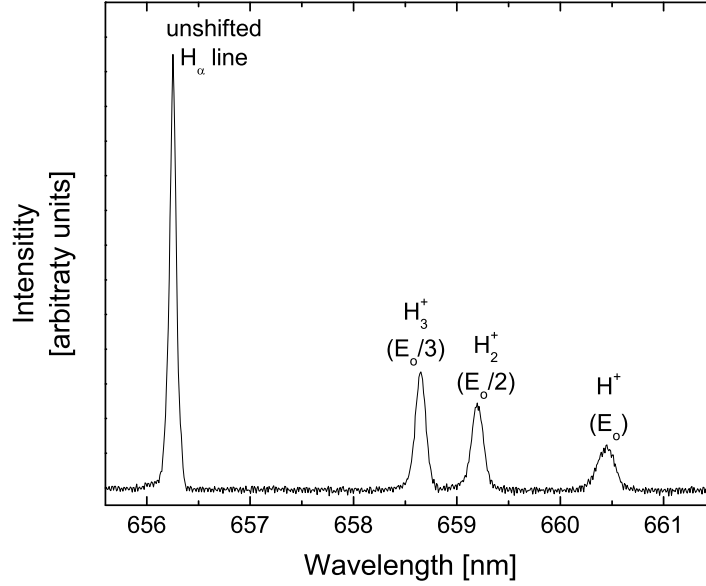


**Figure 3.17:** Sample of a Doppler spectrum. Measured in hydrogen at GLADIS with an extraction voltage of 42 kV. The RF input power was 26 kW, the gas pressure in the ion source was 1.73 Pa.

The ion species distribution extracted from the ion source was derived from the intensity ratio of the three Doppler shifted peaks. For this, it has to be kept in mind that the extracted particle species all interact differently with the neutraliser gas. This makes correction factors  $C_i$  ( $i = E_0/E$ ) necessary that correctly scale the Doppler peak intensities with the relevant ion fractions [Hem85]. First of all, the molecular ions have a higher neutralization probability than the protons or deuterons. Apart from that, molecules can also fragment into neutral particles and ions; these ions, because of their smaller energy, also have a larger neutralization cross section compared to full energy particles. All in all, for calculating the intensities of each peak, a total of 11 particle species (neglecting negative ions) with different energies have to be considered [Hem85]:

- Protons:  $H^+(E_0)$ ,  $H^+(E_0/2)$ ,  $H^+(E_0/3)$
- Neutral atoms:  $H^0(E_0)$ ,  $H^0(E_0/2)$ ,  $H^0(E_0/3)$
- Molecular ions:  $H_2^+(E_0)$ ,  $H_2^+(2E_0/3)$ ,  $H_3^+(E_0)$
- Neutral molecules:  $H_2^0(E_0)$ ,  $H_2^0(2E_0/3)$ .

All these particles originate solely from the three primary ions, namely  $H^+(E_0)$ ,  $H_2^+(E_0)$ ,  $H_3^+(E_0)$ .

Using the cross sections for all the reactions of the fast particles with the back-

ground gas, the correction factors  $C_i$  are calculated with a computer program. Details can be found in [Hem85]. The resulting correction factors are normalised to  $C_1$  [FVS98]. They also depend the target thickness  $\langle nL \rangle$  and full energy per nucleon  $E_0/A$ . They are valid for all isotopes of hydrogen. The values of  $C_2$  and  $C_3$  for an infinitely thick target (i.e.  $\langle nL \rangle \geq 5 \cdot 10^{19} \text{ m}^{-2}$ , see 2.5) are shown in Fig. 3.18.

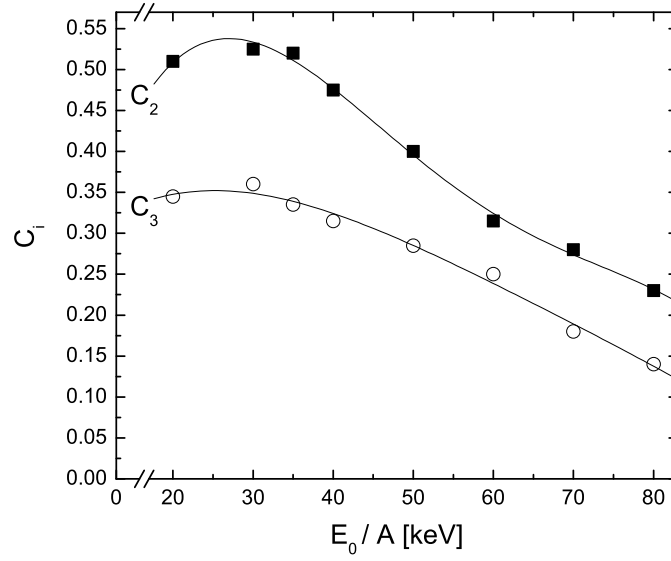


**Figure 3.18:** Correction factors  $C_2$  and  $C_3$  according to [Hem85] versus full energy per nucleon  $E_0/A$  (symbols). The data has been fitted with grade 4 polynomials (drawn through lines) for interpolation to arbitrary energies within the given range.

[Hem85] does not contain error estimations for  $C_2$  and  $C_3$ . Because the calculated data is based on a large number of experimentally measured interaction cross sections, an error margin of at least  $\pm 10\%$  is assumed.

Estimations by [FVS98] show that an infinitely thick neutralisation target can be assumed for the ASDEX Upgrade neutraliser. At the GLADIS test bed, values for  $\langle nL \rangle$  in the range from approximately  $6 \cdot 10^{19} \text{ m}^{-2}$  to  $1.6 \cdot 10^{20} \text{ m}^{-2}$  have been derived from pressure measurements in the target tank (see also section 5.2.3).

The beam divergence can be derived from the width of the Doppler shifted peaks.

Assuming a small<sup>6</sup> divergence angle  $\epsilon$ , the deviation in viewing angle causes a broadening  $\delta$  of the shifted peaks that is proportional to  $\epsilon$  (see also Fig. 3.16):

$$\delta \propto \cos(\alpha - \epsilon) - \cos(\alpha + \epsilon) \approx 2\epsilon \cdot \sin \alpha. \quad (3.35)$$

A similar effect is caused by the tilting of the grid halves of the extraction system of a positive ion source as described in section 2.4: Doppler spectra show two overlapping peaks for each energy, each peak corresponding to one half of the beam [FKV<sup>+</sup>99]. A sample spectrum can be seen in Fig. 5.4.

The beam divergence was not measured here because it mainly depends on the beam optics, i.e. the perveance matching (see section 2.4). Systematic analysis of the dependence of the divergence on plasma parameters such as the gas temperature could be the subject of future investigations.

**To summarise,  $H_\alpha$  Doppler spectroscopy of the extracted beam was used to derive the ion species distribution. For this, the intensity ratios of the three Doppler shifted peaks of the  $H_\alpha$  line that correspond to the neutralisation of  $H^+$ ,  $H_2^+$  and  $H_3^+$  ions was measured. The intensities were scaled by correction factors  $C_i$  that consider the different interaction cross sections of the ion species with the neutraliser gas.**

---

<sup>6</sup>i.e.  $\sin \epsilon \approx \epsilon$  and  $\cos \epsilon \approx 1$ , for  $\epsilon \ll 1$



## 4 Preparation Work at JET

### 4.1 The JET Neutral Beam Test Bed

A part of the measurements was planned to be performed at the Neutral Beam Test Bed (NBTB) of the JET fusion experiment in Culham, UK. This test bed is a full scale replica of the NBI system at the main experiment. It is located in a separate shielded chamber ( "*Hot Cell*" ) and can operate independently from JET, although some of the main systems (e.g. cooling circuits, cryogenics) are shared at a basic level. The NBTB is equipped with a multitude of diagnostics for commissioning PINI injectors: electrical diagnostics like beam current and extraction voltage monitoring, water and infrared beam calorimetry and a multichannel Doppler spectroscopy system [DAF<sup>+</sup>87, CFG98]. While JET has 8 arc-driven PINI sources (see section 2.6.1) attached to each of its two Neutral Injection Boxes (NIB), only one PINI at a time is attached to the NBTB. The NBTB has a target tank with a mock up of the box scraper, a water-cooled beam dump and several diagnostic calorimeters that can be moved into the path of the beam. A PINI is always fully mounted together with its neutraliser [DAF<sup>+</sup>87]. A sketch of the NBTB along with the Doppler spectroscopy lines of sight can be seen in Fig. 4.1.

In order to take absolute spectroscopic measurements of the source and neutraliser plasmas of a JET PINI, it was necessary to re-commission and recalibrate the existing spectrometer. This meant a thorough testing of the system as well as some maintenance work that will be described in the following sections.

During a longer shut-down of the main experiment at JET, vital systems for the operation of the NBTB were also out of order. Because of this, the planned measurements could not be performed (see section 4.6).

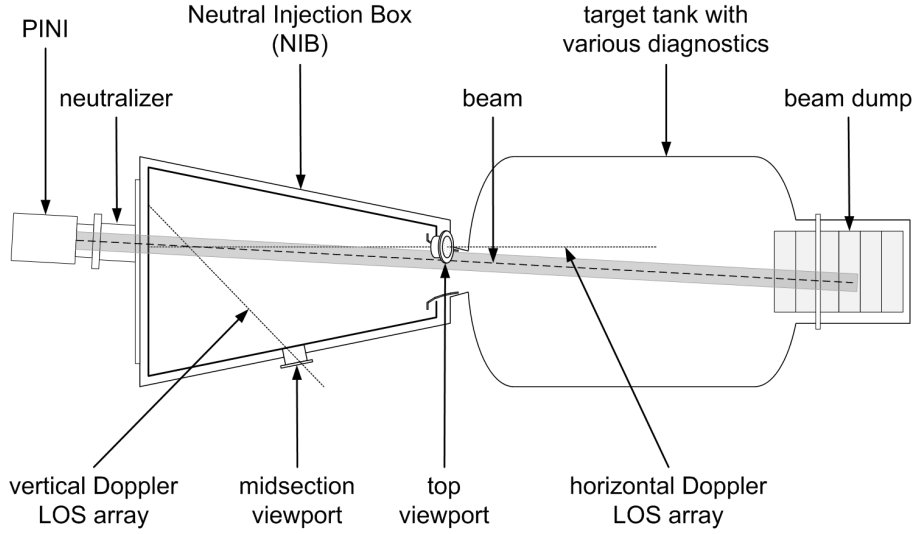


**Figure 4.1:** Sketch of the JET NBTB along with the Doppler spectroscopy lines of sight (LOS).

## 4.2 Testing of the Spectroscopic Equipment

The spectroscopic equipment at the NBTB (see section 3.1) was tested on a more basic level than that at the other experiments. This was necessary because it had not been regularly used for a longer time. It was not only recalibrated, but also tested for detector linearity and uniformity. The spectrometer entry optics was also redesigned for a better sensitivity of the system. Furthermore, the integration sphere that serves as a spectral radiance standard at the NBTB was refitted with a stronger light source and recalibrated (see section 4.3.1).

The detector's linearity in respect to exposure time was tested using the integration sphere before its recalibration. The spectrometer was set to a fixed wavelength of 653 nm. This test was performed with a single fibre of the original entry optics assembly and a slit width of  $70\mu\text{m}$ . Several exposures with exposure times from 100 ms to 5000 ms were taken. The dark current was subtracted and the light signal integrated over the whole wavelength range for this spectrometer position. As can be seen in Fig. 4.2, a good linearity is confirmed for exposure times between 100 ms and 5000 ms. A still better fitting result can be obtained by allowing a constant offset to the linear fit. Exposure times shorter than 100 ms are not recommended.

For the absolute intensity calibration (see section 3.2.2) the exposure time had to be increased to 10000 ms. Linearity testing up to this value was not possible

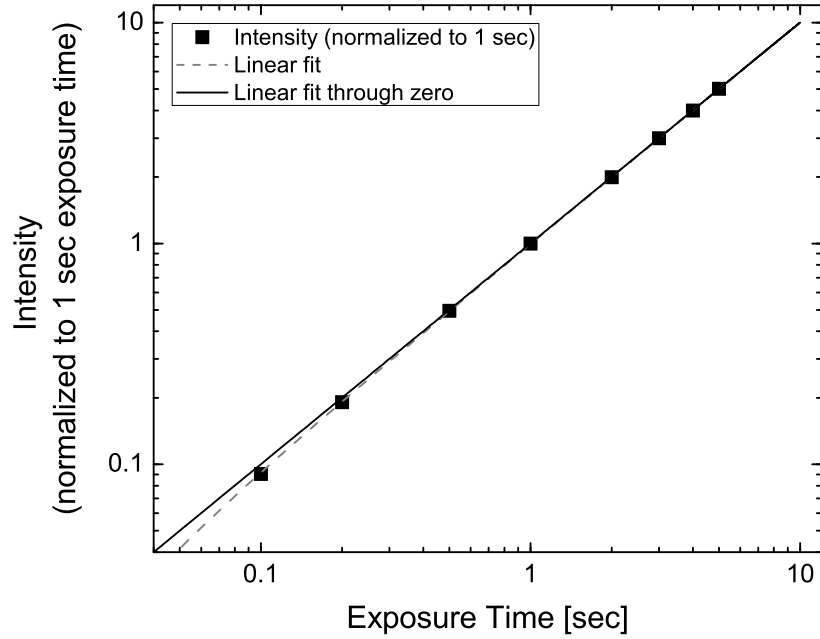


**Figure 4.2:** Linearity testing of the JET NBTB spectrometer.

within the available time and is yet to be done.

Fig. 4.3 shows several background corrected spectra recorded for this test. It can be seen that several pixels at the left and right side of the CCD are not illuminated. This could be caused by light being cut off by the exit mirror. These pixels can be used for dark current subtraction. It can also be seen that the noise level becomes higher with increasing signal strength respectively exposure time. The relative standard deviation of the continuum signal is 3.5% or less for exposure times of 500 ms or more and saturates at around 1.7% for long exposure times. The noise level is therefore considered tolerable. For the small signals at shorter exposure times, the signal to noise ratio becomes worse (up to 16% relative standard deviation at 100 ms).

Looking at several spectra taken with the original system, a relatively low sensitivity of the system (in relation to comparable systems) becomes obvious. Even the unshifted  $H_{\alpha}$  line by far does not utilise the dynamic range of the camera (16 bit per pixel), even at exposure times of one second and more. Therefore, all fibre optics assemblies, especially the spectrometer entry optics, were surveyed for light losses. It turned out that the lens assembly that was used to make a demagnifying projection of 24 lines of sight on the CCD array caused considerable

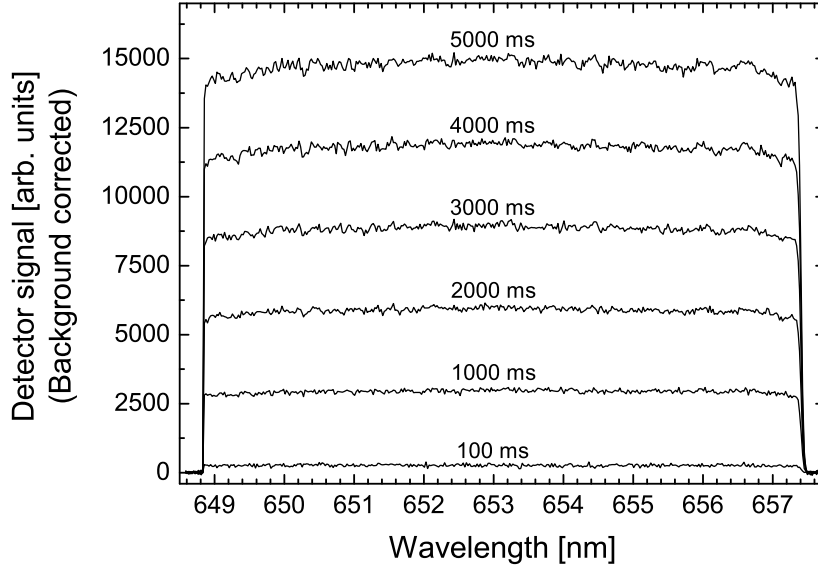


**Figure 4.3:** Background corrected spectra of test measurements of a continuum light source with the JET NBTB spectrometer.

losses at the entrance slit. To increase the sensitivity for more reliable absolute measurements, a new entry optics assembly was designed (see 4.3.2).

## 4.3 Maintenance and Refurbishment Work

### 4.3.1 Spectral Radiance Standard

In order to increase the light output of the NBTB spectral radiance standard, its original 10 W tungsten halogen light bulb was replaced with a 30 W bulb. For this, the lamp socket also had to be exchanged. After that, its light output was calibrated in spectral radiance units. The calibration from 380 nm to 800 nm was carried out by Bentham Instruments (date: July 18<sup>th</sup>, 2007). The calibration certificates were handed over to the JET Beam Development Group who operates the NBTB.

### 4.3.2 Spectrometer Entry Optics

In a first step to increase the spectroscopic system's sensitivity, the spectrometer entry optics assembly was redesigned in order to minimize the light losses caused by the demagnifying lens assembly. The number of fibres was reduced from 24 to 12. The camera objective was removed and the fibre ends were placed directly in front of the entrance slit. The whole set-up is sketched in Fig. 4.4.

Since the original 24 fibre assembly had also proven very fragile due to stress on the fibres and lack of cover, the new design was also made more robust. For this, the stripped fibre ends were enclosed in an aluminium block. A face plate for the slit housing that fits tightly around the fibre clamp was added to aid the alignment and to further eliminate stray light<sup>1</sup>. Construction drawings of the new fibre holder assembly can be found in Figs. A.5, A.6 and A.7 in the appendix.

For accurate positioning of the fibre clamp, it was mounted to a manual three-way stage that was already used for aligning the previous assembly. The y-position of the three-way stage was nearly fixed by the faceplate; the z position was slightly adjusted until all 12 fibres were fully visible on the CCD; the x position was adjusted until an image with the maximum intensity per fibre with a still reasonable separation of the fibre images was achieved.

### 4.3.3 CCD Camera

When checking the alignment of the new entry optics with a Neon lamp illuminating all 12 fibres, and a spectral line centred on the CCD, a small but noticeable tilt of the image on the CCD became apparent. Since moving and tilting the fibre assembly did not correct this, the camera was rotated carefully on its flange until all 12 images formed a perfect column. This as well as fitting a new entry optics assembly made a recalibration of the wavelength axis necessary (see section 3.2.1). The 12 channels defined by the new entry optics assembly are covered by the binning areas listed in Tab. 4.1. It can be seen in the table that the margin at the bottom is larger than at the top. The reason for this is that for the bottom end, the light path appeared to be cut off for positions farther down. This could be caused by the exit mirror, just like the dark pixels at the left and right sides of the CCD (see section 4.2).

---

<sup>1</sup>Ambient light suppression was already quite good due to a blackened box enclosing the spectrometer and fibre assemblies.

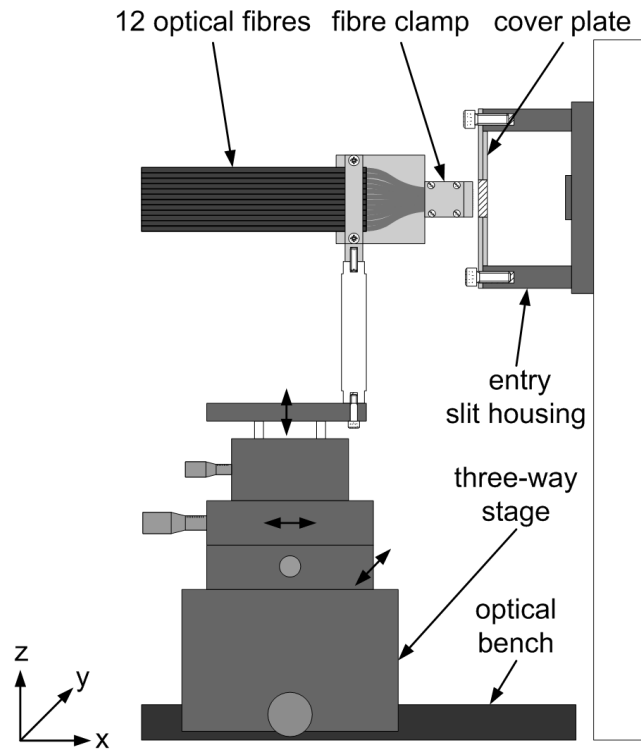


**Figure 4.4:** Fibre Holder Assembly for the JET NBTB spectrometer. The three-way stage can be moved on the optical bench for coarse adjustment of the x position.

**Table 4.1:** CCD Binning Areas of the JET NBTB spectrometer. The total chip area is  $410 \times 600$  pixels.

Channel	From CCD row	To CCD row
1	5	47
2	52	94
3	98	140
4	145	157
5	192	234
6	240	282
7	288	330
8	335	377
9	382	424
10	429	471
11	475	517
12	523	565

## 4.4 Spectrometer Calibration

A wavelength calibration as well as an absolute spectral radiance calibration of the spectroscopic system was performed. Details can be found in section 3.2.

## 4.5 Data File Conversion Program

Since the spectrometer's data acquisition software produces binary files, a program converting these to ASCII files was written. The program is able to simply convert the binary data into CCD raw data (counts versus pixel) as well to perform a wavelength calibration and binning of selected CCD rows into a single dataset (software binning). It produces a preview image with reduced resolution showing the binning tracks which can also be edited by the user. The default binning tracks are those defined in the initialization file of the program used for evaluation of Doppler spectra by the BDG. It also has a batch mode (without preview) to quickly convert larger numbers of files.

## 4.6 Measurements

During the stay at the JET facility, the main experiment went into a prolonged maintenance shut-down. Because of this, several systems necessary for NBTB operation that are shared with the main experiment, especially high voltage, cooling water and cryogenics, were unavailable. When the end of these outages was postponed, the Beam Development Group decided to vent the test bed vacuum for maintenance work of their own. While the maintenance and calibration work on the spectrometer described in this chapter could still be carried out, pulse operation for the test bed was postponed several more times to a date too close to the submission deadline for this work. Therefore, only the measurements at the RF sources at ASDEX Upgrade and GLADIS could be performed (see chapter 5). The data to be gained from measurements at the NBTB remains of interest because it will provide a comparison between the RF driven sources and high-powered arc-driven sources. Arc sources are also used at ASDEX Upgrade, but the source plasma of these sources is not accessible for spectroscopy.





## 5 Experiments at IPP Garching

Measurements were carried out at two experiments at the Max-Planck-Institute for Plasma Physics (IPP) in Garching, Germany: the north-west neutral beam injector at the fusion experiment ASDEX Upgrade and the high heat flux test bed GLADIS for materials testing. The ion sources used at these experiments were already described in sections 2.6.2 and 2.6.3. The evaluation methods are described in sections 3.4, 3.5.3, 3.6 and 3.7. In this chapter, a detailed description of the performed measurements along with the lines of sight for the spectroscopy of the beam and the ion source plasma is given. The results of the measurements for each ion source are discussed and compared.

### 5.1 The Neutral Beam Injection at ASDEX Upgrade

Besides ohmic and electromagnetic wave heating, the main plasma of the fusion experiment ASDEX Upgrade is heated by two neutral beam injector beam lines with four PINI type ion sources each. The “South-East” beamline contains four 60 kV arc-driven PINIs, the “North-West” beam line contains four 93 kV RF PINIs<sup>1</sup> [IPP08]. Both beam lines can be operated in deuterium as well as in hydrogen, although for most ASDEX Upgrade discharges only deuterium is used. Each beam line is able to inject a heating power of up to 10 MW of D<sup>0</sup> atoms into the torus [FKV<sup>+</sup>99]. The investigated ion source is the RF source number 4 of the North-West injector (“NW4”). It is marked in Fig. 5.1. The vacuum in the injector box is maintained primarily by four titanium evaporator pumps with a pumping speed of  $6 \cdot 10^5$  l/s (for H<sub>2</sub>). A conventional vacuum system with two turbomolecular pumps (pumping speed: 2200 l/s each) is also present [IPP08].

---

<sup>1</sup>Maximum acceleration voltages stated for deuterium. For hydrogen, voltages are lower: 55 kV for beam line 1, 72 kV for beam line 2. The maximum voltage in hydrogen is determined by the maximum current the high voltage supply can deliver.

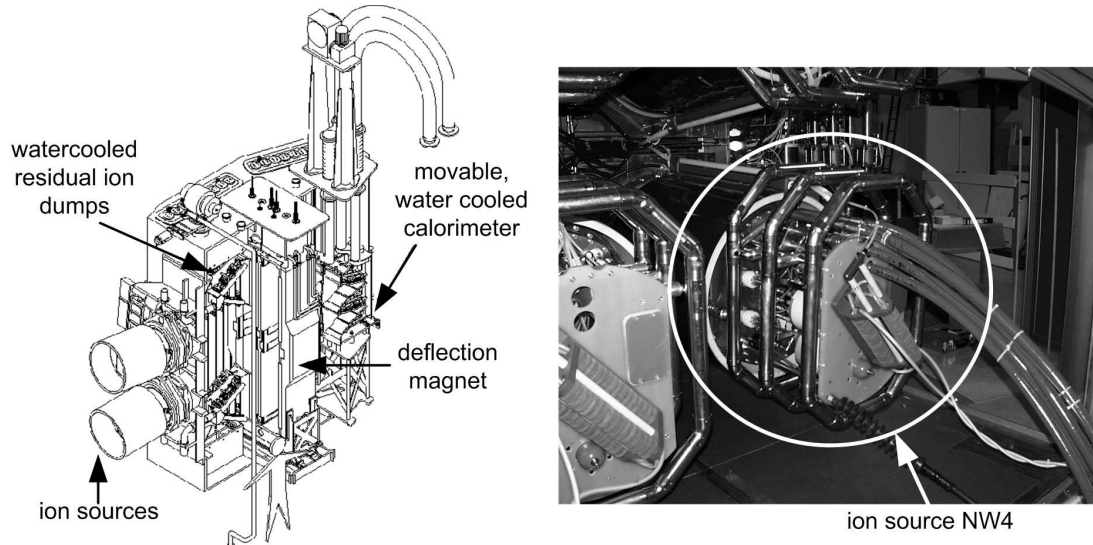


**Figure 5.1:** The North-West injector of the NBI system at ASDEX Upgrade. One half of the injector is sketched in the schematic on the left. Source NW4 is the bottom right source. It is marked in the photograph on the right [IPP08].

The NBI system at ASDEX Upgrade can be operated either synchronous with the fusion experiment for plasma heating, or in an asynchronous test mode. In asynchronous mode, a shutter valve between the neutral injector box and the torus is closed, and the beams are fired onto a retractable calorimeter.

### 5.1.1 Lines of Sight

As already mentioned in section 3.1, spectroscopic access to the RF PINI was provided via the optics of the interlock for the RF generator (see section 3.1). It provided a line of sight near the edge of the source plasma. As a consequence, the line of sight is situated within the heating zone of the RF (see section 2.3). This is sketched in Fig. 5.2.

The line of sight for the beam spectroscopy was located in the neutraliser of the ion source NW4. Its intersection with the beam was approximately halfway along the neutraliser with a viewing angle of  $\alpha = 50^\circ$  [FVS98]. The geometry is sketched in Fig. 5.3.

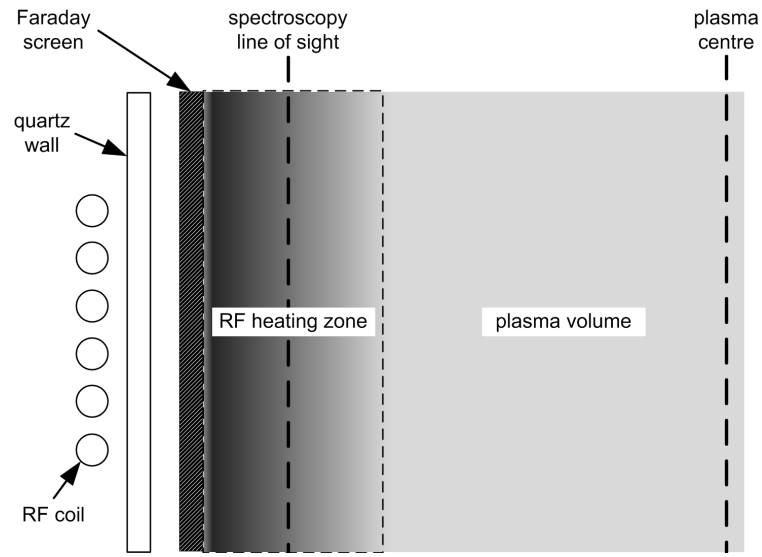


**Figure 5.2:** Sketch of the location of the spectroscopy line of sight within the source plasma of the RF PINI. Because of the skin effect, the RF can only heat the plasma near the edge.

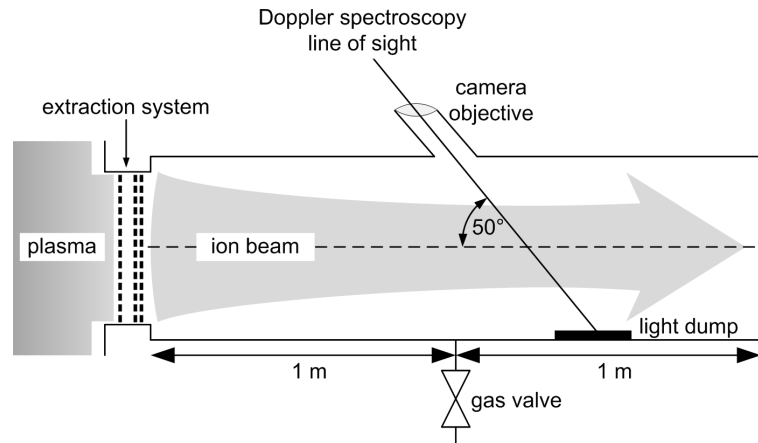


**Figure 5.3:** Location of the Doppler spectroscopy line of sight in the neutraliser of source NW4.

### 5.1.2 Measurements

Measurements in deuterium operation were performed for five different RF power settings<sup>2</sup>: 57 kW, 64 kW, 73 kW, 75 kW and 87 kW. The pulses with 57 kW, 64 kW and 73 kW were performed in asynchronous mode, the pulses with 75 kW and 87 kW were performed synchronous with ASDEX Upgrade since the available beam time was limited and ASDEX Upgrade operation was priority. A number of measurements without extracting a beam could be taken with  $P_{RF} = 75$  kW

<sup>2</sup>These are the set values of the RF generator.

for comparison.

For all these measurements, the gas flow into the source and the neutraliser, and accordingly the gas pressure, was not changed. Absolute values for the gas pressure could not be obtained, however. Typical values are assumed to be in the range of 2.5 Pa [DAF<sup>+</sup>87].

For comparison with the measurements at the GLADIS test bed and to study isotope effects, pulses in hydrogen operation were also recorded. For this, the RF power was set to 85 kW. The gas flow settings were the same as for the deuterium pulses. Accordingly, the pressure is also at the same value of 2.5 Pa.

The tilting of the sub-grids of the PINI's extraction system (see section 2.4) leads to twinned Doppler peaks. A sample spectrum can be seen in Fig. 5.4.

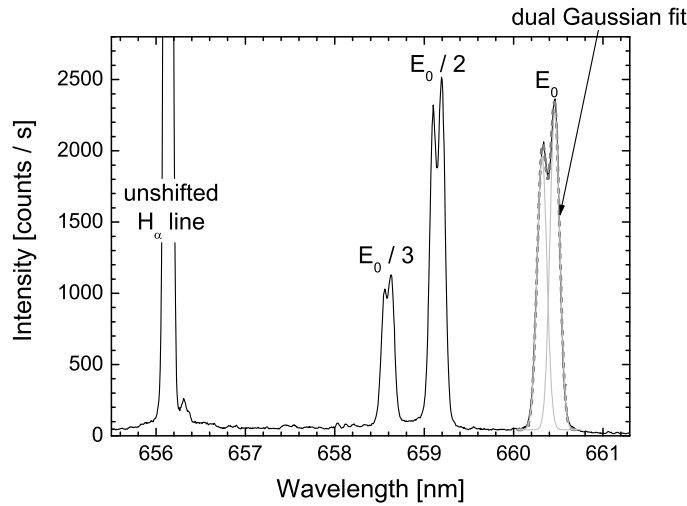


**Figure 5.4:** Doppler peaks measured at the beam of the ASDEX Upgrade neutral beam injector NW4 with Gaussian fits. Peaks are twinned due to vertical inclination of the grid halves.

The distance between the sub-peaks corresponds to the tilting angle of  $\pm 0.9^\circ$ . The difference in height is due to a geometric effect: the effective viewing length through the sub-beams is determined by the angle relative to the line of sight. This is sketched in Fig. 5.5.

The twinned peaks made a fit with two overlapping Gaussian peaks (see Fig. 5.4) necessary. To check the validity of the fit, the ion species distribution was also derived from peak areas measured by integrating over the twinned peaks. The results were nearly identical.

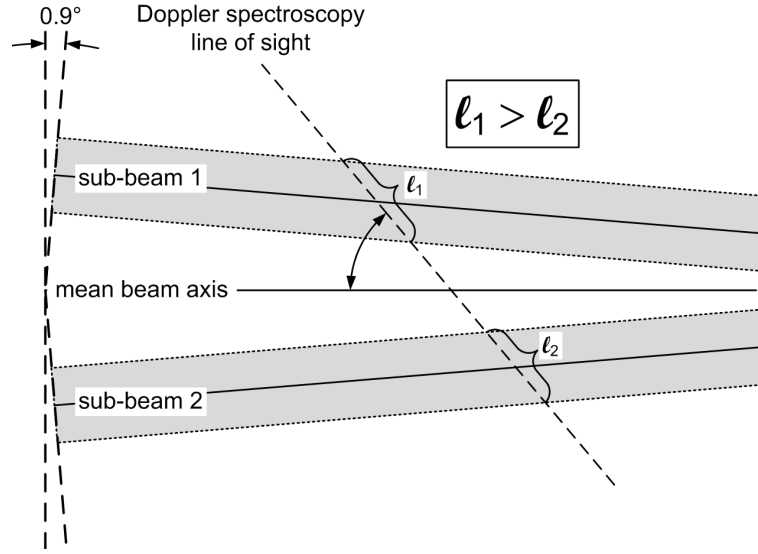


**Figure 5.5:** Effective viewing lengths through the sub-beams of an ASDEX Upgrade neutral injector. The tilt of  $\pm 0.9^\circ$  is exaggerated in the sketch.

### 5.1.3 Results

#### Ion species distribution and atom to molecule ratio.

With increasing RF input power  $P_{RF}$ , the  $D^+$  fraction in deuterium rises from 61.2% at 57 kW to 70.4% at 87 kW. At the same time, the  $D_3^+$  fraction drops significantly from 13.8% to 6.5% while the  $D_2^+$  fraction changes only little, dropping from 25.0% to 23.0%. All three species distributions follow very smooth tendencies in the observed parameter range. The tendencies as well as the absolute values are well in agreement with the measurements presented in [FKV<sup>+</sup>99]. For hydrogen at an RF power of 85 kW, the  $H^+$  fraction of 54.9% is lower than the comparable  $D^+$  fraction at 87 kW. Accordingly, the molecular ion fractions are higher: 28.6% for  $H_2^+$  and 16.5% for  $H_3^+$ .

The reproducibility of the species distribution measurements was tested for the 93 kV / 87 kW and for the 82 kV / 75.2 kW settings. The deviations in the species distribution results are only minimal (93 kV: standard deviations of less than 0.2% for each species, with the  $D^+$  fraction being the most accurate one since it produced the highest intensity).

The spectroscopic measurements of the source plasma show that the atom to molecule ratio in deuterium rises with  $P_{RF}$  from 0.144 at 57 kW to 0.209 at 87 kW. Together with the observations for the species distribution, this confirms the assumption that at a constant gas flow, the fraction of atomic ions (here:

$D^+$ ) increases with the fraction of neutral atoms in the ion source, with the molecular ion fractions decreasing accordingly. The comparison of measurements with and without extraction at  $P_{RF} = 75$  kW results in nearly identical atom to molecule ratios.

In hydrogen, the atom to molecule ratio at an RF power of 85 kW is reduced to 0.112. This is only slightly more than half the value at 87 kW in deuterium.

The results for the species distribution and atom to molecule ratio measurements are plotted in Fig. 5.6.

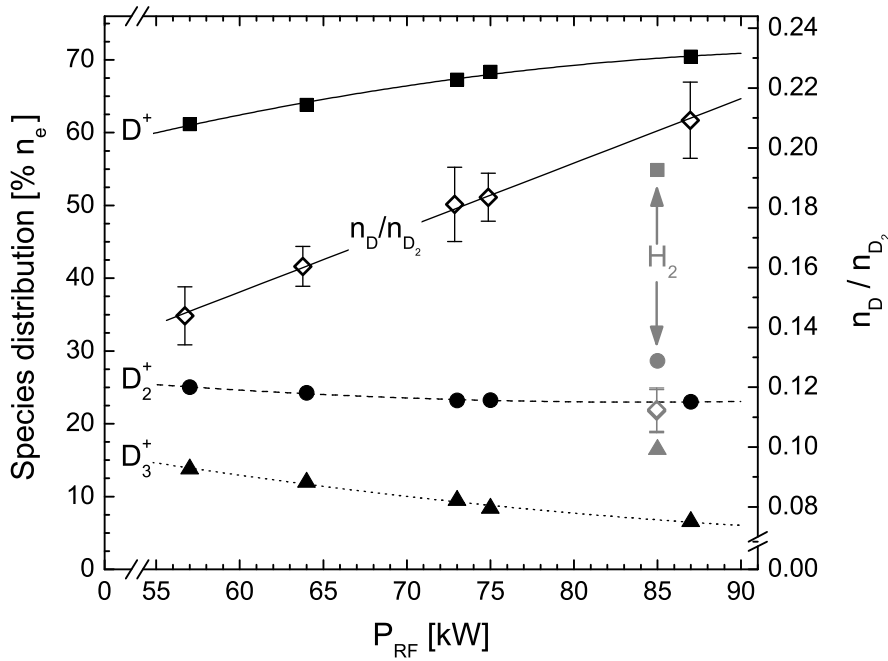


**Figure 5.6:** Species distribution and atom to molecule ratio versus RF input power measured at the ASDEX Upgrade neutral injector NW4. The measurements in hydrogen are marked grey.

The electron density and temperature could not be measured spectroscopically due to the lack of available measurement time and an absolute calibration. However, it is assumed that  $n_e$  rises with  $P_{RF}$  while  $T_e$  stays constant on the basis of [FKV<sup>+</sup>99]. This leads to the conclusion that at constant pressure, the dissociation of molecular deuterium increases with the RF power due to a higher electron density. The higher neutral atom density in turn leads to a higher  $D^+$  fraction.

The differences between the isotopes hydrogen and deuterium can also be explained by a difference in electron density. Because the deuterium ions are heavier

than hydrogen ions, they are also slower. Since the loss of charge carriers from a steady state plasma is ambipolar and therefore governed by the slower species, this also reduces the loss rate of electrons and leads to a better confinement of the plasma. Therefore, the electron density is higher in deuterium plasmas compared to hydrogen plasmas at equal RF input power. Accordingly, the atom to molecule ratio and subsequently the atomic ion fraction are also higher in deuterium.

### Gas temperature and vibrational population.

The gas temperature inside the ion source is around  $T_{gas} = 1150$  K in deuterium. The results for all  $P_{RF}$  settings are shown in Fig. 5.7. Considering the error bars,  $T_{gas}$  shows only little dependence on  $P_{RF}$ . However, the results can also be interpreted as a minor decrease of  $T_{gas}$  with  $P_{RF}$ . In hydrogen, the gas temperature is higher:  $1230 \pm 130$  K at  $P_{RF} = 85$  kW.

Comparing measurements with and without extraction at  $P_{RF} = 75$  kW, the gas temperature appears to be higher at  $1240 \pm 50$  K without extraction.

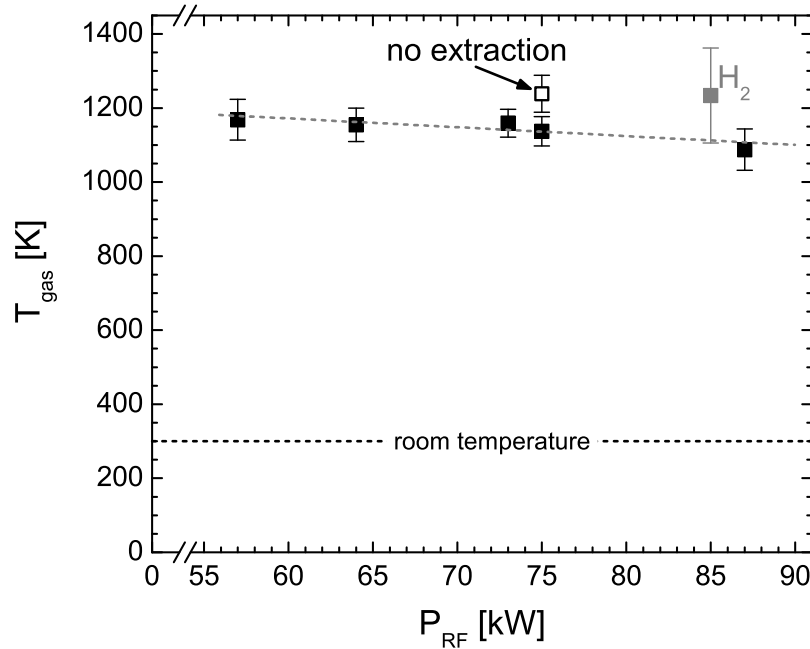


**Figure 5.7:** Gas temperature in deuterium at ASDEX Upgrade. The value measured in hydrogen is marked grey.

A possible explanation the observed behaviour of  $T_{gas}$  is a difference in diffusion:

a higher diffusion of neutral particles means that the influence of the water cooled walls on the gas temperature becomes stronger [Heg02]. In hydrogen as well as at lower RF powers in deuterium, the atom to molecule ratio is lower than at high  $P_{RF}$  in deuterium. Because atoms are smaller than molecules, they also have a higher diffusion coefficient. As a consequence, a higher atom to molecule ratio also means a higher overall diffusion, and accordingly a lower gas temperature. Comparing the gas temperature for the different hydrogen isotopes, there is a second effect which is due to the higher mass of deuterium: the energy transfer between the electrons, which are the particle species that is heated by the RF, and the neutrals is less efficient compared to hydrogen. This also leads to a lower  $T_{gas}$ .

Because the atom to molecule ratio was equal with and without extraction at  $P_{RF} = 75$  kW, the difference in gas temperature here has to be explained by the disturbance of the plasma by the extraction. Further systematic measurements would be necessary to make a more precise statement.

The measured vibrational population of the  $d^3\Pi_u$  state was compared to theoretical populations derived from thermal populations in the molecule's ground state. The measured populations of the vibrational states  $v'$  correspond to vibrational temperatures  $T_{vib}(X^1\Sigma_g^+)$  between 3500 K and 5000 K. The values are listed in Tab. 5.1. In hydrogen at  $P_{RF} = 85$  kW, the measured vibrational population does not agree well with any one of the modelled ones. The vibrational temperature is estimated to be in the range of 6000 K or higher. This higher value than in deuterium can be explained by considering that in deuterium, the vibrational energy levels are closer together due to the higher mass. This means that a similar population distribution is described by a lower temperature in deuterium. The ground state vibrational temperature is significantly higher than the gas temperature because not only heavy particle collisions contribute to the vibrational population, but also the electrons. Their temperature is significantly higher than the gas temperature.

The variation of  $T_{vib}$  with  $P_{RF}$  does not seem as systematic as for the gas temperature. It is assumed that the observed variations are more likely due to measurement uncertainties of the vibrational population for a  $T_{vib}$  around 4000 K. A more detailed discussion of vibrational populations in hydrogen can be found in section 5.2.3.



**Table 5.1:** Vibrational temperatures of deuterium measured at ASDEX Upgrade.

$P_{RF}$ [kW]	$T_{vib}$ [K]
57	5000
64	4000
73	4000
75	3500
75 (no extraction)	4500
87	5000
85 (H <sub>2</sub> )	$\geq 6000$

Examples of the calculated and measured vibrational population for both isotopes are shown in Fig. 5.8. The error margins are derived from the uncertainty of the  $f_v(T_{rot})$  factors, as described in section 3.5.3. The data point for  $v' = 0$  does not have error bars because  $n(v')$  is normalized to  $n(v' = 0)$ , and the margins for  $v' > 0$  are increased accordingly by the uncertainty of  $n(v' = 0)$ .

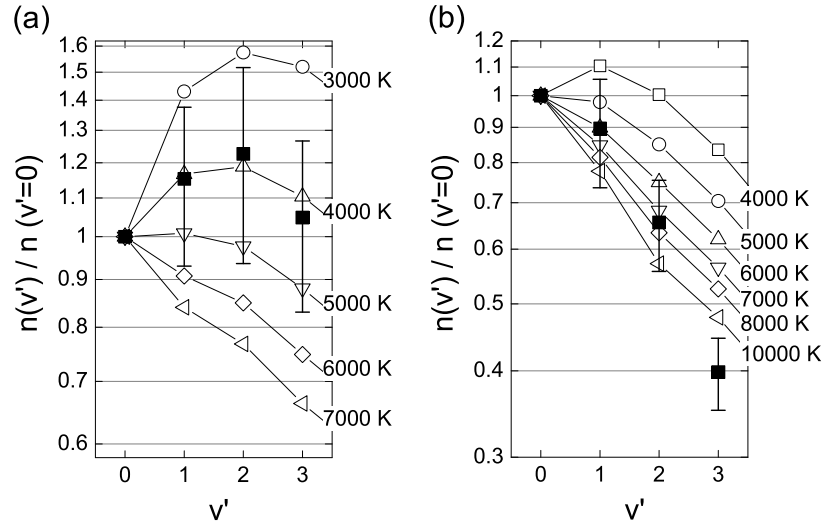


**Figure 5.8:** Vibrational populations measured at ASDEX Upgrade (filled symbols) and comparison with model calculations (open symbols). (a) shows the population of the  $d^3\Pi_u$  state of deuterium at  $P_{RF} = 73$  kW, (b) shows the population for hydrogen at  $P_{RF} = 85$  kW.

## 5.2 The GLADIS High Heat Flux Test Bed

The GLADIS test bed (see Fig. 5.9) is a facility where plasma facing components for fusion experiments can be subjected to heat loads and the resulting thermal stresses similar to operational conditions. Typical power densities are between 10 and 20 MW/m<sup>2</sup>. The system is currently able to deliver a peak power density between 3 and 55 MW/m<sup>2</sup> in the beam centre [GBBM07]. The tested components are mainly for the upcoming experiments WENDELSTEIN 7-X (stellarator) and ITER (tokamak). It is designed to be able to handle large samples (even full scale ITER divertor elements; maximum sample length 2 m, heated length up to 30 cm) and perform a large number of thermal cycles ( $\geq 100$  per hour) on them. It is equipped with a multitude of sample diagnostics like cooling water calorimetry, thermocouples and visual as well as infrared imaging cameras [GBB<sup>+</sup>05]. One line of sight for Doppler spectroscopy of the beam and one for spectroscopic diagnostics of the source plasma have also been provided. While the source plasma diagnostic was a temporary set-up for these measurements, the Doppler spectroscopy is planned to be commissioned as a routine diagnostic for the ion beam composition [GBBM07].

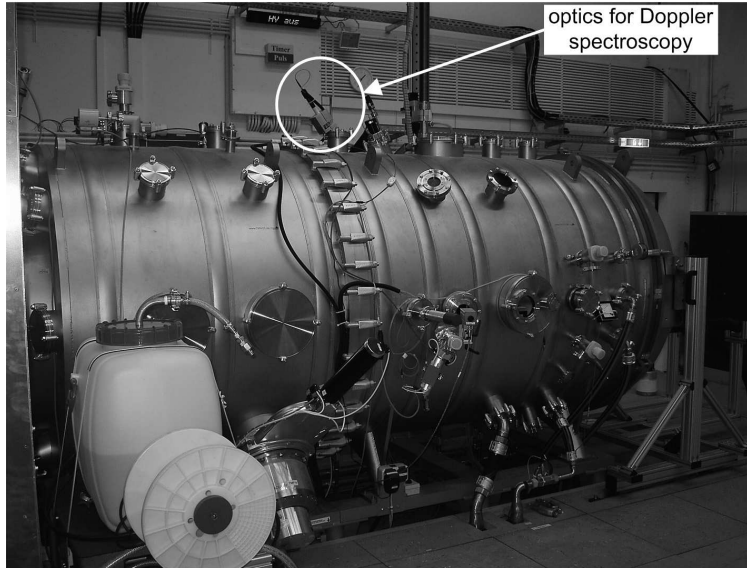


**Figure 5.9:** Photograph of the GLADIS test chamber. The Doppler spectroscopy lens is marked on top of the chamber.

The GLADIS test bed consists of two positive hydrogen ion sources (only one is currently operated) with a maximum beam power rating of 1.2 MW each, and a test chamber containing beam scrapers, the sample holder with cooling water

supply for the samples and a water-cooled beam dump. The test chamber also contains a multitude of diagnostic ports. It has a sliding end door with the full diameter of the tank (the beam dump is mounted to this door) [GBB<sup>+</sup>05].

The vacuum is maintained by four turbomolecular pumps in combination with a 1000 m<sup>3</sup>/h Roots pump (total pumping speed: 6000 l/s) per beam line. Only beam line 1 (upper ion source) is currently operated [GBB<sup>+</sup>05]. The vacuum pressure is in the order of  $10^{-6}$  mbar in standby mode and rises to  $\approx 2 \cdot 10^{-3}$  mbar during beam pulses (see section 5.2.3). This background gas pressure during pulses is comparable to the gas pressure in the ASDEX Upgrade NBI neutralisers [FVS98] and therefore effectively serves as a neutraliser. Because no ion deflection magnets are present, the sample targets are struck by a mixed neutral/ion beam [GBB<sup>+</sup>05].

### 5.2.1 Lines of Sight

The line of sight for the source plasma spectroscopy was provided by the optics for the RF generator interlock (see section 3.1). Similar to the set-up at ASDEX Upgrade, the line of sight was located at the edge of the ion source and within the RF heating zone (see Fig. 5.2). Fig. 5.10 is a photograph of the back plate and the Faraday screen of the GLADIS ion source. The pinhole for the spectroscopy line of sight, the gas inlet and the starter filament can also be seen.

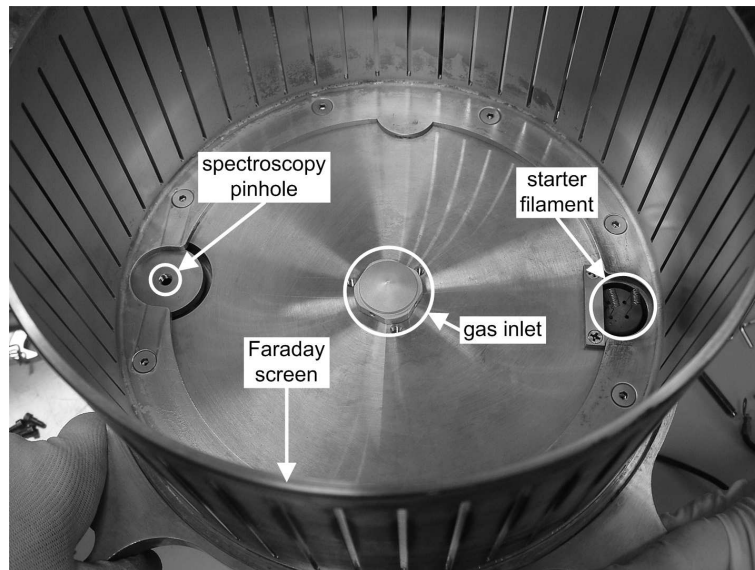


**Figure 5.10:** View of the back plate of the GLADIS ion source with the Faraday screen. The spectroscopy pinhole, the gas inlet and the starter filament are also marked

The line of sight for the Doppler spectroscopy of the beam intersects with the beam approximately in the target plane of the test chamber. The intersection point is approximately 3 m away from the extraction system, the viewing angle is approximately  $47^\circ$ . The geometry can be seen in Fig. 5.11.

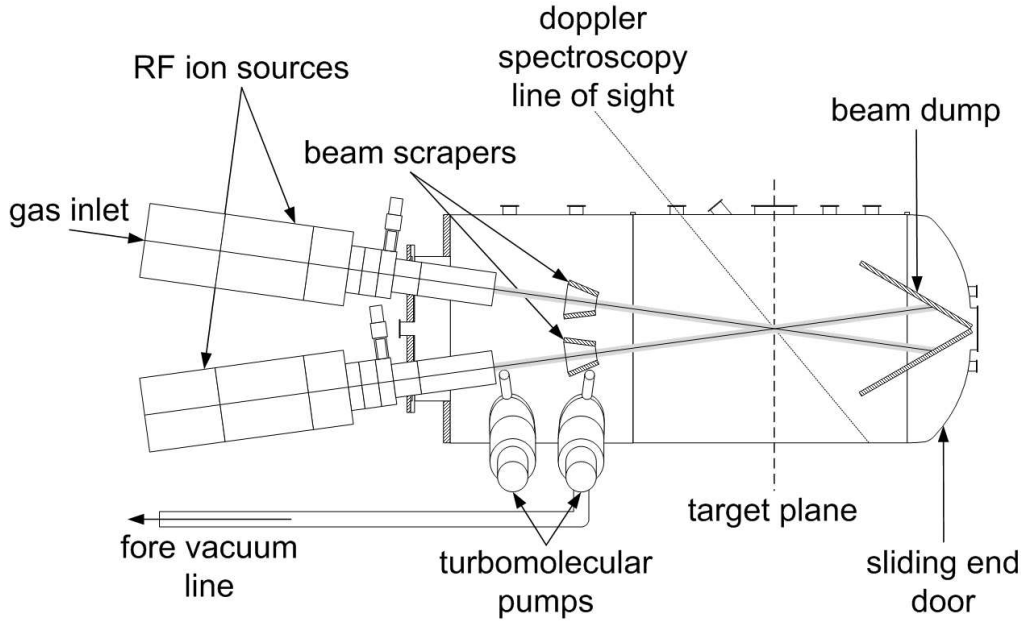


**Figure 5.11:** The GLADIS high heat flux test bed. The overall tank length (without ion sources) is  $\approx 3.7$  m. Only the upper one of the two ion sources is currently in use.

### 5.2.2 Measurements

At the GLADIS test bed, pressure measurements in the target tank and in the ion source were made in order to determine the neutral gas density depending on the gas valve position. These values are necessary for several points:

- Determining the variation of the spectroscopically measured parameters (ion species distribution,  $\Delta_a$ ,  $n_e$ ,  $T_e$ ) with the gas pressure.
- Obtaining absolute particle densities for the interpretation of absolute intensity measurements.
- Relating the RF input power and pressure settings of the ion source to other types of ion sources.
- Determining the target thickness  $\langle nL \rangle$  of the gas in the target tank between extraction system and Doppler spectroscopy viewing point.

The measurements were done with a gas type independent capacitive vacuum gauge (type PFEIFFER CMR-274 compact capacitance gauge) and without plasma or beam, respectively. The measurement point at the target tank was located on top of the vessel approximately above the pumping ports. For the source pressure measurements, the vacuum gauge was attached to the back plate of the source with a  $\approx 30$  cm long vacuum tube.

For the spectroscopic measurements of the beam and the ion source at GLADIS, two different parameter scans were performed: An RF power sweep from 15 kW to 27 kW at a constant gas pressure of  $p_{source} = 1.26$  Pa (Valve setting 4), and a pressure sweep at two different RF powers. At  $P_{RF} = 22$  kW, pressures of 0.82 Pa, 1.26 Pa and 1.45 Pa were set. At  $P_{RF} = 26$  kW the pressure settings were 1.26 Pa, 1.46 Pa and 1.73 Pa. Using two different power settings was necessary in order to keep the ion source within the operational limits given by the perveance matching.

### 5.2.3 Results

#### Target thickness and ion source pressure.

The pressure measurements in the target tank show that for all gas valve settings within the operational range, i.e Gas 3 - Gas 7, the pressure ranges from 0.08 Pa to 0.23 Pa. Assuming a travel length of the beam through the neutral background gas of 3 m, this high enough to provide an infinitely thick neutraliser target for all these gas valve settings. For the calculation of  $\langle nL \rangle$ , a background gas temperature of 300 K was assumed. Gas heating by the beam may lower these values, however [SCC<sup>+</sup>02, SC03]. The estimated target thicknesses are plotted in Fig. 5.12.

The source pressure measurements show that in the operational range of GLADIS, cold gas pressures lie in the range between 0.82 Pa and 1.92 Pa. The values are displayed in Fig. 5.13. This is still somewhat higher than in negative hydrogen ion source experiments at the IPP that use a similar driver, but placed onto an expansion chamber<sup>3</sup> to provide spatial separation of excitation region and extraction region; these negative ion sources operate at 0.3 Pa design value with

---

<sup>3</sup>This chamber is e.g. the body of a JET arc PINI including some confinement magnets, but without filaments.

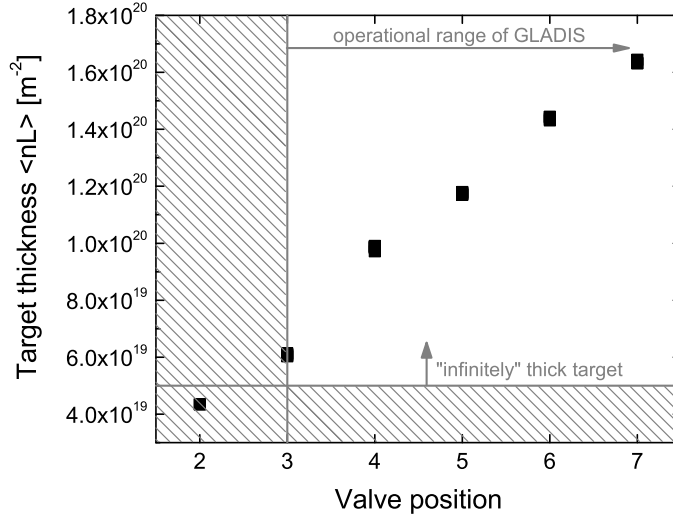


**Figure 5.12:** Neutraliser target thicknesses at GLADIS depending on gas valve setting. The tank is pressurized solely by gas streaming from the ion source. For  $\langle nL \rangle \geq 5 \cdot 10^{19} \text{ m}^{-2}$ , the target can be considered infinitely thick [FVS98].

RF input powers of around 80 kW to 150 kW [SFF<sup>+</sup>06].

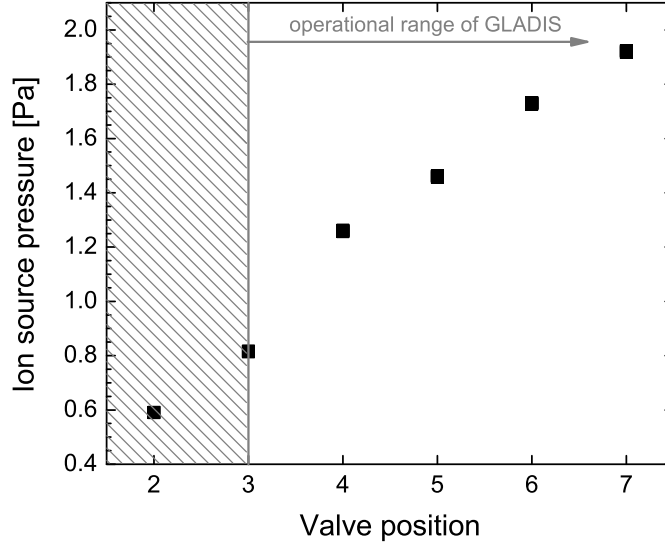


**Figure 5.13:** Pressure measurements in the GLADIS ion source depending on gas valve setting. The source can't be operated below valve setting 3.

### Electron density and temperature

As already discussed in section 3.4, the absolute evaluation of the Balmer series

is only able to show that the electron temperature  $T_e$  is 6 eV or more. Therefore, variations of  $T_e$  with  $P_{RF}$  or  $p_{source}$  could not be measured. It is expected however that  $T_e$  is independent of  $P_{RF}$  at constant pressure [FKV<sup>+</sup>99]. With increasing  $p_{source}$ , the electron temperature is expected to decrease. This is due to a longer ion confinement time in the ionisation balance at higher pressures [Fan01].

The RF power sweep showed that the electron density  $n_e$  is in good approximation proportional to  $P_{RF}$ . It increases from  $2.1 \cdot 10^{17} \text{ m}^{-3}$  at 15 kW to  $3.8 \cdot 10^{17} \text{ m}^{-3}$  at 27 kW. The sweep was performed at constant cold gas pressure of 1.26 Pa. This means a constant initial neutral particle density of  $n_0 = 3.0 \cdot 10^{20} \text{ m}^{-3}$ . Therefore, the degree of ionisation  $\alpha \approx n_e/n_0$  increases accordingly from  $6.9 \cdot 10^{-4}$  to  $1.2 \cdot 10^{-3}$ . This can be seen in Fig. 5.14.

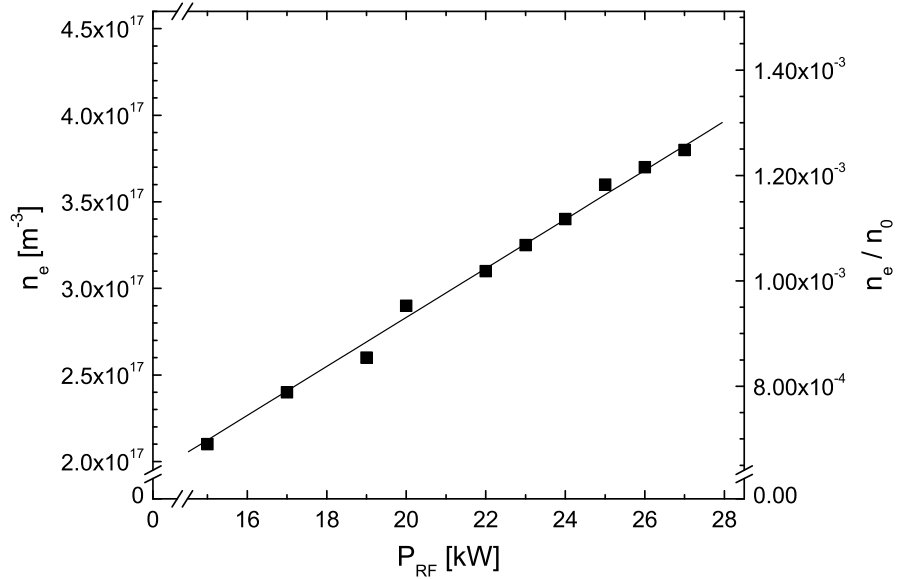


**Figure 5.14:** Electron density respectively degree of ionisation depending on the RF input power, measured at GLADIS. The cold gas pressure was constant at 1.26 Pa.

An increase of the gas pressure at constant RF power also increases the electron density from  $2.1 \cdot 10^{17} \text{ m}^{-3}$  at 0.82 Pa to  $3.3 \cdot 10^{17} \text{ m}^{-3}$  at 1.46 Pa with  $P_{RF} = 22$  kW and from  $3.7 \cdot 10^{17} \text{ m}^{-3}$  at 1.26 Pa to  $4.2 \cdot 10^{17} \text{ m}^{-3}$  at 1.73 Pa with  $P_{RF} = 26$  kW. The variation of  $n_e$  with  $p_{source}$  also appears to depend on the RF power. For higher  $P_{RF}$ , the variation is smaller. This can be seen in Fig. 5.15.

However, the neutral particle density is also higher for a higher pressure. As a result, the degree of ionisation actually drops slightly from  $1.06 \cdot 10^{-3}$  to  $9.4 \cdot 10^{-4}$

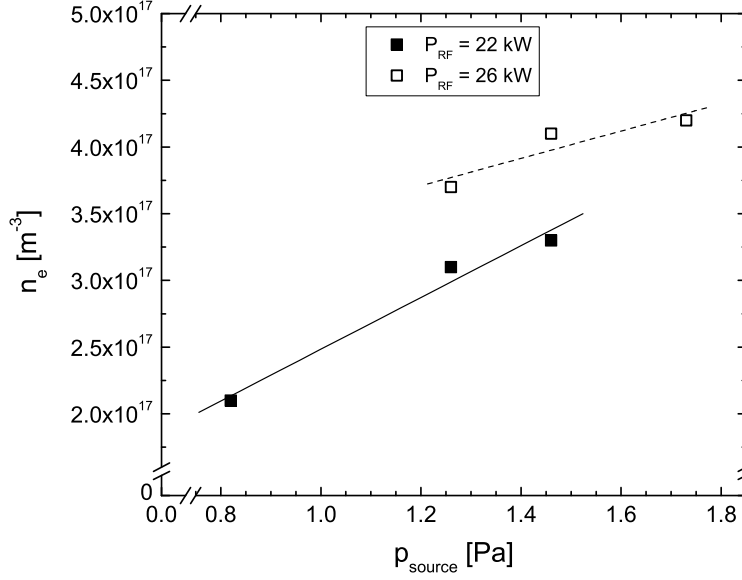


**Figure 5.15:** Electron density depending on the gas pressure, measured at GLADIS.

at 22 kW and from  $1.22 \cdot 10^{-3}$  to  $1.01 \cdot 10^{-3}$  at 26 kW. This is shown in Fig. 5.16.

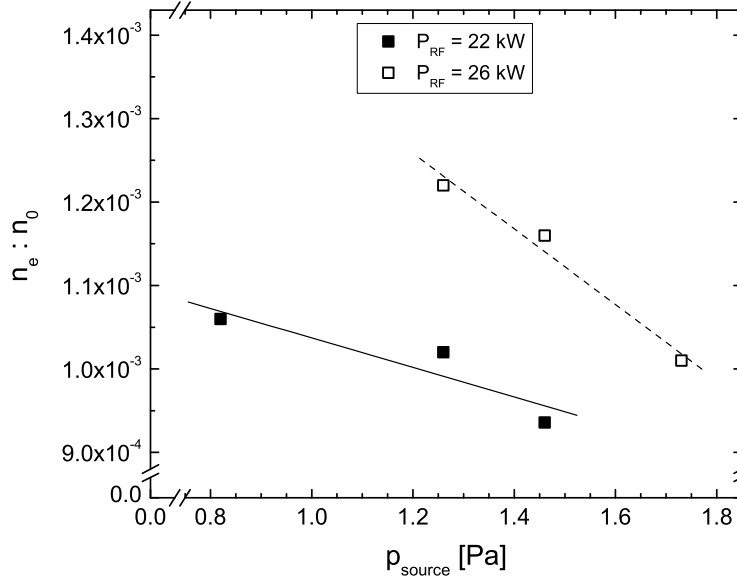


**Figure 5.16:** Degree of ionisation depending on the gas pressure, measured at GLADIS.

#### Ion species distribution and atom to molecule ratio.

The Doppler spectroscopy of the beam reveals an increase of the proton fraction



with  $P_{RF}$  at constant pressure. The  $H_2^+$  fraction turns out to be very close to the proton fraction over the whole parameter range, rising only slightly less. The  $H^+$  fraction rises from 34.1% at 15 kW to 42.2% at 27 kW, becoming the largest species fraction at high power, and the  $H_2^+$  fraction increases from 34.5% to 40.3%. The  $H_3^+$  fraction drops from 31.4% at 15 kW to 17.5% at 27 kW. The behaviour of all three ion species fractions is very smooth in the observed range. The results are shown in Fig. 5.17.

The atom to molecule ratio  $n_H/n_{H_2}$  in the ion source measured by the intensity ratio of the  $H_\gamma$  line to the Fulcher band increases with the RF power. It ranges from 0.067 at 15 kW to 0.099 at 27 kW, at a constant cold gas pressure of 1.26 Pa. The values are displayed together with the species distribution in Fig. 5.17.

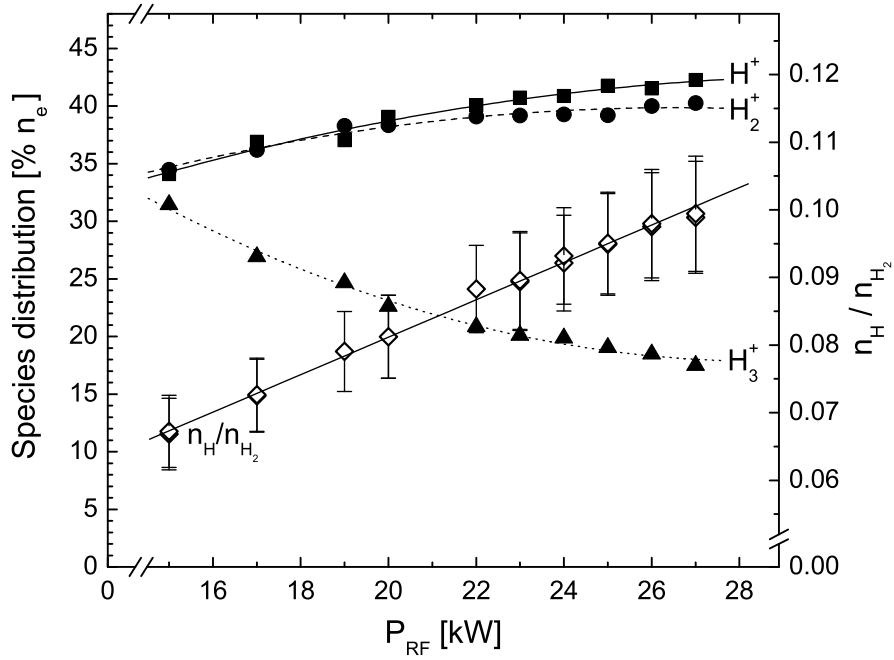


**Figure 5.17:** Species distribution and atom to molecule ratio versus RF input power measured at the GLADIS high heat flux test bed. The cold gas pressure was constant at 1.26 Pa.

The mechanisms behind the observed behaviour can be best seen in a plot of the absolute particle densities that is shown in Fig. 5.18. Both  $n_{H^+}$  and  $n_{H_2^+}$  both increase approximately parallel to  $n_e$ . The increase of  $n_{H^+}$  with  $P_{RF}$  is slightly stronger because the atom density  $n_H$  also rises.  $n_{H_3^+}$  stays constant. The reason is that it can only be produced by the reaction  $H_2^+ + H_2 \rightarrow H_3^+ + H$ . The reaction rate of this process strongly depends on the mean free path length of  $H_2^+$  and accordingly on the gas pressure, which was constant during the RF power sweep.

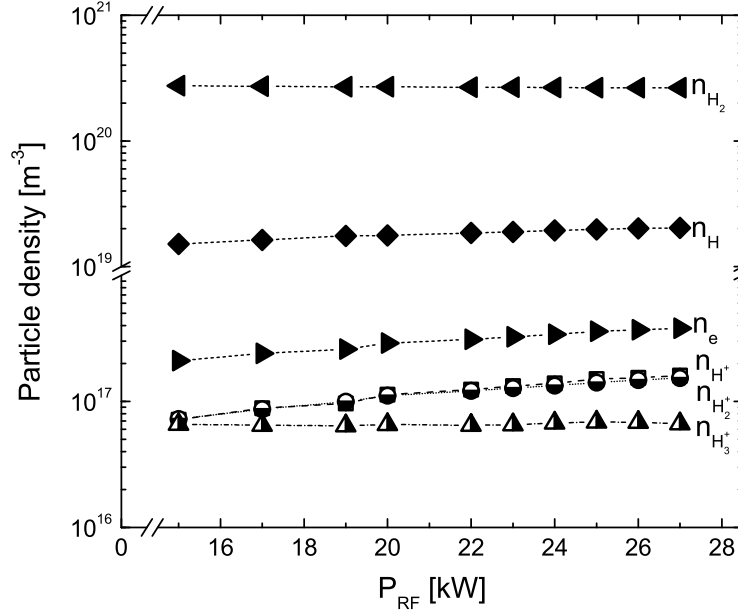


**Figure 5.18:** Absolute particle densities versus RF input power in the ion source measured at the GLADIS high heat flux test bed.  $n_e$  and  $n_H$  are derived from the absolute evaluation of the Balmer series.  $n_{H^+}$ ,  $n_{H_2^+}$  and  $n_{H_3^+}$  are calculated by scaling the ion species distribution with  $n_e$ .  $n_{H_2}$  is derived from the gas pressure.

The pressure sweep shows a significant decrease of the  $H_2^+$  fraction with increasing  $p_{source}$ , subsequently giving rise to the  $H^+$  and also  $H_3^+$  fractions. This is shown in Fig. 5.19. At 0.82 Pa and 22 kW,  $H_2^+$  is the majority ion species with the fraction of 51.3%, which decreases to 28.8% at 1.73 Pa and 26 kW. Accordingly, the  $H^+$  fraction rises from 37.7% to 46.8%, and the  $H_3^+$  fraction from 11.0% to 24.4%. The necessary switching from  $P_{RF} = 22$  kW to  $P_{RF} = 26$  kW is visible in the form of a slight increase of the  $H^+$  and  $H_2^+$  fractions with an according decrease of  $H_3^+$ . This was to be expected with the results from the power sweep. However, the influence of  $p_{source}$  is considerably stronger than that of the  $P_{RF}$  switching, possibly also due to the much greater relative increase of the pressure.

Comparing the observed values with measurements presented in [KFH<sup>+</sup>01] (see Fig. 5.20), it has to be considered that the latter measurements were taken at higher RF power (37 kW), and the pressure scale is expressed in gas flow units. Despite these differences, the results obtained here are in the same range and show the same general behaviour with increasing pressure respectively gas flow. Extrapolating the results from the RF power sweep, the much lower  $H_3^+$  fraction in [KFH<sup>+</sup>01] can be attributed to the higher  $P_{RF}$  setting.

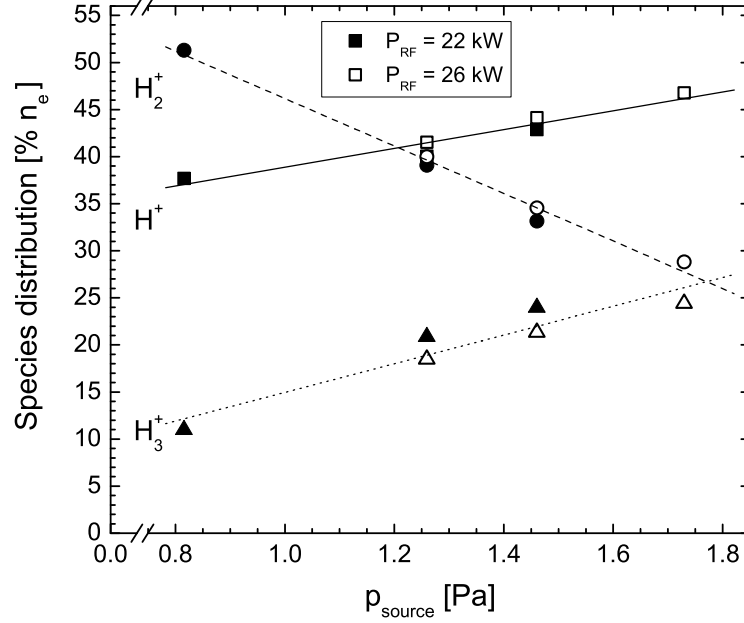


**Figure 5.19:** Species distribution versus gas pressure in the ion source measured at the GLADIS high heat flux test bed.

The sweep of the gas pressure also shows that the atom to molecule ratio decreases with increasing pressure as can be seen in Fig. 5.21. At  $P_{\text{RF}} = 22$  kW the values drop from 0.106 at 0.82 Pa to 0.082 at 1.46 Pa, and at  $P_{\text{RF}} = 26$  kW they drop from 0.098 at 1.26 Pa to 0.083 at 1.73 Pa. Comparing the values at equal pressure for both RF powers, the atom to molecule ratio is higher for the 26 kW setting. Also, the decrease of the atom to molecule ratio with increasing pressure seems to be slightly less at the higher RF power.

To understand the seemingly contradictory behaviour of the atom to molecule ratio and the ion species distribution, it is helpful to look at the absolute particle densities. These are shown in Fig. 5.22. It can be seen that the hydrogen atom density actually stays constant while the density of the  $\text{H}_2$  molecules increases with the pressure. The density of  $\text{H}^+$  ions increases by about the same factor as the electron density. The  $\text{H}_2^+$  density stays approximately constant.

In other words, the degree of ionisation of the atoms  $n_{\text{H}^+}/n_{\text{H}}$  increases together with  $n_e$ , while the degree of ionisation for the molecules  $n_{\text{H}_2^+}/n_{\text{H}_2}$  becomes smaller. Considering that the ionisation energy is 13.6 eV for hydrogen atoms and 15.6 eV for the molecules, this behaviour can be explained by a reduction of the electron

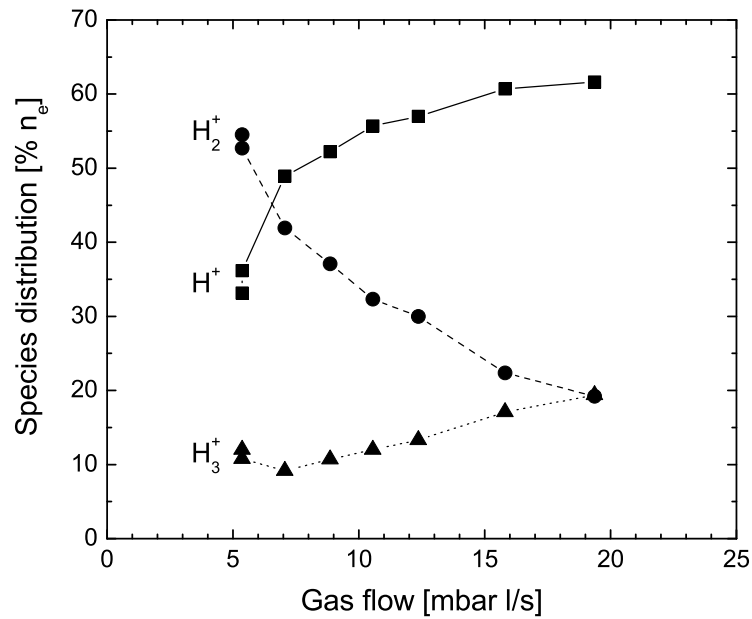


**Figure 5.20:** Ion species distribution depending on the gas flow, measured at the original WENDELSTEIN 7-AS ion source with  $P_{RF} = 37$  kW [KFH<sup>+</sup>01].

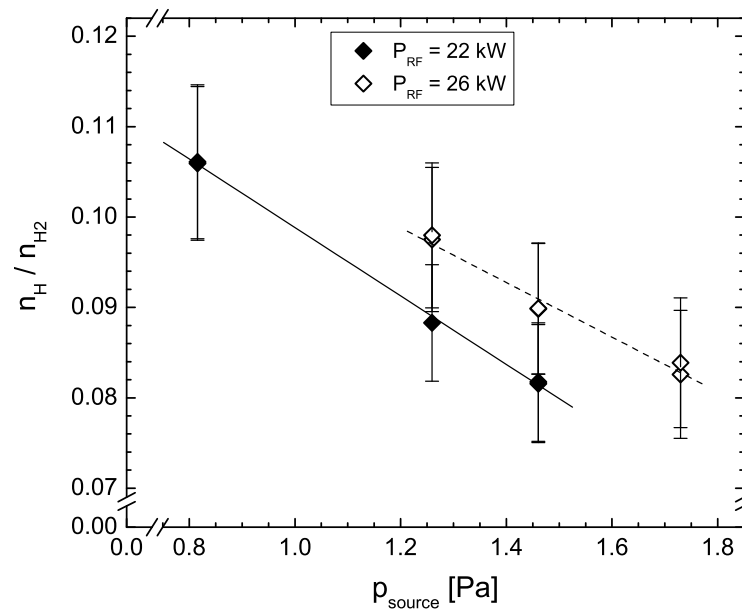


**Figure 5.21:** Atom to molecule ratio versus gas pressure in the ion source measured at the GLADIS high heat flux test bed.

temperature due to the higher pressure. The increase of the  $\text{H}_3^+$  density is due to the process  $\text{H}_2^+ + \text{H}_2 \rightarrow \text{H}_3^+ + \text{H}$  becoming more effective for higher molecule densities. This also reduces the  $\text{H}_2^+$  fraction at higher pressures.

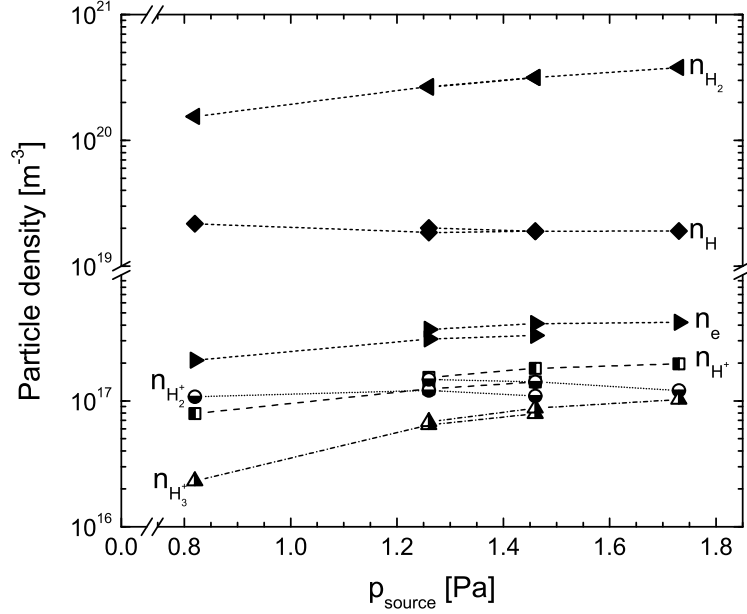


**Figure 5.22:** Absolute particle densities versus gas pressure in the ion source measured at the GLADIS high heat flux test bed.  $n_e$  and  $n_H$  are derived from the absolute evaluation of the Balmer series.  $n_{H^+}$ ,  $n_{H_2^+}$  and  $n_{H_3^+}$  are calculated by scaling the ion species distribution with  $n_e$ .  $n_{H_2}$  is derived from the gas pressure.

The values for  $n_H/n_{H_2}$  presented in Figs. 5.17 and 5.21 were measured with grating 3 of the ANDOR SR303i using the measurement method for the Fulcher band described in section 3.6. For a verification of these measurements, the Fulcher band radiation was also estimated by integrating over the wavelength range from 600 nm to 638 nm where the diagonal vibrational transitions  $v' = v'' = 0, 1, 2, 3$  can be found. For this, gratings 1 and 2 were used because the whole wavelength range could be measured in a single exposure. These integrals showed the same tendency as the values from the detailed evaluation. The absolute values of the integrals were lower, however, because the integration range did not cover the complete Fulcher transition. A mean scaling factor from the measured wavelength range to the whole Fulcher band of  $1.50 \pm 0.02$  was experimentally derived by comparing the integrals with the extrapolated values from the high resolution measurement. Calculation of  $n_H/n_{H_2}$  from the intensity ratio of the  $\text{H}_\gamma$  line and the Fulcher band measured with gratings 1 and 2 yields values well within the

error margin of the values obtained with grating 3. This can be seen in Fig. 5.23 for the RF power sweep and in Fig. 5.24 for gas pressure sweep.

The atom to molecule ratio obtained from absolute measurements of the Balmer series yields the same tendencies as the values derived from the intensity ratio of atomic and molecular radiation as can be seen in in Figs. 5.23 (RF power sweep) and 5.24 (gas pressure sweep). The absolute values are systematically lower, however (apart from a single measurement at 0.82 Pa / 22 kW). Similar observations concerning the absolute values were made e.g. by [Heg02] and [Reg05]. This discrepancy is also a topic of ongoing research at the Lehrstuhl für Experimentelle Plasmaphysik at the University of Augsburg.

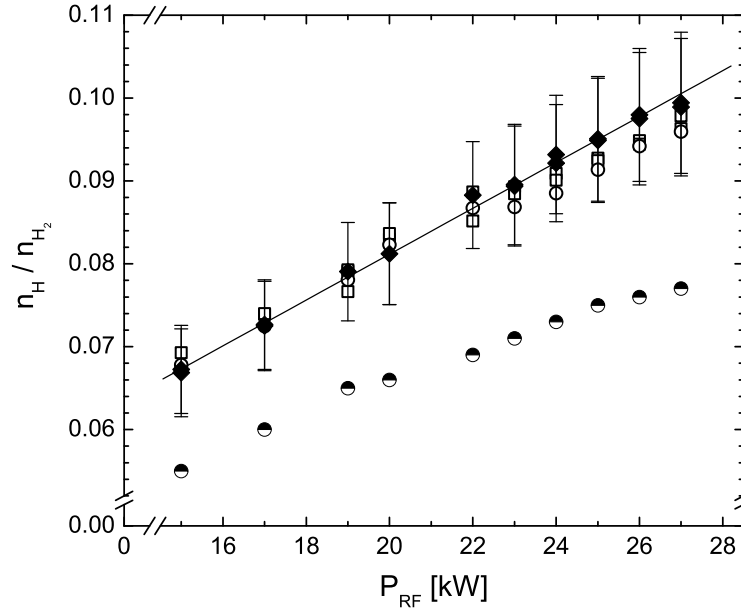


**Figure 5.23:** Comparison of the atom to molecule ratios measured in hydrogen at GLADIS and depending on  $P_{RF}$ . Diamonds: grating 3; open circles: grating 2; open squares: grating 3; half-filled circles: from absolute measurements of Balmer lines.

### Gas temperature and vibrational population.

The gas temperature  $T_{gas}$  and vibrational temperature  $T_{vib}$  were also derived from the measurement of the Fulcher band with grating 3 of the ANDOR SR303i, with the methods described in section 3.5.3.

The gas temperature is almost independent from  $P_{RF}$ , with an average of around 1070 K. The power sweep shows the same minute decrease with increasing  $P_{RF}$  that is observed at the ASDEX Upgrade RF source. The absolute decrease still lies well within the error margin, however, as can be seen in Fig. 5.25. A possible

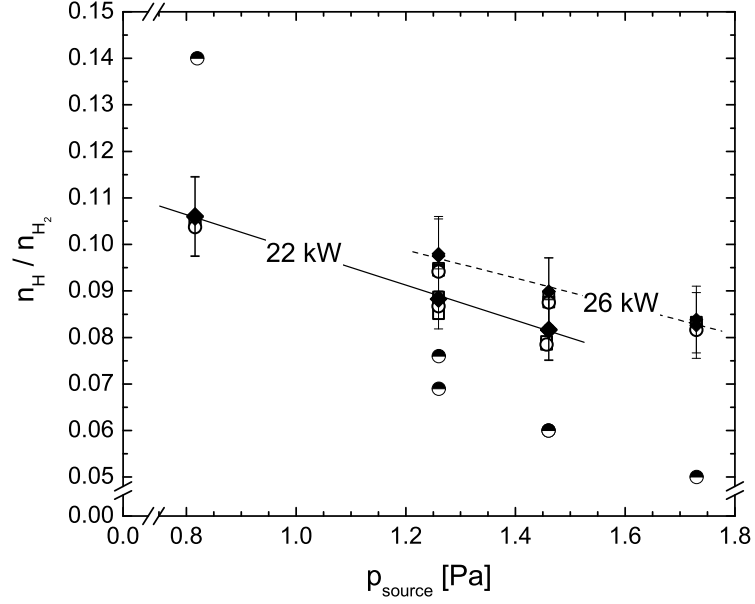


**Figure 5.24:** Comparison of the atom to molecule ratios measured in hydrogen at GLADIS and depending on  $p_{\text{source}}$ . Diamonds: grating 3; open circles: grating 2; open squares: grating 3; half-filled circles: from absolute measurements of Balmer lines.

explanation for this has already been given in section 5.1.3.

The pressure sweep on the other hand shows a significant increase of the  $T_{\text{gas}}$  with rising  $p_{\text{source}}$  from  $900 \pm 110$  K at 0.82 Pa / 22 kW to  $1170 \pm 160$  K at 1.73 Pa / 26 kW. This is shown in Fig. 5.26. As in the power sweep, the values with higher  $P_{\text{RF}}$  at equal pressure have a 30 K to 60 K smaller  $T_{\text{gas}}$ . This is well smaller than the error margin on the individual points, but again systematic.

This increase of  $T_{\text{gas}}$  with increasing pressure can be understood as a result of reduced diffusion. At higher pressures, the diffusion of neutral particles to the water-cooled walls is reduced. Therefore, the gas has a better thermal insulation and can reach higher temperatures [Heg02]. The underlying mechanism is thus similar to the one causing a decrease of  $T_{\text{gas}}$  with  $P_{\text{RF}}$ . The difference is that during the pressure sweep, the diffusion is influenced mainly by the pressure, whereas during the power sweep the fraction of the more mobile atoms is increased.

The relative vibrational populations were derived from the measurement of the Fulcher band with grating 3 of the ANDOR SR303i. They don't fit very well

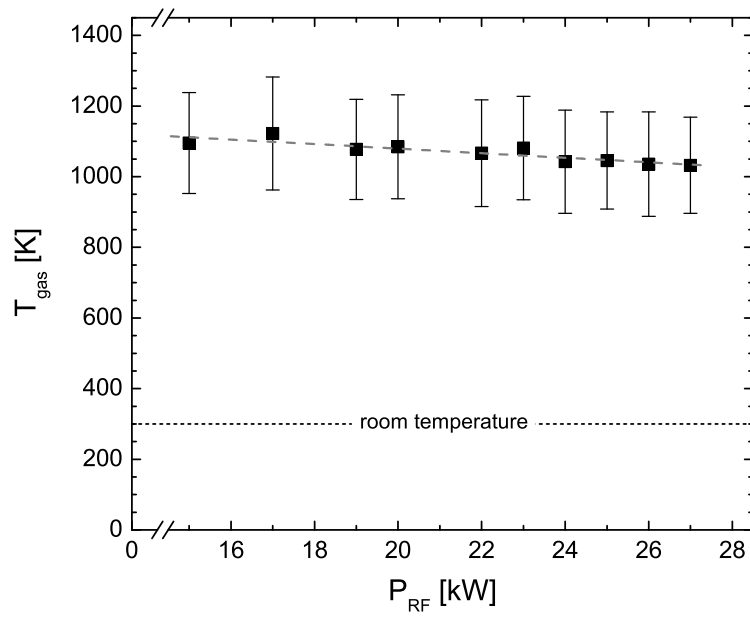


**Figure 5.25:** Gas temperature in hydrogen depending on the RF input power at constant pressure, measured at GLADIS.

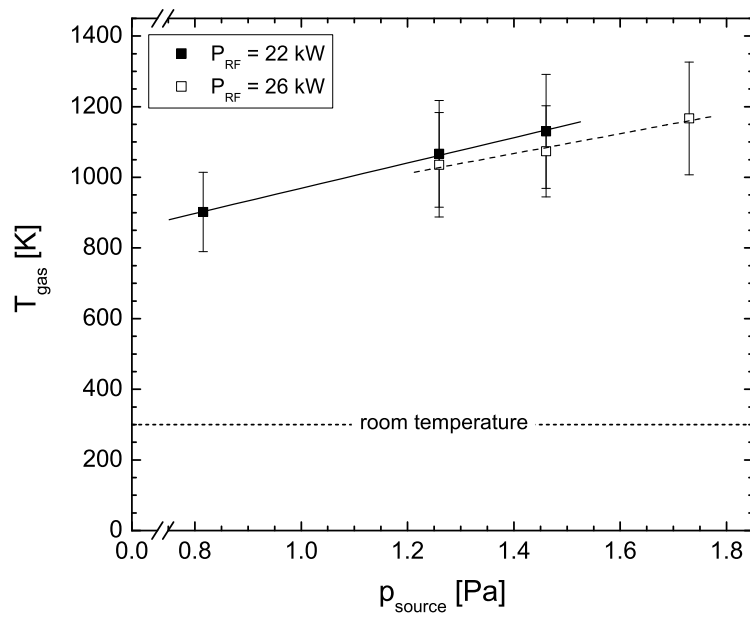


**Figure 5.26:** Gas temperature in hydrogen depending on the gas pressure, measured at GLADIS.



to the theoretical populations calculated from an assumed  $T_{vib}$  in the electronic ground state, as can be seen in Fig. 5.27. The vibrational populations in  $d^3\Pi_u$  appear to be depleted for  $v' = 2$  and  $v' = 3$ . This could be due to processes like predissociation, associative attachment or auto-ionisation which depopulate especially higher vibrational states with  $v' \geq 3$ . These processes were not included in the modelling of the theoretical vibrational populations (see section 3.5.3).

There is no observable variation of the vibrational population with  $P_{RF}$ . However, an increase in  $p_{source}$  appears to cause a slightly stronger depletion of the  $v' = 2$  and  $v' = 3$  levels, as shown in Fig. 5.27.

Considering the error bars, the vibrational temperature is estimated to be between 5000 K and 10000 K. Since there is no good agreement between the measured population and any one of the modelled ones however, the ground state population might be in fact non-thermal (see section 3.5.3).

The error margins were derived from the uncertainty in  $f_v(T_{rot})$  through the rotational temperatures  $T_{rot}$ . Since the populations  $n(v')$  are normalized to  $n(v' = 0)$ , the data point for  $v' = 0$  does not have error bars, and the margins for  $v' > 0$  are increased accordingly by the uncertainty of  $n(v' = 0)$ .

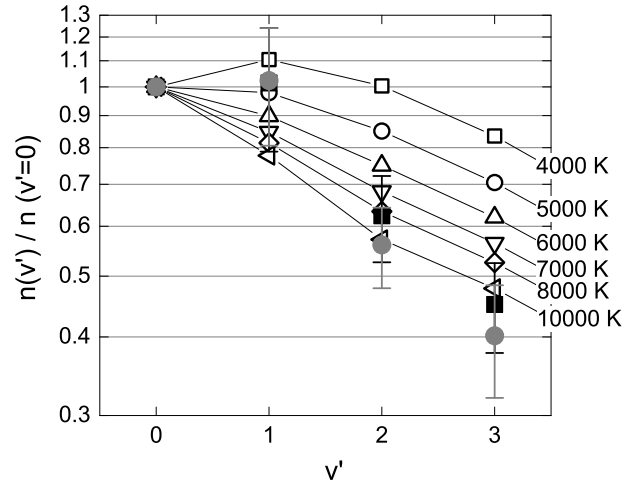


**Figure 5.27:** Vibrational populations of the hydrogen  $d^3\Pi_u$  state at GLADIS for  $P_{RF} = 26$  kW: black squares: 1.26 Pa, grey circles: 1.73 Pa. Open symbols represent calculated populations.

The stronger depopulation with increasing pressure might point towards a heavy particle effect, although the heavy particle densities of the observed plasmas are unusually small for this [Heg02]. It could also be interpreted as an increase of  $T_{vib}$  with the pressure. However, the agreement between theory and measurement is not good enough to warrant a definitive statement.

### 5.3 Comparison of the RF sources

This section compares the investigated RF sources with each other. Isotope effects are also discussed. Additionally, the results from GLADIS are extrapolated to typical RF input powers and gas pressures for the driver of a negative hydrogen ion source at the IPP [SFF<sup>+</sup>06]. Such a driver has the same geometry as the GLADIS source, but is placed onto an expansion chamber. A comparison to the arc-driven PINI sources at JET is the aim of future investigations.

#### Electron density and temperature

The measurements at GLADIS show that at constant pressure, the electron density is proportional to the RF input power. It also increases with the gas pressure, but not as strongly as the neutral particle density. This means that in the RF PINI, significantly higher electron densities are to be expected due to higher pressure and RF power. At the same time, the electron temperature is expected to be lower because of the higher pressure. Spectroscopically measured values of  $T_e$  and  $n_e$  could not be obtained for the RF PINI.

Comparing typical operating parameters of  $p_{source} = 0.3$  Pa and  $P_{RF} = 100$  kW in the driver of a negative ion source [SFF<sup>+</sup>06] with 27 kW at 1.26 Pa at GLADIS, about four times the electron density of is expected due to the four times higher RF power. This is countered by the decrease in pressure by also a factor four. Since the decrease of  $n_e$  for lower pressures appears to be smaller for high powers (see Fig. 5.15), a net increase of  $n_e$  up to the range of  $\geq 1 \cdot 10^{18} \text{ m}^{-3}$  is expected. This is backed by measurements presented in [FFF<sup>+</sup>06]. Because of the lower pressure, the electron temperature is expected to be higher in the driver of a negative ion source. It is estimated at  $\approx 8$  eV by [FFF<sup>+</sup>06].

#### Atom to molecule ratio

For both the RF source at GLADIS and the RF PINI, the atom to molecule ratio  $n_H/n_{H_2}$  increases with  $P_{RF}$  due to the higher electron density. The pressure sweep at GLADIS shows that  $n_H/n_{H_2}$  decreases for higher pressures. Comparing the measurements at the RF PINI in hydrogen with those at GLADIS, the atom to molecule ratio is comparatively low for the PINI:  $n_H/n_{H_2} = 0.112$  for 85 kW and 2.5 Pa. The GLADIS source reaches a  $n_H/n_{H_2}$  of up to 0.099 at a significantly lower RF power of 27 kW and a pressure of 1.26 Pa. This is due to the higher pressure in the RF PINI. Furthermore, the RF power density is

increased by much less than the total RF power because the PINI has a larger volume. Comparing the results in deuterium and hydrogen, the atom to molecule ratio is about twice as high in deuterium due to a higher electron density.

Extrapolating the results from GLADIS to  $p_{source} = 0.3$  Pa and  $P_{RF} = 100$  kW for a negative hydrogen ion source, a significantly higher atom to molecule ratio is to be expected. Both the lower pressure and the higher RF power enhance the dissociation of the  $H_2$  molecules. A rough extrapolation from the pressure and power sweeps suggests  $n_H/n_{H_2} > 0.3$ . This is well in agreement with [FFF<sup>+</sup>06].

### Ion species distribution

The ion species distribution can be controlled by varying the RF power as well as the gas pressure. Both the measurements at the RF PINI and at the GLADIS source show that the higher atom to molecule ratio at higher RF power increases the fraction of atomic ions. At the same time, the fraction of  $H_3^+$  (respectively  $D_3^+$  ions is reduced. The  $H_2^+$  respectively  $D_2^+$  fraction follows different tendencies for the two sources, however. It stays almost equal to the  $H^+$  fraction for the GLADIS source. For the RF PINI, the  $D_2^+$  is considerably lower than the  $D^+$  fraction and depends only little on  $P_{RF}$ , while the  $D^+$  fraction rises.

The pressure sweep at GLADIS showed that the  $H_2^+$  fraction decreases strongly when the pressure is increased. At the same time, the  $H^+$  and  $H_3^+$  fractions rise. This is explained by the reduction of  $T_e$  and the increase of the reaction rate of  $H_2^+$  with  $H_2$ . A comparison of the measurements at GLADIS and at the RF PINI in hydrogen shows effects of increasing both  $P_{RF}$  and  $p_{source}$  at the same time: the atomic ion fraction increases strongly while the  $H_2^+$  fraction decreases. The  $H_3^+$  fraction stays almost constant. The reason is that increases in  $P_{RF}$  and  $p_{source}$  both tend to increase the  $H^+$  fraction, while they approximately cancel their effects on  $H_3^+$ . With this background, the different behaviour of the  $H_2^+$  respectively  $D_2^+$  fraction in both sources can also be understood as an effect of the higher pressure in the RF PINI.

Extrapolating the tendencies for the ion species distribution at GLADIS to the driver of negative ion sources, it is expected that the largest fraction is made up by  $H_2^+$  because of the lower pressure and accordingly high electron temperature. Considering that both low pressure and high RF power lead to a smaller  $H_3^+$  fraction, it is expected to be very small. The remaining ions are  $H^+$  ions. Because of the relatively high atom to molecule ratio, they should still constitute a significant fraction of the ion density. In negative ion sources, the ion species distribution cannot be measured by Doppler spectroscopy of the beam because

only  $\text{H}^-$  ions (and electrons) are extracted.

### Gas temperature

The gas temperature in hydrogen is higher at the RF PINI than at GLADIS due to the higher pressure in the RF PINI. Although for the RF PINI the gas temperature in deuterium is slightly lower than in hydrogen, the higher pressure is still sufficient to reach higher temperatures than at GLADIS.

Comparable gas temperatures around 1200 K in hydrogen were measured in a negative hydrogen ion source experiment [FFF<sup>+</sup>06]. They showed the same general behaviour as at GLADIS, i.e. increasing with pressure and staying approximately constant with  $P_{RF}$ .

### Vibrational population

The vibrational temperatures measured in deuterium at the RF PINI are lower than those measured in hydrogen both the RF PINI and at GLADIS. The reason is the higher mass of deuterium, as was already explained in section 5.1.3. The vibrational populations in hydrogen are very similar for both ion sources, however. The observed depletion of the higher vibrational levels in  $d^3\Pi_u$  is even greater at the RF PINI than at GLADIS. This tends to support the assumption that this is related to the gas pressure (which is higher for the RF PINI).

The reason why the measured vibrational populations in deuterium show a better agreement with the calculated ones than those measured in hydrogen might be the higher mass of deuterium.  $\text{H}_2$  is a very light molecule, so the Born-Oppenheimer approximation is not as good as for heavier molecules (e.g.  $\text{Cl}_2$ ). Since  $\text{D}_2$  has twice the mass of  $\text{H}_2$ , it can be expected that any deviations from the Born-Oppenheimer approximation are reduced for  $\text{D}_2$ . This can also explain why the measurement errors for rotational temperatures measured in hydrogen are larger than in deuterium.

The vibrational temperatures that were measured at a negative ion source experiment in hydrogen are similar to those at GLADIS [FFF<sup>+</sup>06]. However, they show a slight reduction of  $T_{vib}$  for a higher  $P_{RF}$ , while at GLADIS, no such behaviour is observed. The values for  $T_{vib}$  at the negative ion source show an increase with the gas pressure. The observed stronger depletion of  $v' = 2$  and  $v' = 3$  at GLADIS with increasing pressure could also be interpreted as a temperature increase.

## 5.4 Synopsis

To summarise the results from these measurements, it can be stated that at constant cold gas pressure  $p_{source}$ , the electron density  $n_e$  and the degree of ionisation are proportional to the RF input power  $P_{RF}$ . A higher  $n_e$  in turn causes the atom to molecule ratio to rise, which ultimately enhances the proton fraction. A variation of the electron temperature  $T_e$  could not be measured due to limitations of the measurement method; only a lower bound of  $T_e \geq 6$  eV can be stated. However, it is assumed that  $T_e$  does not change with  $P_{RF}$  and decreases for higher pressures.

An increase of the gas pressure has a strong influence on the ion species distribution. The production of  $H^+$  is increased with respect to  $H_2^+$  because of the reduced electron temperature. Another process is the conversion of  $H_2^+$  into  $H_3^+$  through collisions with molecular hydrogen at higher pressures. This increases the  $H_3^+$  fraction and further reduces the  $H_2^+$  fraction. Although  $n_e$  increases with the pressure, the overall degree of ionisation decreases slightly.

Increasing the gas pressure also causes the gas temperature to rise, whereas the RF power has little to no effect on  $T_{gas}$ . The determination of the vibrational temperature is difficult especially in hydrogen. Variations of the excited state vibrational population with the RF power could not be observed. An increase of  $T_{vib}$  with  $p_{source}$  in hydrogen is a possible explanation for the stronger depletion of  $v' = 2$  and  $v' = 3$  at higher pressures.

The measurements in deuterium show a higher atom to molecule ratio and accordingly a higher atomic ion fraction than those in hydrogen. This can be explained by a higher electron density. The vibrational temperature in deuterium is lower than in hydrogen because of the higher mass. The gas temperature in deuterium is also slightly lower, which is due to the higher atom to molecule ratio and the less efficient energy transfer between electrons and heavy particles.

While the concrete realisation of the ion source as well as the gas type strongly influence the absolute values of the measured parameters, the observed tendencies appear to be applicable to different RF driven positive hydrogen ion sources. The measured values can also be extrapolated to the RF driven sources for negative hydrogen ions that are being developed at the IPP in Garching. Especially important is the ion species distribution that cannot be measured by Doppler spectroscopy of a negative hydrogen ion beam.



## 6 Summary

Both the source plasma and the extracted particle beam have been investigated spectroscopically for two different RF-driven sources of positive hydrogen ions. One is part of the neutral beam injection (NBI) system of the fusion experiment ASDEX Upgrade, and the other one is operated at the materials testing facility GLADIS. While both ion sources use the same method of plasma generation, they differ in size and geometry, and operate at different RF input powers and gas pressures. Furthermore, the NBI source could be operated in deuterium as well as in hydrogen. The GLADIS system is designed only for operation in hydrogen.

Measurements at a high powered arc-driven PINI ion source, whose geometry is similar to the RF ion source at ASDEX Upgrade, could not be carried out due to system outages. A comparison between this ion source and the ones that were already investigated here would be of interest.

Relative intensity measurements of the radiation of the ion source plasma yielded information about the atom to molecule ratio, the gas temperature and the vibrational population of the hydrogen molecules. Absolute spectroscopic measurements made the determination of the electron density and temperature possible. They also provided a second method of measuring the atom to molecule ratio. The species distribution of atomic and molecular hydrogen ions could be derived from  $H_\alpha$  Doppler spectroscopy of the extracted particle beam. The combination of the measurements at the ion source and at the beam for different RF input powers and gas pressures allowed the correlation of the ion species distribution with the source plasma parameters. The ion species distribution in the extracted beam is assumed to also be a measure for the species distribution inside the ion source.

At ASDEX Upgrade, a sweep of the RF power from 57 kW to 87 kW was performed in deuterium at a constant pressure of about 2.5 Pa. An additional

measurement with an RF power of 85 KW at 2.5 Pa was performed for hydrogen to study the influence of the isotope on the measured values and to make a comparison with the ion source at GLADIS possible.

In deuterium, the atom to molecule ratio is between 0.15 and 0.21 and increases with the RF power. Because of this, the fraction of  $D^+$  ions also increases from 61% to 70%. At the same time, the  $D_3^+$  fraction halves from 14% to 7%, while the  $D_2^+$  fraction drops only marginally from 25% to 23%. The measured ion species distributions agree well with previous investigations and could now be correlated to the atom to molecule ratio.

The gas temperature is in the order of 1150 K and nearly independent from the RF power. The vibrational temperature is in the range of 4000 K. A systematic dependence on the RF power cannot be identified.

In hydrogen, the atom to molecule ratio is only 0.11 and thus about half as high as at a comparable input power in deuterium. Accordingly, the atomic ion fraction is also lower at 55%, and the fraction of the molecular ions is higher: 29% for  $H_2^+$  and 17% for  $H_3^+$ .

The gas temperature of about 1230 K is higher than in deuterium. This can be explained by the atom to molecule ratio being smaller and the energy transfer between electrons and heavy particles being more effective for the lighter hydrogen. It is difficult to state a vibrational temperature in hydrogen because the measured populations in the  $d^3\Pi_u$  state of the hydrogen molecule do not agree well with calculated populations based on a thermal population in the ground state. The measurements suggest a vibrational temperature of at least 6000 K, however. The difference to deuterium is due to the larger mass of  $D_2$ .

The electron density and temperature could not be measured at ASDEX Upgrade because an absolute calibration of the spectroscopic system could not be performed.

At GLADIS, an RF power sweep from 15 kW to 27 kW at a constant gas pressure of 1.26 Pa and a pressure sweep from 0.82 to 1.73 Pa were performed. During the pressure sweep, the RF power had to be increased from 22 kW to 26 kW to remain within the operational limits of the ion source.

The absolute evaluation of the Balmer series shows that the electron temperature is 6 eV or more. A more precise statement cannot be made because the evaluation method is insensitive to the electron temperature in this temperature range. It is assumed that it is independent from the RF power and decreases for higher gas pressures.



The electron density derived from the absolute Balmer radiation increases proportionally to the RF power from  $2.1 \cdot 10^{17} \text{ m}^{-3}$  to  $3.8 \cdot 10^{17} \text{ m}^{-3}$ . Accordingly the degree of ionisation also rises from  $6.9 \cdot 10^{-4}$  to  $1.2 \cdot 10^{-3}$ . This causes an increase of the atom to molecule ratio. The intensity ratio of the  $H_\gamma$  and the molecular Fulcher band suggests values between 0.067 and 0.099. The absolute evaluation of the Balmer series yields systematically lower values, but with the same tendency. This discrepancy has also been reported in other works and is a topic of ongoing research.

Along with the electron density and the atom to molecule ratio, the proton fraction also increases from 34% to 42%. The  $H_2^+$  fraction is almost equal to the proton fraction and rises only marginally less from 35% to 40%. This high  $H_2^+$  fraction compared to ASDEX Upgrade is attributed to the lower gas pressure at GLADIS. The  $H_3^+$  fraction drops from 31% to 18%. When the ion species distribution is scaled with the electron density, absolute ion densities are obtained. It can be seen that in absolute units, the densities of  $H^+$  and  $H_2^+$  increase, while the  $H_3^+$  density stays constant due to the constant pressure.

The gas temperature is almost independent from the RF power like at ASDEX Upgrade. The value of around 1070 K at GLADIS is lower than at ASDEX Upgrade because the gas pressure is only half as high. The vibrational population of  $d^3\Pi_u$  also shows no significant variation with the RF power. It is similar to the one measured at ASDEX Upgrade and similarly difficult to interpret as a ground state vibrational temperature. The vibrational temperature is estimated to be 5000 K or more.

A higher gas pressure also causes an increase of the electron density. The measured values were between  $2.1 \cdot 10^{17} \text{ m}^{-3}$  and  $4.2 \cdot 10^{17} \text{ m}^{-3}$ . Because the increase of the neutral gas density is slightly stronger, the total degree of ionisation actually drops slightly. It stays in the range of  $1 \cdot 10^{-3}$ , however. The atom to molecule ratio also decreases with increasing pressure. The intensity ratio of the  $H_\gamma$  line and the Fulcher band yields values between 0.11 and 0.08. The absolute evaluation of the Balmer lines again yields systematically lower values (apart from one measurement) with the same tendency as the relative measurements. In absolute units however, the atom density actually stays constant. The decreasing density ratio is caused by a higher molecule density at higher pressures.

The measurement of the ion species distribution shows that  $H^+$  and  $H_3^+$  fractions increase and the  $H_2^+$  fraction decreases with the gas pressure. At 0.82 Pa, the  $H_2^+$  fraction is highest with 51%. The  $H^+$  and  $H_3^+$  fractions are 31% respectively 11%

at this pressure. For higher pressures the  $\text{H}^+$  and  $\text{H}_3^+$  fractions increase to up to 47% respectively 24%, and the  $\text{H}_2^+$  fraction drops to 29%.

Again, the absolute densities are more favourable for a physical interpretation. The  $\text{H}^+$  density increases while the  $\text{H}_2^+$  fraction stays approximately constant. In correlation with the densities of the neutral atoms and molecules, this means that the degree of ionisation increases for the atoms and decreases for the molecules. Considering the higher ionisation energy of the molecules, this can be linked to a decrease of the electron temperature. The other effect is that the production of  $\text{H}_3^+$  by the reaction of  $\text{H}_2$  and  $\text{H}_2^+$  becomes more effective at higher pressure. Therefore, the  $\text{H}_3^+$  density increases with the gas pressure. This effect also reduces the  $\text{H}_2^+$  density.

The pressure also influences the gas temperature and the vibrational population. The gas temperature increases with the pressure because of the reduced diffusion of gas particles to the water cooled walls at higher pressures. The values range from 900 K to 1170 K. For the vibrational population, a slightly stronger depopulation of the  $v' = 2$  and  $v' = 3$  states relative to the  $v' = 0$  state at higher pressures can be interpreted as an increase of the ground state vibrational temperature.

The extrapolation of the plasma parameters in the ion source measured at GLADIS agrees reasonably well with measurements in the driver of an RF-driven negative hydrogen ion source. This suggests that an extrapolation of the ion species distribution which cannot be measured at negative ion sources is also valid. The extrapolation points towards the  $\text{H}_2^+$  ions constituting the largest fraction, followed by  $\text{H}^+$ . The  $\text{H}_3^+$  fraction is expected to be small.

**To summarise, the spectroscopic survey of the investigated RF-driven ion source has yielded valuable information about the general relations of the RF input power and the gas pressure with the plasma parameters in the ion source and the ion species distribution in the beam. Both plasma sources show analogous behaviour concerning variations of RF input power and gas pressure. Therefore, they demonstrate that the general relations that are pointed out in this thesis are widely independent of the exact implementation of an RF-driven positive hydrogen ion source. The results can even be extrapolated to the driver of RF-driven negative hydrogen ion sources.**

The effects of the hydrogen isotope on the atom to molecule ratio and the ion species distribution can be attributed to the higher electron density in deuterium plasmas at otherwise equal conditions. The influence on the gas temperature can be explained by the higher mass ratio of the heavy particles to the heated electrons and by the higher atom to molecule ratio in deuterium. The influence of the isotope on the vibrational temperature is directly related to the different mass of  $\text{H}_2$  and  $\text{D}_2$  molecules.

All in all, the results of this work are a helpful step towards understanding the relations of the source plasma parameters and the extracted beam of positive ion based NBI systems.



# A Appendix

## A.1 Sample spectra

### Hydrogen

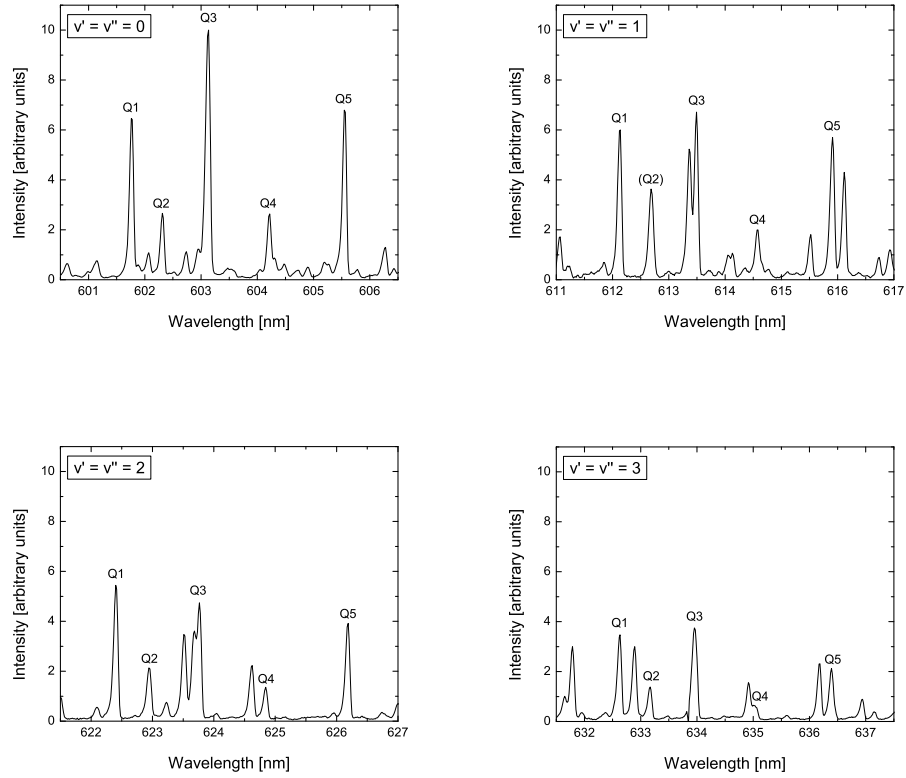


**Figure A.1:** Sample spectra of the first four diagonal vibrational transition of the hydrogen Fulcher band ( $d^3\Pi_u \rightarrow a^3\Sigma_g^+$ ). The spectra were recorded at GLADIS at  $P_{RF} = 26$  kW and  $p_{source} = 1.26$  Pa. Occasional superpositions of spectral lines cause uncertainties in the measurement.

## Deuterium

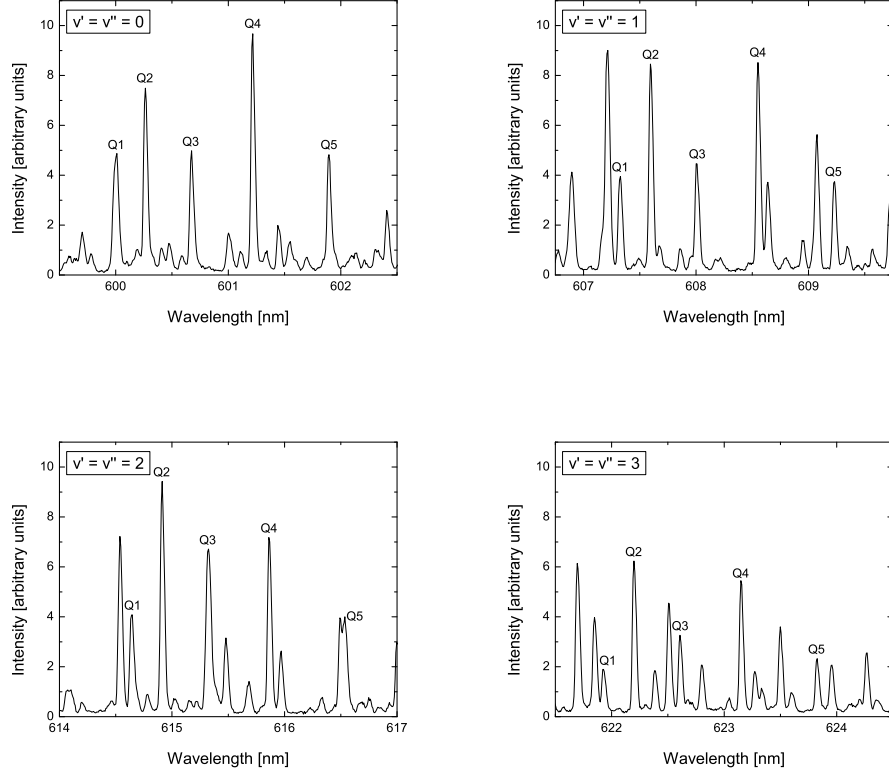


**Figure A.2:** Sample spectra of the first four diagonal vibrational transition of the deuterium Fulcher band ( $d^3\Pi_u \rightarrow a^3\Sigma_g^+$ ). The spectra were recorded at the ASDEX Upgrade NBI source at  $P_{RF} = 87$  kW and  $p_{source} \approx 2.5$  Pa. Note the closer spacing between the rotational lines and the reversed intensity change compared to hydrogen.

## A.2 Molecular Data

### Rotational states

Tabs. A.1 to A.4 list the molecular data for the rotational states of the  $d^3\Pi_u$  state in hydrogen, and Tabs. A.5 to A.8 show the same for deuterium.  $J$  is the rotational quantum number and  $\Delta E$  is the energy referenced to the  $J' = 1$  state. The  $\Delta E$  values are taken from [Die72] for hydrogen and from [LU08] for deuterium. Slanted figures indicate values derived from fits to the literature data. The Hönl-London factors  $S_{J'}$  for all three rotational branches (after [Her53]) and the  $\gamma_{J'}$  factors are also listed.

Only the rotational states  $J' = 1$  to  $J' = 13$  were used for modelling the Fulcher spectrum in order to calculate the  $f_v(T_{rot})$  factors, and only  $J' = 1$  to  $J' = 5$  for the Q branch were measured.

### Hydrogen

**Table A.1:** Rotational states of  $d^3\Pi_u$  in hydrogen, vibrational band  $v' = v'' = 0$ .

$d^3\Pi_u^-$ (Q branch)				$d^3\Pi_u^+$ (P and R branches)				
$J'$	$\Delta E$ [cm $^{-1}$ ]	$S_{J'}$ Q	$\gamma_{J'}$	$J'$	$\Delta E$ [cm $^{-1}$ ]	$S_{J'}$ P	$S_{J'}$ R	$\gamma_{J'}$
1	0	0.75	3	1	0	0.25	0.5	1
2	117.77	1.25	1	2	118.65	0.5	0.75	3
3	293.27	1.75	3	3	295.34	0.75	1	1
4	525.13	2.25	1	4	528.52	1	1.25	3
5	811.57	2.75	3	5	816.31	1.25	1.5	1
6	1150.72	3.25	1	6	1156.38	1.5	1.75	3
7	1538.75	3.75	3	7	1545.89	1.75	2	1
8	1982.04	4.25	1	8	1996.52	2	2.25	3
9	2482.59	4.75	3	9	2499.21	2.25	2.5	1
10	3035.15	5.25	1	10	3056.19	2.5	2.75	3
11	3641.46	5.75	3	11	3667.48	2.75	3	1
12	4301.52	6.25	1	12	4333.06	3	3.25	3
13	5015.33	6.75	3	13	5052.93	3.25	3.5	1

**Table A.2:** Rotational states of  $d^3\Pi_u$  in hydrogen, vibrational band  $v' = v'' = 1$ .

$d^3\Pi_u^-$ (Q branch)				$d^3\Pi_u^+$ (P and R branches)				
$J'$	$\Delta E$ [cm $^{-1}$ ]	$S_{J'}$ Q	$\gamma_{J'}$	$J'$	$\Delta E$ [cm $^{-1}$ ]	$S_{J'}$ P	$S_{J'}$ R	$\gamma_{J'}$
1	0	0.75	3	1	0	0.25	0.5	1
2	111.76	1.25	1	2	110.47	0.5	0.75	3
3	278.34	1.75	3	3	272.17	0.75	1	1
4	498.37	2.25	1	4	486.01	1	1.25	3
5	770.24	2.75	3	5	723.01	1.25	1.5	1
6	1092.01	3.25	1	6	1017.40	1.5	1.75	3
7	1461.10	3.75	3	7	1352.16	1.75	2	1
8	1875.15	4.25	1	8	1730.51	2	2.25	3
9	2349.82	4.75	3	9	2152.47	2.25	2.5	1
10	2871.36	5.25	1	10	2618.02	2.5	2.75	3
11	3443.44	5.75	3	11	3127.18	2.75	3	1
12	4066.05	6.25	1	12	3679.94	3	3.25	3
13	4739.19	6.75	3	13	4276.29	3.25	3.5	1

**Table A.3:** Rotational states of  $d^3\Pi_u$  in hydrogen, vibrational band  $v' = v'' = 2$ .

$d^3\Pi_u^-$ (Q branch)				$d^3\Pi_u^+$ (P and R branches)				
$J'$	$\Delta E$ [cm $^{-1}$ ]	$S_{J'}$ Q	$\gamma_{J'}$	$J'$	$\Delta E$ [cm $^{-1}$ ]	$S_{J'}$ P	$S_{J'}$ R	$\gamma_{J'}$
1	0	0.75	3	1	0	0.25	0.5	1
2	106.01	1.25	1	2	107.69	0.5	0.75	3
3	263.93	1.75	3	3	267.72	0.75	1	1
4	472.50	2.25	1	4	478.41	1	1.25	3
5	730.23	2.75	3	5	737.68	1.25	1.5	1
6	1035.07	3.25	1	6	1042.98	1.5	1.75	3
7	1392.51	3.75	3	7	1390.23	1.75	2	1
8	1798.90	4.25	1	8	1792.93	2	2.25	3
9	2255.05	4.75	3	9	2242.05	2.25	2.5	1
10	2760.96	5.25	1	10	2739.29	2.5	2.75	3
11	3316.64	5.75	3	11	3284.65	2.75	3	1
12	3922.09	6.25	1	12	3878.14	3	3.25	3
13	4577.29	6.75	3	13	4519.76	3.25	3.5	1



**Table A.4:** Rotational states of  $d^3\Pi_u$  in hydrogen, vibrational band  $v' = v'' = 3$ .

$d^3\Pi_u^-$ (Q branch)				$d^3\Pi_u^+$ (P and R branches)				
$J'$	$\Delta E$ [cm $^{-1}$ ]	$S_{J'}$ Q	$\gamma_{J'}$	$J'$	$\Delta E$ [cm $^{-1}$ ]	$S_{J'}$ P	$S_{J'}$ R	$\gamma_{J'}$
1	0	0.75	3	1	0	0.25	0.5	1
2	100.39	1.25	1	2	102.80	0.5	0.75	3
3	249.92	1.75	3	3	254.35	0.75	1	1
4	447.37	2.25	1	4	454.65	1	1.25	3
5	691.22	2.75	3	5	703.70	1.25	1.5	1
6	984.03	3.25	1	6	1001.50	1.5	1.75	3
7	1324.39	3.75	3	7	1348.05	1.75	2	1
8	1712.58	4.25	1	8	1743.35	2	2.25	3
9	2148.61	4.75	3	9	2187.40	2.25	2.5	1
10	2632.48	5.25	1	10	2680.20	2.5	2.75	3
11	3164.18	5.75	3	11	3221.75	2.75	3	1
12	3743.71	6.25	1	12	3812.05	3	3.25	3
13	4371.08	6.75	3	13	4451.1	3.25	3.5	1

**Deuterium****Table A.5:** Rotational states of  $d^3\Pi_u$  in deuterium, vibrational band  $v' = v'' = 0$ .

$d^3\Pi_u^-$ (Q branch)				$d^3\Pi_u^+$ (P and R branches)				
$J'$	$\Delta E$ [cm $^{-1}$ ]	$S_{J'}$ Q	$\gamma_{J'}$	$J'$	$\Delta E$ [cm $^{-1}$ ]	$S_{J'}$ P	$S_{J'}$ R	$\gamma_{J'}$
1	0	0.75	1	1	0	0.25	0.5	2
2	59.56	1.25	2	2	59.73	0.5	0.75	1
3	148.54	1.75	1	3	149.03	0.75	1	2
4	266.70	2.25	2	4	267.54	1	1.25	1
5	413.50	2.75	1	5	414.80	1.25	1.5	2
6	588.45	3.25	2	6	590.18	1.5	1.75	1
7	790.83	3.75	1	7	793.03	1.75	2	2
8	1019.95	4.25	2	8	1022.57	2	2.25	1
9	1275.00	4.75	1	9	1277.97	2.25	2.5	2
10	1554.99	5.25	2	10	1558.19	2.5	2.75	1
11	1860.08	5.75	1	11	1861.76	2.75	3	2
12	2186.24	6.25	2	12	2189.58	3	3.25	1
13	2535.38	6.75	1	13	2540.18	3.25	3.5	2

**Table A.6:** Rotational states of  $d^3\Pi_u$  in deuterium, vibrational band  $v' = v'' = 1$ .

$d^3\Pi_u^-$ (Q branch)				$d^3\Pi_u^+$ (P and R branches)				
$J'$	$\Delta E$ [cm $^{-1}$ ]	$S_{J'}$ Q	$\gamma_{J'}$	$J'$	$\Delta E$ [cm $^{-1}$ ]	$S_{J'}$ P	$S_{J'}$ R	$\gamma_{J'}$
1	0	0.75	1	1	0	0.25	0.5	2
2	57.38	1.25	2	2	57.48	0.5	0.75	1
3	143.17	1.75	1	3	143.34	0.75	1	2
4	257.05	2.25	2	4	256.79	1	1.25	1
5	398.55	2.75	1	5	395.42	1.25	1.5	2
6	567.17	3.25	2	6	575.67	1.5	1.75	1
7	762.20	3.75	1	7	768.3	1.75	2	2
8	982.99	4.25	2	8	988.91	2	2.25	1
9	1228.73	4.75	1	9	1234.86	2.25	2.5	2
10	1498.56	5.25	2	10	1515.37	2.5	2.75	1
11	1791.50	5.75	1	11	1819.78	2.75	3	2
12	2108.15	6.25	2	12	2151.36	3	3.25	1
13	2446.84	6.75	1	13	2510.09	3.25	3.5	2

**Table A.7:** Rotational states of  $d^3\Pi_u$  in deuterium, vibrational band  $v' = v'' = 2$ .

$d^3\Pi_u^-$ (Q branch)				$d^3\Pi_u^+$ (P and R branches)				
$J'$	$\Delta E$ [cm $^{-1}$ ]	$S_{J'}$ Q	$\gamma_{J'}$	$J'$	$\Delta E$ [cm $^{-1}$ ]	$S_{J'}$ P	$S_{J'}$ R	$\gamma_{J'}$
1	0	0.75	1	1	0	0.25	0.5	2
2	55.30	1.25	2	2	55.70	0.5	0.75	1
3	137.96	1.75	1	3	138.96	0.75	1	2
4	247.67	2.25	2	4	249.37	1	1.25	1
5	383.98	2.75	1	5	386.49	1.25	1.5	2
6	546.41	3.25	2	6	549.71	1.5	1.75	1
7	734.29	3.75	1	7	738.38	1.75	2	2
8	946.96	4.25	2	8	951.75	2	2.25	1
9	1183.60	4.75	1	9	1189.03	2.25	2.5	2
10	1443.47	5.25	2	10	1449.20	2.5	2.75	1
11	1728.00	5.75	1	11	1731.18	2.75	3	2
12	2025.24	6.25	2	12	2034.11	3	3.25	1
13	2362.59	6.75	1	13	2375.99	3.25	3.5	2

**Table A.8:** Rotational states of  $d^3\Pi_u$  in deuterium, vibrational band  $v' = v'' = 3$ .

$d^3\Pi_u^-$ (Q branch)				$d^3\Pi_u^+$ (P and R branches)				
$J'$	$\Delta E$ [cm $^{-1}$ ]	$S_{J'}$	Q	$\gamma_{J'}$	$J'$	$\Delta E$ [cm $^{-1}$ ]	$S_{J'}$	P R $\gamma_{J'}$
1	0	0.75	1	1	1	0	0.25	0.5 2
2	53.26	1.25	2	2	2	53.50	0.5	0.75 1
3	132.83	1.75	1	1	3	133.41	0.75	1 2
4	238.49	2.25	2	2	4	239.29	1	1.25 1
5	369.78	2.75	1	1	5	370.42	1.25	1.5 2
6	526.16	3.25	2	2	6	525.14	1.5	1.75 1
7	707.02	3.75	1	1	7	702.85	1.75	2 2
8	911.73	4.25	2	2	8	908.44	2	2.25 1
9	1139.54	4.75	1	1	9	1137.92	2.25	2.5 2
10	1389.61	5.25	2	2	10	1392.31	2.5	2.75 1
11	1661.03	5.75	1	1	11	1671.58	2.75	3 2
12	1949.95	6.25	2	2	12	1975.76	3	3.25 1
13	2259.78	6.75	1	1	13	2304.82	3.25	3.5 2

## Scaling of rotational temperatures

**Table A.9:** Ratio of rotational constants  $B_{v''=0}(X^1\Sigma_g^+) / B_{v'}(d^3\Pi_u)$  in the ground state and the  $d^3\Pi_u$  state for hydrogen and deuterium.

$v'$	$\text{H}_2$	$\text{D}_2$
0	2.00	2.00
1	2.11	2.08
2	2.24	2.16
3	2.38	2.25

## Vibrational states

All energy eigenvalues, Franck-Condon factors and transition probabilities for vibrational states respectively transitions that were used were taken from [FW06].

## $f_v(T_{rot})$ scaling factors

### Hydrogen

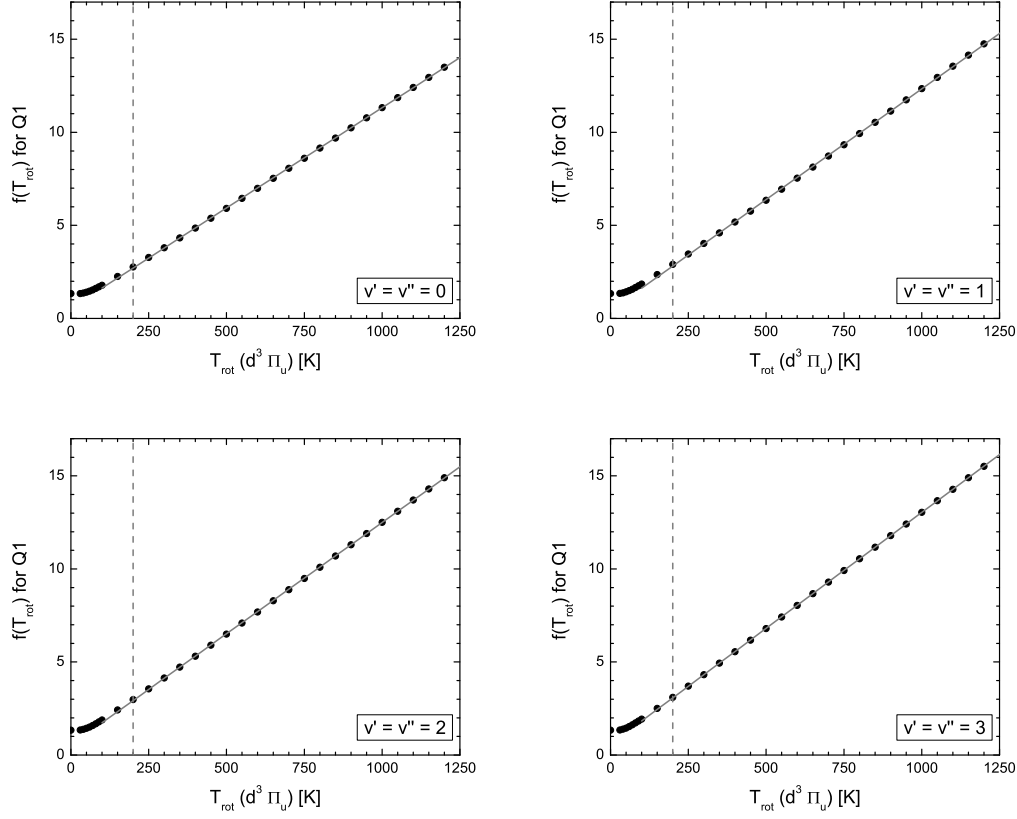


**Figure A.3:**  $f_v(T_{rot})$  scaling factors normalized to the Q1 line of the hydrogen Fulcher band for the first four diagonal vibrational transitions  $v = v' = v'' = 0, 1, 2, 3$  in hydrogen. The calculated data can be approximated very well with a linear fit between 200 K and 1200 K. The low temperature limit represents the ratio of the Hönl-London factors of the R, Q and P branches and the statistical abundances of ortho and para hydrogen in the  $J' = 1$  state.

## Deuterium

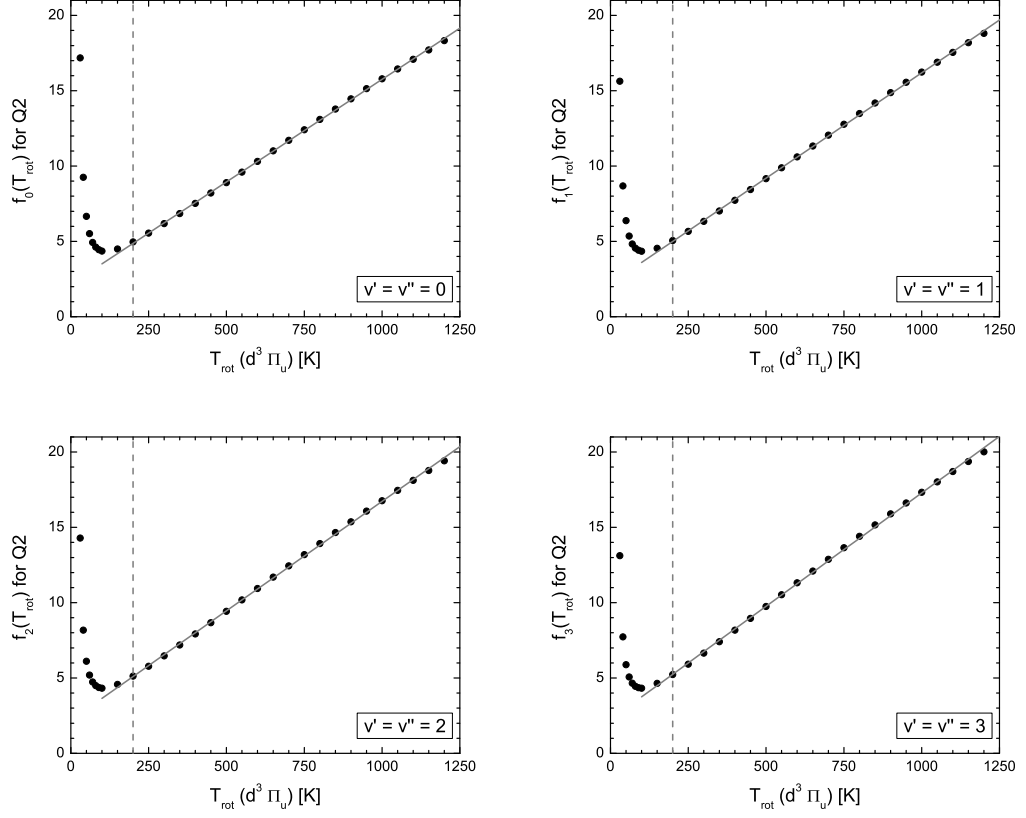


**Figure A.4:**  $f_v(T_{rot})$  scaling factors normalized to the Q2 line of the deuterium Fulcher band for the first four diagonal vibrational transitions  $v = v' = v'' = 0, 1, 2, 3$  in deuterium. The calculated data can be approximated very well with a linear fit between 200 K and 1200 K. The divergence for  $T_{rot} \rightarrow 0$  originates from the fact that the  $J' = 2$  state is not populated at very low temperatures.

## A.3 JET Neutral Beam Test Bed

### A.3.1 Wavelength Calibration Results

**Table A.10:** Wavelength Calibration Results, Validity range: 350 nm - 810 nm.  $x$  is the displayed wavelength of the spectrometer,  $y$  the calibrated value.

Value $y$	Fit model	Fit parameters
Pixel 0 wavelength	$y = a \cdot x + b$	$a = 1.00065$ $b = -50.1571$
Wavelength increment per pixel	$y = a \cdot x^2 + b \cdot x + c$	$a = -1.75780 \cdot 10^9$ $b = 1.08837 \cdot 10^5$ $c = 0.226481$

### A.3.2 Absolute Intensity Calibration

**Table A.11:** Fibre Mapping for the JET NBTB spectrometer.

Fibre	Hot Cell	Position on Beam	SPEX Ch.	Comments
2	2 midsection	top vertical	1	fixed
3	3 midsection		2	fixed
4	4 midsection		3	fixed
5	5 midsection		4	fixed
6	6 midsection		5	fixed
7	7 midsection		6	fixed
8	8 midsection		7	swap with 19
9	9 midsection		8	swap with 20
10	10 midsection		9	swap with 21
11	11 midsection		10	swap with 22
12	12 midsection	↓	11	swap with 23
13	13 midsection	bottom vertical	12	swap with 24
19	2 top	right horizontal	7	swap with 8
20	3 top		8	swap with 9
21	4 top		9	swap with 10
22	5 top		10	swap with 11
23	6 top	↓	11	swap with 12
24	7 top	left horizontal	12	swap with 13

### A.3.3 Fibre Holder Construction Drawings

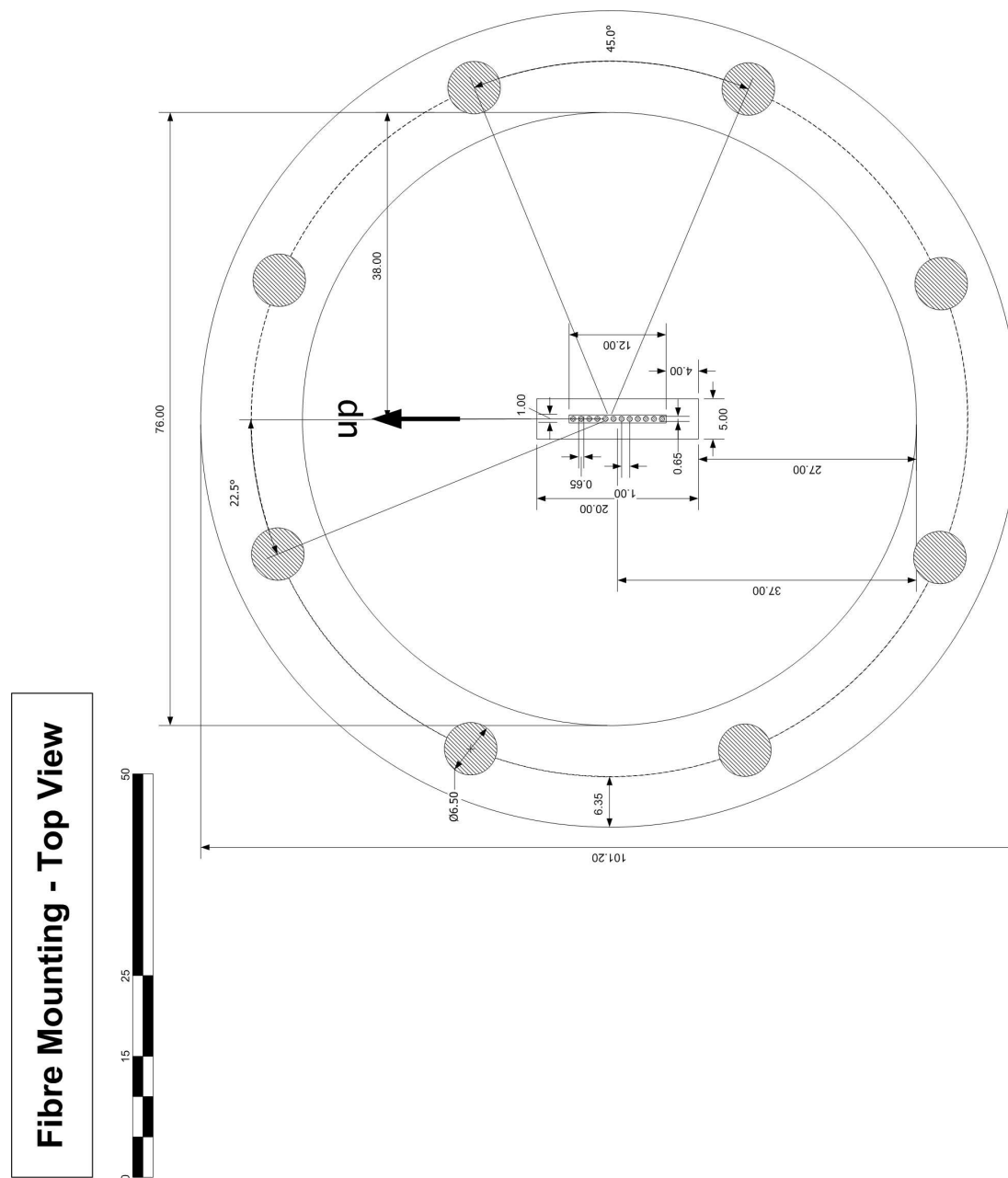


**Figure A.5:** Construction drawing of the fibre holder for the JET NBTB spectrometer, top view.



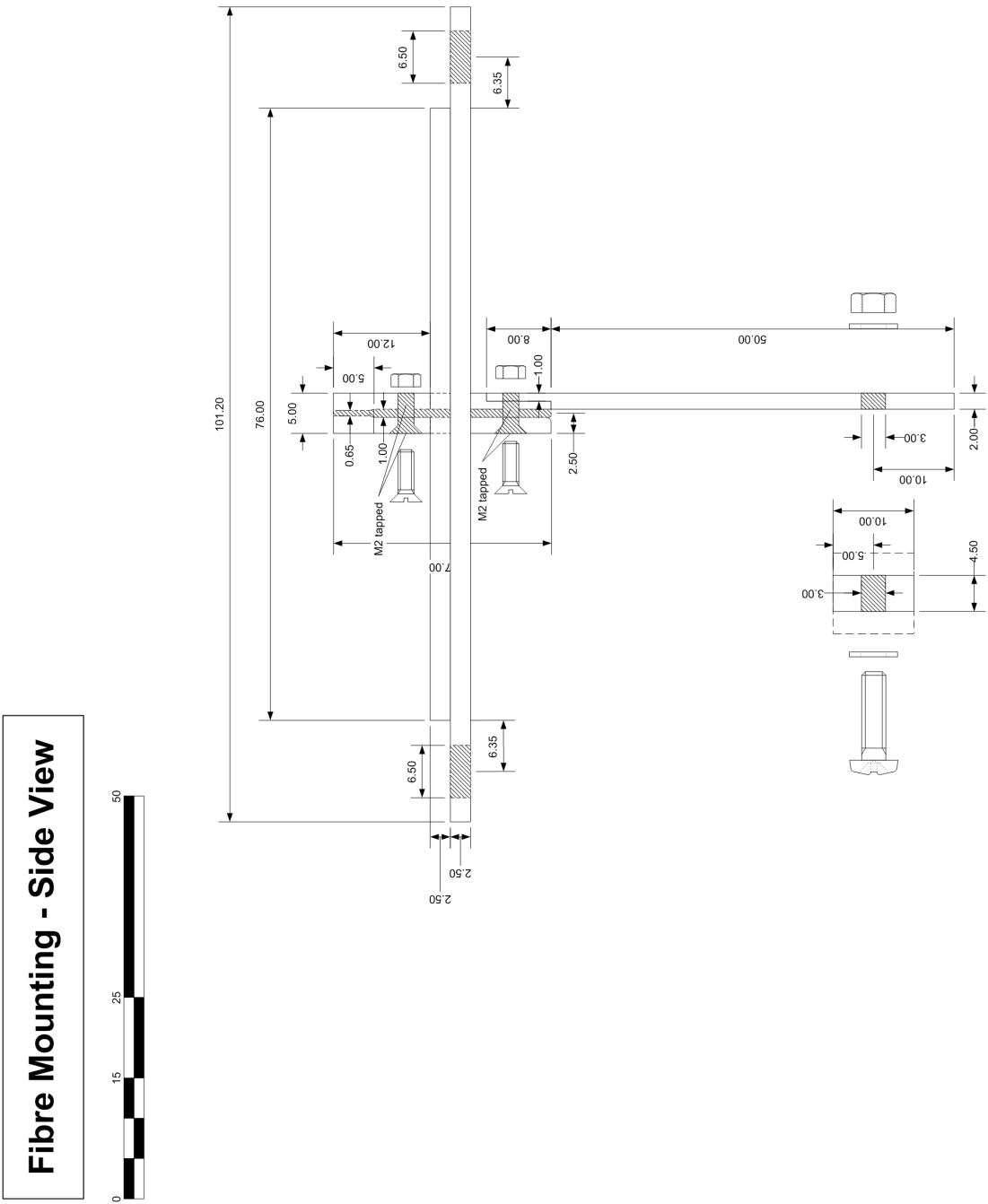


**Figure A.6:** Construction drawing of the fibre holder for the JET NBTB spectrometer, side view.

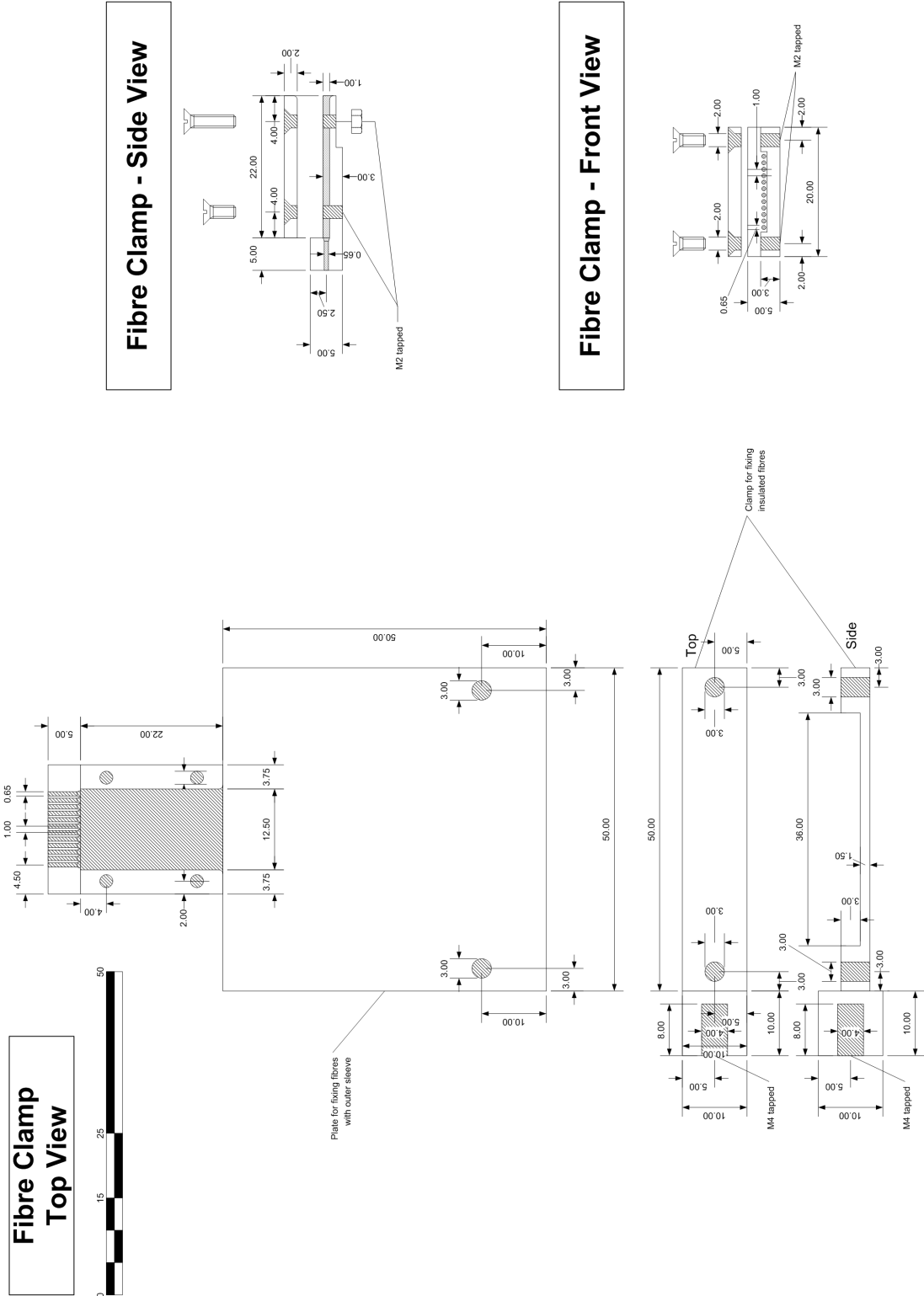


Figure A.7: Construction drawing of the fibre holder for the JET NBTB spectrometer, fibre clamp detail.

# Bibliography

- [Beh00] K. Behringer, *Einführung in die Plasmaspektroskopie*, Lecture script, Universität Augsburg, 2000.
- [Beh01] ———, *Spektroskopische Diagnostik von Nichtgleichgewichtsplasmen*, Lecture script, Universität Augsburg, 2001.
- [BF00] K. Behringer and U. Fantz, *The influence of opacity on hydrogen excited-state population and applications to low-temperature plasmas*, New Journal of Physics **2** (2000), 23.1.
- [C<sup>+</sup>06] D. Ciric et al., *Overview of the JET neutral beam enhancement project*, Proc. SOFT Conference (Warsaw, Poland), Sep 11–15 2006.
- [CBC83] C. F. Chan, C. F. Burrell, and W. S. Cooper, *Model of positive ion sources for neutral beam injection*, Journal of Applied Physics **54**(11) (1983), 6619.
- [CFG98] D. Ciric, H.-D. Falter, and D.J. Godden, *Space and time resolved doppler spectroscopy of neutral beams*, Proc. 20th Symposium on Fusion Technology (Marseille, France), vol. 1, 1998, p. 496.
- [Cox03] S. Cox, *A super high current tetrode for JET*, CCNB Meeting (Padua, Italy), Jun 5–6 2003.
- [DAF<sup>+</sup>87] G. Düsing, H. Altmann, H. Falter, A. Goede, R. Haange, R.S. Hemsworth, P. Kupschus, D. Stork, and E. Thompson, *Neutral beam injection system*, Fusion Technology **11** (1987), 163.
- [Die72] G. H. Dieke, *The Hydrogen Molecule Wavelength Tables*, Wiley Interscience, 1972.
- [Dra96] G. W. F. Drake, *Atomic, Molecular & Optical Physics Handbook*, American Institute of Physics, 1996.
- [EJ07] EFDA-JET, *EFDA-JET web pages*, <http://www.jet.efda.org/>, 2007.

- [EL73] K. W. Ehlers and K. N. Leung, *Characteristics of the Berkeley multicusp ion source*, Review of Scientific Instruments **50** (1973), 1353.
- [Fan01] U. Fantz, *Atomic and molecular emission spectroscopy in low temperature plasmas containing hydrogen and deuterium*, Habilitationsschrift, Universität Augsburg, 2001.
- [FFF<sup>+</sup>06] U. Fantz, H. Falter, P. Franzen, D. Wunderlich, et al., *Spectroscopy—A powerful tool in source development*, Nuclear Fusion **46** (2006), S297.
- [FH98] U. Fantz and B. Heger, *Spectroscopic diagnostics of the vibrational population in the ground state of  $H_2$  and  $D_2$  molecules*, Plasma Physics and Controlled Fusion **40** (1998), 2023.
- [FKS82] J.-H. Feist, J. Kolos, and E. Speth, *Design of a water cooled extraction system for a 55 kV, 22 A, 10 sec hydrogen ion source*, Proc. 12th Symposium on Fusion Technology (Jülich, Germany), vol. 2, 1982, p. 1301.
- [FKS<sup>+</sup>95] J.-H. Feist, W. Kraus, E. Speth, M. Ciric, B. Heinemann, F. Probst, and R. Riedl, *Progress in the development of a large area RF plasma generator*, Proc. 16th IEEE/NPSS Symposium on Fusion Engineering (Champaign, IL, USA), vol. 2, Sep 30–Oct 05 1995, p. 976.
- [FKV<sup>+</sup>99] P. Franzen, W. Kraus, O. Vollmer, B. Heinemann, R. Riedl, E. Speth, and A. Stäbler, *Determination of the species distribution and the divergence of the ASDEX Upgrade neutral beam system*, Proc. 26th EPS conference on Controlled Fusion and Plasma Physics (Maastricht, Netherlands), Jun 14–18 1999, p. 485.
- [FOS<sup>+</sup>98] P. Franzen, S. Obermayer, J. Schäffler, A. Stäbler, E. Speth, and O. Vollmer, *Beam current feedback regulation of the RF neutral beam sources of ASDEX Upgrade*, Fusion Engineering and Design **56–57** (1998), 487.
- [FVS98] P. Franzen, O. Vollmer, and A. Stäbler, *Spectroscopic determination of the species distributions of the ASDEX Upgrade neutral beam injection systems*, Report 4/278, Max-Planck-Institut für Plasmaphysik, Garching, Germany, 1998.
- [FW06] U. Fantz and D. Wunderlich, *Franck-Condon factors, transition probabilities, and radiative lifetimes for hydrogen molecules and their isotopomers*, Atomic Data and Nuclear Data Tables **92** (2006), 853.

- [GBB<sup>+</sup>05] H. Greuner, H. Bolt, B. Böswirth, T. Franke, P. McNeely, S. Obermayer, N. Rust, and R. Süß, *Design, performance and construction of a 2 MW ion beam test facility for plasma facing components*, Fusion Engineering and Design **75-79** (2005), 345.
- [GBBM07] H. Greuner, B. Böswirth, B. Boscari, and P. McNeely, *High heat flux facility GLADIS: Operational characteristics and results of W7-X pre-series target tests*, Journal of Nuclear Materials **367-370** (2007), 1444.
- [GCF00] D.J. Godden, D. Ciric, and H.-D. Falter, *Modelling ion source uniformity*, Proc. 22th Symposium on Fusion Technology (Madrid, Spain), 2000.
- [Heg02] B. Heger, *Untersuchung und Interpretation der Molekülstrahlung von Wasserstoff und Deuterium in Niederdruckplasmen*, Ph.D. thesis, Universität Augsburg, 2002.
- [Hel89] K.H. Hellwege, *Einführung in die Physik der Molekeln*, 2<sup>nd</sup> ed., Springer-Verlag, 1989.
- [Hem85] R. S. Hemsworth, *Species determination using Doppler shift spectroscopy for non-equilibrium hydrogen ions and/or neutral beams*, Report JET-DN-C(85)8, JET Joint Undertaking, Abingdon, Oxfordshire, UK, 1985.
- [Her53] G. Herzberg, *Molecular Spectra and Molecular Structure*, 2<sup>nd</sup> ed., vol. I, D. Van Nostrand Company, 1953, Spectra of Diatomic Molecules.
- [HH79] G. Herzberg and K. P. Huber, *Molecular Spectra and Molecular Structure*, 15<sup>th</sup> ed., vol. IV, D. Van Nostrand Company, 1979, Constants of Diatomic Molecules.
- [IPP08] IPP - Max-Planck-Institute for Plasma Physics, *IPP web pages*, <http://www.ipp.mpg.de/>, 2008.
- [KFH<sup>+</sup>01] W. Kraus, P. Franzen, B. Heinemann, E. Speth, and O. Vollmer, *Recent developments of long pulse RF ion sources for NBI systems*, Fusion Engineering and Design **56-57** (2001), 499.
- [KSF<sup>+</sup>98] W. Kraus, E. Speth, J.-H. Feist, B. Heinemann, R. Riedl, R. Trainham, and C. Jacquot, *Large-area radio frequency plasma sources for fusion applications*, Review of Scientific Instruments **69(2)** (1998), 956.

- [Lor05] A. Lorenz, *Ortsaufgelöste  $H_\alpha$ -Dopplerspektroskopie an einem Wasserstoffstrahl aus einer negativen Ionenquelle*, Diploma thesis, Technische Universität München, 2005.
- [LU08] B. P. Lavrov and I. S. Umrikhin, *Rovibronic energy levels for triplet electronic states of molecular deuterium*, <http://arxiv.org> (2008), arXiv:physics/0703114v3.
- [Mai07] F. Maisberger, *Private communication*, 2007.
- [Reg05] M. Regler, *Messung ausgewählter übergänge im Wasserstoffmolekül und Vergleich mit Rechnungen*, Diploma thesis, Universität Augsburg, 2005.
- [SC03] E. Surrey and B. Crowley, *Spectroscopic measurement of gas temperature in the neutraliser of the JET neutral beam injection system*, Report EFDA-JET-PR(03)18, EFDA-JET Culham Science Center, Abingdon, Oxfordshire, UK, 2003.
- [SCC<sup>+</sup>02] E. Surrey, B. Crowley, S. J. Cox, D. Ciric, and A. R. Ellingboe, *Experimental studies of the JET NBI neutraliser plasma*, Proc. SOFT Conference (Helsinki, Finland), Sep 9–13 2002, p. 591.
- [SCCG02] E. Surrey, D. Ciric, B. Crowley, and D. J. Godden, *Properties of the JET 130kV/60A Positive Ion Neutral Injector*, Proc. 19th IEEE/NPSS Symposium on Fusion Engineering (Atlantic City, New Jersey, USA), Jan 22–25 2002, p. 64.
- [SCF<sup>+</sup>99] E. Speth, M. Ciric, J.H. Feist, P. Frank, B. Heinemann, W. Kraus, F. Probst, R. Riedl, R. Trainham, O. Vollmer, and R. Wilhelm, *Rf ion sources for fusion applications: design, development and performance*, Fusion Engineering and Design **46** (1999), 383.
- [SFF<sup>+</sup>06] E. Speth, H.D. Falter, P. Franzen, U. Fantz, et al., *Overview of the RF source development programme at IPP Garching*, Nuclear Fusion **46** (2006), S220.
- [Spe89] E. Speth, *Neutral beam heating of fusion plasmas*, Rep. Prog. Phys. **52** (1989), 57.
- [Wün04] D. Wunderlich, *Berechnung von Teilchendichten für die Diagnostik an Niedertemperaturplasmen*, Ph.D. thesis, Universität Augsburg, 2004.

Finally I would like to thank all the people who helped me along the way of writing this thesis or who made it possible in the first place.

**PD Dr.-Ing Ursel Fantz**

for her invaluable help and tutoring during this thesis, and for giving me the opportunity to do the thesis in the first place.

**apl. Prof. Dr. Jörg K. N. Lindner**

for agreeing to do the second revision of this thesis.

**Dr. Patrick Starke**

for his great logistic help especially during my stay at JET, and for numerous patient proofreadings.

**Dr. Steve Gee, Dr. Brendan Crowley and the JET Beam Development Group**

for the invitation to JET and the great experience gained there.

**Dr. Albrecht Stäbler and the ASDEX Upgrade NBI team**

for giving me the opportunity to measure at their ion sources on very short notice and accommodating it in their tight operations schedule.

**Dr. Henri Greuner and the GLADIS team**

for providing me with ample measurement time at their experiment and for their extensive and welcoming assistance, also on short notice.

**Dr. Peter Franzen**

for assisting me with his extensive experience in  $H_\alpha$  Doppler spectroscopy.

**Dipl.-Phys. Stephan Dietrich**

for helping me out with numerous theoretical and practical details and for helping me with the testing and servicing of the ANDOR spectrometer.

**Mr Simon König and Ms Nikola Pascher**

for helping me with the commissioning, testing and servicing of the ANDOR spectrometer.

**Mr David Filimonov, Mr. Stefan Briefi and Mr. Philipp Schmidt**

for the friendly working atmosphere and for many interesting discussions.

Special thanks go to **my family** for their continuous support during the writing of this thesis and especially during my stay in the UK.

My very special thanks are dedicated to my girlfriend **Ms Elizaveta Zharova**, whose unwavering support gave me the strength to continue despite all difficulties.